Numerical study of the transition to turbulence in particulate pipe flows

Rouquier, Anthony

Award date:
2019

Awarding institution:
Coventry University

Numerical study of the transition to turbulence in particulate pipe flows

By
Anthony Rouquier

A thesis submitted in partial fulfilment of the University's requirements for the Degree of Master of Philosophy/Master of Research

February 2019

Certificate of Ethical Approval

Applicant:

Anthony Rouquier

Project Title:

Numerical study of the transition to turbulence in pipe flows with liquid and solid phases.

This is to certify that the above named applicant has completed the Coventry University Ethical Approval process and their project has been confirmed and approved as Low Risk

Date of approval:

06 December 2018

Project Reference Number:

P80329

Abstract

This dissertation aims to contribute to the knowledge of the effect of the addition of particles in the transition to turbulence of pipe flows. The following work studied, to this end, the linear stability of a particulate pipe flow where the solid phase is modelled with an Eulerian formulation and the system resolved using of an eigenvalue solver. This work has been extended to a linear transient growth analysis, with the same physical model and solid phase formulation. The transient growth analysis has been conducted with a linear Direct Numerical Simulation code. An iterative variational method has been used to obtain the flow transient growth. The last part of this work considers a point particle model using a mixed Eulerian-Lagrangian formulation, where the fluid phase is described with a standard Eulerian formulation while the solid phase behaviour is determined through particle Lagrangian tracking. This allows for a nonlinear analysis of the particulate flow, done with a DNS code. The linear stability analysis showed that the addition of particles can lead to linear instability at experimentally realistic parameters, as opposed to the single phase pipe flow which is linearly stable for all Reynolds numbers. This thesis also highlights the important role of the particles size on the flow stability. Smaller particles have a destabilising effect on the flow stability while the effect is inverted as particles become larger. Another critical parameter is the distribution of particles across the pipe, in particular across the particle radius. The effect of the particles on the flow stability is stronger when they are concentrated closer to the Segré-Silberberg radius. In particular, linear instability has only been observed when particles are concentrated in an annulus whose position is close to the Segré-Silberberg radius. The flow transient growth is also significantly increased by the addition of particles, in particular for, again, particles concentrated close to the Segré-Silberberg radius, for which the transient growth can be more than tripled compared to the case of the single phase flow. Moreover, we found with the point particle model a tendency for medium-sized particles to migrate and accumulate close to the wall, where their effect on the flow stability is larger.

Acknowledgements

I am grateful for Dr Chris Pringle and Professor Alban Pothérat for their guidance and support through the thesis, without which this project would have been an even more daunting task.

I had the fortune to work in a great environment, with helpful and friendly colleagues. Their presence helped me in many ways, they made those years more pleasant than they had any right to be and helped me through the harder parts.

My friends and family were also instrumental to this work by their unyielding support, for that I cannot thank them enough.

This project has been financed by NEL.

Contents

General introduction

Most flows can be classified in two categories – laminar and turbulent – with completely different properties and very distinct characteristics. Laminar flows are viscosity-dominated, have no lateral mixing, small gradients and are characterised by weak dissipation and slow diffusion. Examples of laminar flows are a flow of honey, a highly viscous fluid, a slow stream out of a nozzle. Laminar flows have simple structures and show little complexity, such that they behave in a deterministic way and are predictable. On the other hand, turbulent flows are characterised by a more complex, chaotic and unpredictable behaviour with multiscale vortices interacting with each other. Turbulent flows are dominated by advection and Reynolds stress. Turbulent flows are common, and typical examples of turbulent structures are torrents, the flow behind an obstacle (airplane wing, bridge pillar) or jets. Turbulent structures produce strong pressure and velocity gradients. Mixing occurs very rapidly in turbulent flows, this can be easily observed by dropping an ink droplet in a turbulent flow, and the dissipation rate of energy is much larger than in the laminar case.

Because laminar and turbulent flows have very different properties, it is often of critical importance to know the conditions leading to the transition from one to the other, in environmental flows as well as in more exotic cases, such as the flow inside the earth liquid core or stars. It is also of importance in the industrial sector with widespread potential applications: cars and planes aerodynamics performances have been, for example, improved by using more streamlined, aerodynamically efficient shapes which delay the onset of turbulence. The efficiency of fuel combustion is strongly dependent on the flow state, and the drag and friction in water and oil pipes is increased when the flow is turbulent. Transition to turbulence has therefore been a major topic of study for over a century. It is a complex, nonlinear chaotic problem still far from being understood today.

Transition to turbulence is generally studied through stability analysis. A stability analysis is the study of the effect of a perturbation on a steady laminar flow, namely whether this perturbation leads to a transition of the flow to a turbulent state or dies out eventually. The majority of the research done on stability focuses on single phase flows. However, real flows often are multiphase, further adding complexity to the topic of the transition to turbulence. This work focuses on a subset of multiphase flows: particulate flows, also called particle-laden flows. Particulate flows have a carrier phase, either liquid or gas, which is seeded by solid particles. Particulate flow relate to a wide range of applications, notably in the oil industry with the prevalence of oil and gas flows. Oil and gas flows contains solid impurities, such as sand, such that they combine fluid, gas and solid phases. Oil and gas flows are extremely difficult, with the current methods, to model. Modelling them as particulate flows allows to capture most of the dynamics while simplifying the problem. They are also frequently encountered in biofluid dynamics: blood is considered as a particulate flow, with red and white blood cells acting as particles of up to 40% of volume fraction, particulate flows have also been used to study the behaviour of self-propelled cells in the organism. In the case of environmental flows, examples of particulate

flows are found in rivers with transport of sediments as well as debris flows. Atmospheric pollution is due to the ejection of particles while the dynamics of droplets are key to rain and snow formation.

Pipe flows are a classical problem and a major area of research in fluid dynamics due to its significance as a subset of more general wall-bounded problems. The relative simplicity of the geometry, suitable to experimentation as well as its relevance to industry and engineering makes it one of the widely studied geometry. The interest in pipe flows also extends to particulate flows in the case of pipelines for oil and gas flows, and pipes are in general widely used in the industry. Another example is the blood flows in arteries. We have chosen, for these reasons, to focus in this work on pipe flow geometry.

One of the challenges regarding particulate flow is the need to accurately measure flow rates or volume fractions in complex fluid mixtures flowing through pipes; this issue concerns a wide range of industrial fields. Examples range from the precise determination of the volume fraction of oil in the oil-water-sand-gas mixture that is extracted from offshore wells, to needs in the food processing industry due to the large range of liquids conditions encountered, and flows of molten metal carrying impurities during recycling processes. In all these examples, the nature of the flow state needs to be determined to make accurate measurements; in particular, one needs to know whether the flow is turbulent. Having an estimate of the flow state as a function of its characteristics can prove indispensable when determining the pipe size or motor power that best suits requirements. Particulate pipe flows, including their transition to turbulence, are therefore attracting a growing interest from the scientific community. The addition of particles to the flow can have different effects on the flow stability depending on the particles parameters, such as size, shape, their volume concentration, whether they are neutrally buoyant or not, and whether they are monodisperse or polydisperse. In addition, parameters such as the pipe dimensions and roughness, the flow velocity and the fluid properties (viscosity and density) affects the flow stability.

The stability of particulate pipe flows is a problem that traverses several scientific fields. The complexity of this problem, coupled with the large range of parameters for both fluid and particles, contributes to making the issue of transition to turbulence in particulate flows outstandingly difficult to characterise entirely. It is therefore unsurprising that the knowledge accumulated so far is fragmented, with most of the work available in literature focusing on very specific aspects of the problem, that are difficult to generalise. The aim of this thesis is to further the understanding of how the stability of pipe flows is affected by the additions of particles by providing a more general groundwork using simplified models for the description of the solid phase.

The following work is solely numerical, it is however complemented by an experimental project on particulate pipe flows conducted in the the Fluid and Complex Systems Research Center at Coventry University. This work partly focuses on linearised particulate flows. The linear stability of single phase flows has been extensively studied, which allows for extensive comparison when considering

particulate flows. It is also a good starting point for categorising how the transition between laminar and turbulent states is affected by particles. This manuscript presents a nonlinear model built with the aim to obtain results even in the cases affected by the limitations of linear analysis. Another critical choice is the model used to describe the particles, two models have been used: a fully Eulerian method with an Eulerian formulation for the particles, and a point particle model with Lagrangian tracking. Using two models with distinct capabilities and limitations increases the range of results obtainable.

This dissertation is composed of four chapters, starting with an overview of the concepts involved in this work in Chapter 1: theoretical knowledge of the fluid and solid phases description, the modelling of particulate flows, the basic tenets of flows stability and transition to turbulence as well as the numerical methods allowing the study of stability. Chapter 2 describes the linear stability of a particulate pipe flow using an Eulerian formulation for the particles, with a focus on the impact of the particles relaxation time, volume concentration and radial distribution. Chapter 3 expands the previous chapter work with a transient growth analysis with the same model. In the last chapter is developed a more elaborate model for the solid phase using a point particle approximation with the objective of studying individual particle behaviour.

Chapter 1

Literature overview

This project lies at the intersection between transition to turbulence and particulate flow and the study is conducted through numerical means. We will give in this chapter an overview of the concepts involved in this work. First, with a short reminder on single phase flow and the assumptions made on the fluid, then is presented a summary of the theoretical knowledge concerning the ways particles are affected by the surrounding fluid. followed by a look at the existing models for the description of particulate flows. In a second time is given an overview of the knowledge concerning the transition between laminar and turbulent phases for single phase flows; following with the existing results for the transition of particulate flows. Finally, the chapter is concluded with the experimental and numerical tools available to study these topics.

1.1 Single phase flows dynamics

Theoretical models describing particulate flows are generally built upon single phase flows models, this is true for our work as well. Applying Newton's second law on a closed domain, one can derive the equation of the conservation of momentum describing the motion of viscous flows, the Navier-Stokes equations. The conservation of mass yields:

$$\frac{\partial \rho}{\partial t} = \nabla \cdot (\rho \mathbf{u}) \,, \tag{1.1}$$

as for the conservation of momentum,

$$\frac{\partial (\rho \mathbf{u})}{\partial t} + \nabla \cdot (\rho \mathbf{u} \times \mathbf{u}) = -\nabla p + \nabla \cdot \tau + \mathbf{F} \,, \tag{1.2}$$

where $\mathbf{u}$ is the fluid velocity, ρ its density and p the flow pressure. τ is the Cauchy stress tensor and $\mathbf{F}$ the volumetric forces applying on the flow, for example gravity or the effect of particles. This work focuses in the case of an incompressible Newtonian flow. For Newtonian flows the Cauchy stress tensor is equal to $(\mu \nabla \mathbf{u})$ with μ the dynamic viscosity. Incompressible flows have a constant density, mathematically this translates to $\partial_t \rho = \nabla \rho = 0$.

Equations (1.1) and (1.2) are, in the specific case of an incompressible, Newtonian flow, rewritten as:

$$\nabla \cdot \mathbf{u} = 0 \,, \tag{1.3}$$

$$\rho \left(\frac{\partial \mathbf{u}}{\partial t} + (\mathbf{u} \cdot \nabla) \mathbf{u} \right) = -\nabla p + \mu \nabla^2 \mathbf{u} + \mathbf{F} \,. \tag{1.4}$$

1.2 Fluid-particle dynamics

1.2.1 Fluid-particle coupling for a single particle

The fluid affects the particle through several physical mechanisms each applying a force on the particle, the motion of a particle in the flow can be written as a the sum of these forces $\mathbf{F_i}$,

$$m_p \frac{d\mathbf{u_p}}{dt} = \sum \mathbf{F_i} \,, \tag{1.5}$$

where $\mathbf{u_p}$ is the velocity of the particle. $d/dt = \partial_t + \mathbf{u_p} \cdot \nabla$ is the time derivative in the particle reference frame. The main forces acting on a spherical particle are as follows:

• *Effect of the undisturbed flow:* The particle is affected by the undisturbed flow pressure field and shear stress, the pressure force acting on a particle is, assuming a constant pressure gradient over the particle,

$$\mathbf{F_p} = -V_p \nabla p \,, \tag{1.6}$$

with V_p the particle volume and ρ the fluid density. The force on the particle due to the shear stress $\mathbf{F_{sh}}$ is

$$\mathbf{F_{sh}} = -V_p \rho \nabla \cdot \tau = V_p \mu \nabla^2 \mathbf{u} \,, \tag{1.7}$$

with $\mathbf{u}$ the surrounding fluid velocity. The sum of the forces $\mathbf{F_p}$ and $\mathbf{F_{sh}}$ is equal to

$$\mathbf{F_p} + \mathbf{F_{sh}} = m_p \frac{D\mathbf{u}}{Dt} \,, \tag{1.8}$$

with $D/Dt = \partial_t + \mathbf{u} \cdot \nabla$, the time derivative with regards to the fluid.

• *Virtual mass force:* the surrounding fluid is displaced by the particles, causing a drag proportional to the volume,

$$\mathbf{F_{vm}} = \frac{\rho V_p}{2} \frac{d}{dt} \left(\mathbf{u_p} - \mathbf{u} - \frac{a^2}{10} \nabla^2 \mathbf{u} \right) \,, \tag{1.9}$$

with a, the radius of the particle.

• *Stokes drag force:* The Stokes drag corresponds to the viscous drag caused by the difference in velocity between the particle and the surrounding fluid.

Maxey and Riley (1983) give:

$$\mathbf{F_{St}} = 6\pi a\mu\left(\mathbf{u_p} - \mathbf{u} - \frac{a^2}{6}\nabla^2\mathbf{u}\right) , \tag{1.10}$$

with a being the particle radius. The Laplacian term is the Faxen correction term added to account for the effect of the velocity curvature at low Reynolds number. A more general equation for the drag force is:

$$\mathbf{F_D} = \frac{C_D}{2}\pi a^2\rho\left(\mathbf{u_p} - \mathbf{u}\right) , \tag{1.11}$$

where C_D is the drag coefficient.

• *Buoyancy force:* Caused by a density difference between the fluid and the particle:

$$\mathbf{F_B} = (\rho_p - \rho_f)\frac{4}{3}\pi a^3 g\mathbf{e_g} , \tag{1.12}$$

where a is the particle radius, ρ_p its density and ρ_f the surrounding fluid density.

• *Basset history force:* It is another drag force, derived in Basset (1961). It describes the past effect of the particle on the flow due to the lagging boundary layer development caused by the changing relative velocity of bodies moving through a fluid, it is often added in models where the particles action on the fluid is not calculated in order to compensate for the past particle action on the fluid and its effect on the current particle velocity. It can be written as:

$$\mathbf{F_{bas}} = -6\pi a^2\mu\int_0^t d\tau\left(\frac{d_\tau\left[\mathbf{u_p}(\tau) - \mathbf{u}(\tau) - \frac{a^2}{6}\nabla^2\mathbf{u}\right]}{[\pi\nu(t-\tau)]^{1/2}}\right) . \tag{1.13}$$

• *Saffman lift force:* Velocity gradient in the flow causes a pressure differential which results on a lift force on the particle, first considered in Saffman (1965):

$$\mathbf{F_{Saf}} = 1.61\,a^2\left(\mu\rho\right)^{1/2}\left(\nabla\times\mathbf{u}\right)^{-1/2}\left[(\mathbf{u} - \mathbf{u_p})\times\nabla\times\mathbf{u}\right] . \tag{1.14}$$

The direction of the Saffman lift force depends on the velocity difference between the particle and the fluid. In the case of a pipe, if $(\mathbf{u} - \mathbf{u_p}) > 0$ the force is directed towards the highest velocity, corresponding to the centre of the pipe. If $(\mathbf{u} - \mathbf{u_p}) < 0$ the force is directed towards the lowest velocity, in the direction of the wall.

• *Magnus force*: corresponding to a lift force created by the particle rotation (Rubinow and Keller, 1961):

$$\mathbf{F_{Mag}} = \pi a^3\rho\left[(0.5\nabla\times\mathbf{u} - \omega_p)\times(\mathbf{u} - \mathbf{u_p})\right] . \tag{1.15}$$

1.2.2 Particle rotation rate

The rotation of the particles is one of the key elements of particulate flows dynamics. The rotation rate ω of a particle follows the equation:

$$\frac{dI\omega}{dt} + \omega \times I\omega = \mathbf{T}\,, \tag{1.16}$$

with I as the particle moment of inertia and $\mathbf{T}$ its torque. The moment of inertia of a spherical object is constant, $I = \frac{2m_p a^2}{5}$, therefore in the case of spherical particles $\omega \times I\omega = 0$. Equation (1.16) then becomes:

$$I\frac{d\omega}{dt} = \mathbf{T}\,. \tag{1.17}$$

The torque due to the action of the fluid on a particle is

$$\mathbf{T} = \int_{\partial V} r \times \sigma_T\, \hat{\mathbf{n}}\, \mathrm{d}S\,, \tag{1.18}$$

where ∂V is the surface of the particle, σ_T the stress tensor and $\hat{\mathbf{n}}$ a normalised vector direction orthogonal to the particle surface. The stress tensor of a Newtonian fluid is,

$$\sigma_{ij} = -p\,\delta_{ij} + \mu\left(\frac{\partial u_i}{\partial x_j} + \frac{\partial u_j}{\partial x_i}\right)\,, \tag{1.19}$$

where p is the pressure, μ the dynamic viscosity and δ_{ij} the Kronecker delta.

1.3 Particle modelling through modification of Navier-Stokes equation

Particulate flows are complex physical structures with a large number of parameters to consider, such as particle and fluid densities, particles size, rate of collision and aggregation among other things. To the complexity of the dynamics involved is added the inherent difficulty of considering, theoretically or numerically, a large number of independent objects. Particulate flows cannot realistically be exactly described, they need to be studied through a model making assumptions and approximations in order to simplify the problem while keeping as much as the underlying dynamics as possible. A number of models with a wide range of characteristics and physical assumptions have been developed during the last few decades, they can be classified into three general categories: *modification of the fluid phase equations of motion*, *Eulerian modelling of the particles phase* and *Lagrangian tracking models*. Another important characteristic is the way fluid and particles are coupled, one can characterise three levels of interaction between the fluid and particle phase of the model:

- *Four-way coupling* models have the fluid and particles fully coupled. Particle-particle interactions, notably collisions, are also included.
- *Two-way coupling* models neglect particle-particle interactions but the fluid and particles are still fully coupled.
- *One-way coupling* models, in this case the coupling is injective, either the fluid affects the particles, or the particles the fluid, there is no feedback.

The best suited model depends on the phenomenon studied and the degree of accuracy required, with a trade-off between how detailed a model is and the cost of computational cost associated. A non-exhaustive list of the main particulate flow models is given in Sections 1.3-1.5.
One of the simplest models is the dusty gas approach developed by Marble (1970). The model assumes small particles with a short relaxation time so that they act as tracer and follow the fluid perfectly. Thus the flow can be treated as a single fluid whose density varies as a function of the local particle concentration. The evolution of the flow can be described with a single equation of motion:

$$\partial_t \mathbf{u} + \mathbf{u} \cdot \nabla \mathbf{u} = -\frac{\nabla p}{(1+\kappa)\rho} + \frac{\nabla \cdot \tau}{(1+\kappa)\rho} \,, \tag{1.20}$$

with $\mathbf{u}$ the fluid velocity, p the pressure, ρ the fluid density, τ the viscous stress tensor and $\kappa = \rho_p/\rho$ the ratio between the particle and fluid densities. Marble (1970) assumes a uniform particle distribution, resulting in κ held constant. In the limit $\kappa \to 0$, the model retrieves the single phase flow equation of motion. Its simplicity make the dusty gas approach model straightforward to apply, but the validity of the results is limited due to the assumptions made are only valid in the small particles limit. Further, it does not take into account any of the particles characteristics except their density.

Using a similar concept as the dusty gas model, suspension rheology uses a variable apparent dynamic viscosity $\mu_s(\phi)$, with $\phi = V_p/V_f$ the particle volume concentration. μ_s is generally normalised by the viscosity of the single phase flow, such that the parameter worked with is $\mu_r = \mu_s/\mu_0$. Extensive work has been done on the topic, one can find a comprehensive literature review by Mueller et al. (2009). Different functions for the dynamic viscosity are used in function of the solid volume fraction. For the dilute regime, when $\phi < 10^{-2}$, the viscosity depends on the density in a linear fashion (Einstein, 1911). For semi-dilute flows, $10^{-2} < \phi < 0.25$, polynomial fits are used (Vand, 1948). In the case of dense flows ($\phi > 0.25$), more complex laws are used (Krieger, 1972; Mooney, 1951; Van den Brule and Jongschaap, 1991) Suspension rheology is a flexible method and has been adapted to many cases. In fact this model is, in spite of its limitations, one of the few permitting the study of non Newtonian particulate flows and non-spherical particles without a model for individual particles. Even so, because suspension rheology models presented in this section do not directly represent the particles, they are limited in scope as they do not give information about the behaviour of the particles.

1.4 Eulerian description models for particulate flows

Eulerian models make the continuity assumption for the solid phase, such that the solid phase can be characterised as a continuous medium rather than as an ensemble of distinct objects. This assumption still allows for a direct description of the particles instead of the indirect approach where the effect of the solid phase on the solid flow is computed through the modification of the fluid parameters, as seen in the previous section. A single equation of motion can be derived to describe the evolution of the solid phase characteristics, generally its velocities and local concentration, in an Eulerian frame of reference, using the conservation of the total particle mass and momentum.

1.4.1 Equilibrium Eulerian model

The equilibrium Eulerian approach has been first considered in De La Mora and Rosner (1981), developed in Ferry and Balachandar (2001) and improved in Ferry et al. (2003). The particles are described directly rather than through modifying a parameter of the fluid or its equation of motion. The model is one-way coupled i.e. the particle motion only depends on the surrounding fluid while the influence of the particles on the fluid is neglected. The particle velocity $\mathbf{u_p}$ is described by the following equation:

$$\mathbf{u_p} = \mathbf{u} + \mathbf{U_p} - St(1-\beta)\frac{D\mathbf{u}}{Dt} + \mathbf{U_p}\cdot\nabla\mathbf{u}\,, \tag{1.21}$$

where $\mathbf{u}$ is the velocity of the surrounding fluid and $\mathbf{U_p}$ the particle settling velocity, $\beta = 3/(2\rho+1)$ the density ratio parameter with $\rho = \rho_p/\rho_f$. St is the Stokes number representing the ratio between the particles and Kolmogorov timescales defined as:

$$St = \frac{\tau_p}{\tau_k} = \frac{2a^2\rho_t}{9\,\mu\,\phi(Re)\,\tau_k}\,, \tag{1.22}$$

where a is the particle radius, μ the kinematic viscosity of the fluid and $\phi(Re) = 1 + 0.15Re^{0.687}$ is the correction coefficient function of the Reynolds number. The equilibrium Eulerian model is expected to produce accurate results when the Stokes number is small and the particles closely follow the fluid trajectory, but loses its validity as the relaxation time of the particles increases. Ferry and Balachandar (2001) compared the Equilibrium Eulerian model to a more sophisticated model using Lagrangian particle tracking to model the particles trajectories, similar to the ones mentioned in Section 1.5.1. They found that the results obtained using the Equilibrium Eulerian model were consistent with the point particle model results up to $St = 0.2$. The equilibrium Eulerian model, while it captures a broader range of the particulate flow mechanisms compared to the models presented in Section 1.3,

including particles preferential concentrations. Nonetheless it is still one-way coupled and therefore does not account for the feedback of the particles on the fluid, limiting its scope.

1.4.2 Fully Eulerian approach

The study of the particles influence on stability requires, at a minimum, a two-way coupling model. An example of such model is the fully Eulerian model, early examples can be found in Di Giacinto et al. (1982) and Durst et al. (1984). The fluid and solid phases are treated as two inter-penetrating media. Two additional equations describe the particle motion and mass conservation. Klinkenberg et al. (2011) studied the linear stability of particulate plane Poiseuille flows with the fully Eulerian approach. The description of the fluid and particles motions are given by the following set of equations:

$$\frac{\partial \mathbf{u}}{\partial t} = -(\mathbf{u}\cdot\nabla)\mathbf{u} - \frac{\nabla p}{\rho} + \nu\nabla^2\mathbf{u} + \frac{KN}{\rho}(\mathbf{u_p}-\mathbf{u}) \,, \tag{1.23}$$

$$\frac{\partial \mathbf{u_p}}{\partial t} = -mN(\mathbf{u_p}\cdot\nabla)\mathbf{u_p} + KN(\mathbf{u}-\mathbf{u_p}) \,, \tag{1.24}$$

$$\frac{\partial N}{\partial t} = -\nabla\cdot(N\mathbf{u_p}) \,, \tag{1.25}$$

$$\nabla\cdot\mathbf{u} = 0 \,, \tag{1.26}$$

where $\mathbf{u}$ and $\mathbf{u_p}$ are the velocities of the fluid and particles respectively, N the number of particles per unit volume and p the pressure, m the particle mass, $K = 6\pi a\mu$ the Stokes drag, with a the particle radius and μ the fluid dynamic viscosity. The fully Eulerian model is, as a two-way coupled model, valid for larger particles than the dusty gas and equilibrium Eulerian models. It allows for the study of the effect of the particles on the fluid. Klinkenberg et al. (2011) estimate that the Eulerian two-way coupled model validity extends for volume density ratio up to 10^{-3}.

Additionally, Boronin and Osiptsov (2008) used a two-away coupled fully Eulerian model, albeit a more detailed one. Two fluid-particle interaction forces are taken into account. The Stokes force $\mathbf{f}_{St}$ and Saffman lift $\mathbf{f}_{Saf}$. Even when the particle volumetric concentration is very small, the particle mass fraction can be significant as the solid particles are much denser than the gas. The system of equations used is:

$$\nabla\cdot\mathbf{u} = 0 \,, \tag{1.27}$$

$$\partial_t\mathbf{u} = -\nabla p + \frac{1}{Re}\nabla^2\mathbf{u} - n\kappa\mathbf{f}_{St} - n\kappa\mathbf{f}_{Saf} \,, \tag{1.28}$$

$$\partial_t n + \nabla \cdot (n\mathbf{u_p}) = 0 \,, \tag{1.29}$$

$$\partial_t \mathbf{u_p} = \mathbf{f}_{St} + \mathbf{f}_{Saf} \,, \tag{1.30}$$

$$\mathbf{f}_{St} = \beta(\mathbf{u} - \mathbf{u_p}) \,, \qquad \mathbf{f}_{Saf} = K\mathbf{j}\left(\frac{\partial v}{\partial y}\right)^{1/2}(v - v_p) \,, \tag{1.31}$$

$$Re = \frac{\rho U_0 \delta}{\mu} \,, \qquad \kappa = \frac{mN_0}{\rho} = \frac{\rho_p}{\rho} \,, \qquad \beta = \frac{6\pi\sigma\mu\delta}{mU_0} \,, \tag{1.32}$$

$$K = \frac{6.46\sigma^2(\delta\mu\rho)^{1/2}}{mU_0^{1/2}} = \frac{6.46}{2\pi}\sqrt{\frac{\beta}{2}\frac{\rho}{\rho_p^0}} \,. \tag{1.33}$$

where $\mathbf{u}$ and $\mathbf{u_p}$ are the fluid and particles velocity (with v and v_p components perpendicular to the boundary), p is the pressure. $\kappa = m_p N_0/\rho$ is the particle to fluid density ratio with m_p a particle mass and ρ the fluid viscosity. β the particle inertia parameter. n is the local particle concentration and N_0 its value in the outer flow. $\mathbf{j}$ is the unit vector perpendicular to the flow direction, Three particle distributions N are considered: constant, exponential decay and increase as a function of the distance with the boundary layer y, the three concentrations:

$$N(y) = 1 + \exp(-y) \quad , \quad N(y) = 1 \quad , \quad N(y) = 1 - 0.5\exp(-y) \,. \tag{1.34}$$

The other parameters regarding the particles are the inertia parameter β which is equal to the ratio of the boundary layer thickness to the particle relaxation length, and is the inverse of the Stokes number. The second parameter is the particle mass concentration, α. Boronin and Osiptsov (2016) study the effect of particles on nonmodal instability and transient growth for particulate plane Poiseuille flows with a similar model. They used a nonuniform particle distribution with the particle concentrated in two Gaussian symmetric layers, the particle concentration $N_0(y)$ is expressed as the following equation:

$$N_0(y) = \frac{\alpha}{\rho} N_* \left(\exp\left[\frac{(y-\zeta)^2}{\xi^2}\right] + \exp\left[\frac{(y+\zeta)^2}{\xi^2}\right]\right) \,, \tag{1.35}$$

ζ determines the position of the concentration peak while ξ determines its width, ρ is the particle to fluid density ratio, α the average over the duct of the particle mass loading and N_* a scaling coefficient. Equation 1.35 has two peaks to reflect the particles profiles in real flows as particles tends to accumulate closer to walls in bounded flows (Osiptsov, 1988). The model uses a single effective velocity to represent the fluid-particle mixture, it assumes a small Stokes number, $St \ll 1$ as well as a Froude number, $Fr = (U_0/gL) \gg 1$, with U_0 the centreline fluid velocity, L the channel length and g the gravitational constant. A possible representation of $N_0(y)$ is given in Figure 1.1.

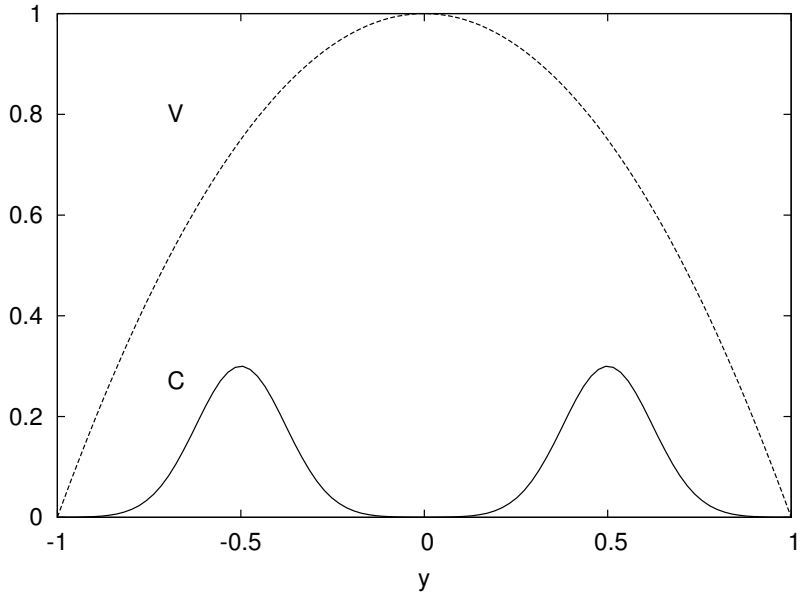

Figure 1.1: C is the profile type in the spanwise direction of particle concentration used in Boronin and Osiptsov (2016), V being the usual fluid mean velocity profile.

The fully Eulerian model can also be modified to account for polydisperse particle distributions (Fox et al., 2008).

1.5 Particulate flows models using Lagrangian particle tracking

The principal advantage of fully Eulerian approaches in modelling the solid phase comes from the continuous approximation made, the solid phase behaviour is expressed by a few equations and the number of particles does not influence the model. Therefore, the continuous approximation significantly simplify the solid phase modelling and lowers the computational cost involved. This is especially true for large number of particles. However, the continuous particles field approximation used in Eulerian models also has drawbacks as particles are not considered individually, preventing the study of particle-particle dynamics. A common method allowing the consideration of particles as discrete entities is to use Lagrangian tracking for the solid phase while the fluid phase is still modelled with an Eulerian framework. This allows one to capture a larger part of the particles dynamics than fully Eulerian models. Notably, polydisperse particle distributions, how the particles are distributed, collisions and particle rotation which are amongst the main drivers of the particle physics. Using Lagrangian particle tracking brings more flexibility in the characteristics considered and is closer to real life particulate flows. However, the computational cost is much higher due to the simulation of individual particles, with at least one equation per particle to consider. Another complication inherent

to Lagrangian particle tracking model is the necessity to convert values from the Eulerian mesh to the Lagrangian one in order to assess the interaction between fluid and particles.

1.5.1 Point particle model

One such Lagrangian model is the point particle method. The point particle-approximation describes each particle as a single point, significantly simplifying particles tracking and avoiding the need for meshing at the particle fluid boundary. The acceleration of particles is obtained using Newton's second law, it is equal to the sum of the forces applied by the flow. While the particles radius does not directly affect their description, it is still taken into account when determining particles trajectories as the forces terms can depend on the particle radius. The description of the particles using a Lagrangian framework is first used in (Migdal and Agosta, 1967). Maxey and Riley (1983) derived a more detailed equation for the evolution of a single rigid sphere in an undisturbed flow with the point particle approximation:

$$m_p \frac{d\mathbf{u_p}}{dt} = m_f \frac{D\mathbf{u}}{dt} + (m_p - m_f)\mathbf{g_i} - \frac{m_f}{2}\frac{d}{dt}\left(\mathbf{u_p} - \mathbf{u} - \frac{a^2}{10}\nabla^2\mathbf{u}\right)$$

$$- 6\pi a\mu\left(\mathbf{u_p} - \mathbf{u} - \frac{a^2}{6}\nabla^2\mathbf{u}\right) - 6\pi a^2\mu\int_0^t d\tau\left(\frac{\frac{d}{d\tau}\left[\mathbf{u_p}(\tau) - \mathbf{u}(\tau) - \frac{a^2}{6}\nabla^2\mathbf{u}\right]}{[\pi\nu(t-\tau)]^{1/2}}\right), \tag{1.36}$$

with $\mathbf{u_p}$ as the particle velocity, $\mathbf{u}$ the fluid dynamic velocity at the particle position, a the particle radius, μ the fluid viscosity, m_p the particle mass and m_f the fluid mass of a volume equal to the particle volume. The terms on the right side of the equation represent (from left to right) the pressure gradient of the flow, the buoyancy force, the added mass term to account for the additional inertia due to the fluid displacement, the Stokes drag and the Basset history force, due to the lagging boundary layer development caused by the changing relative velocity of bodies moving through a fluid. These forces have been mentioned in more detail in Section 1.2.

Point particle models have been mostly used for turbulent flows. Elghobashi (1991) used Equation (1.36) with a turbulent drag. Squires and Eaton (1991) use a similar model but neglect all the forces applied to the particles except for the Stokes drag, in this case the velocity of a particle i at a position $\mathbf{X^i}$ and time t is:

$$\frac{d\mathbf{u}_p^i}{dt} = \frac{\mathbf{u}(\mathbf{X^i}) - \mathbf{u}_p^i}{\tau_p}, \tag{1.37}$$

where τ_p is the relaxation time of the particles and $\mathbf{u}(\mathbf{X^i})$ the fluid velocity at a position $\mathbf{X^i}$.

Ferrante and Elghobashi (2003) used a two-way coupled model; the standard turbulent motion equation describes the fluid motion with an additional force term representing the effect of the particles. A simplified version of Maxey and Riley (1983), assuming heavy particles, is used for the particles motion:

$$\partial_t \mathbf{u} + \mathbf{u}\nabla \cdot \mathbf{u} = -\frac{\nabla p}{\rho} + \nu \nabla^2 \mathbf{u} - \mathbf{F} \,, \tag{1.38}$$

$$m_p \frac{d\mathbf{u}_p}{dt} = m_p \frac{(\mathbf{u} - \mathbf{u}_p)}{\tau_p} + (m_p - m_f)\,\mathbf{g} \,, \tag{1.39}$$

where m_p is the particle mass, m_f is the equivalent fluid mass, $\mathbf{g}$ the gravitational acceleration and τ_p the relaxation time of the particles. d/dt is the time derivative in the particle frame. $\mathbf{f}$ is the force exerted by the particles within the integration volume control onto the fluid and is equal to the sum of the force exerted by each of the N particles present in the volume:

$$\mathbf{F} = \frac{1}{m_p} \sum_{k=1}^{N} \mathbf{F}_k \,. \tag{1.40}$$

Point particles models can also be adapted to take collisions between particles into account. A four-way coupled model including binary particle collisions is introduced in Yamamoto et al. (2001). Fluid and particle motions are handled similarly to Ferrante and Elghobashi (2003), but Yamamoto's model also takes particle rotation and collisions into account. The collisions are determined by evaluating distance between particles between two time step, the particle velocities are assumed to be constant during this interval, such that the particle position between $\tau = t$ and $\tau = t + dt$ can be expressed as :

$$\mathbf{x}_i(\tau) = \mathbf{x}_i(t) + \tau\, u_{p_i} \,, \tag{1.41}$$

where $\mathbf{x_i}(\tau)$ is the position of the particle i at time τ, and $\mathbf{u_{p_i}}$ its velocity at time t. The distance between two particles i and j is then:

$$d(\tau) \;= \sqrt{(\mathbf{x}_i(\tau) - \mathbf{x}_j(\tau))^2} = \sqrt{((\mathbf{x}_i(t) + \tau\, u_{p_i}) - (\mathbf{x}_j(t) + \tau\, u_{p_j}))^2} \,. \tag{1.42}$$

Thus the distance between two particle is expressed by a quadratic function whose roots give potential collision times. The modification of a particle velocity caused by a collision between two particles is calculated using the equations of impulsive motion with a hard-particle assumption, detailed in Section 1.6. The particles rotational velocity $\boldsymbol{\omega}_\mathbf{p}$ is given by:

$$\frac{d\boldsymbol{\omega}_\mathbf{p}}{dt} = -\frac{C_T \rho_f}{2} a^5 |\boldsymbol{\omega}_\mathbf{r}| \boldsymbol{\omega}_\mathbf{r} \,, \tag{1.43}$$

where a is the particle radius, $\omega_\mathbf{r}$ the relative rotation rate and C_T a non-dimensional coefficient depending on the particle Reynolds number.

Another method working on similar assumptions as the point particle model is the discrete element method (sometimes called Distinct Element Method), developed by Cundall and Strack (1979). The behaviour of the particles is determined through the contact and non-contact forces acting on them. The Discrete element method has more of an emphasis particle-particle interactions, with a more sophisticated model for collisions and the inclusion of non-contact forces. The governing equations for the translational and rotational velocity of a particle i of mass m_{p_i} and moment of inertia I_i are:

$$m_{p_i}\frac{d\mathbf{u_i}}{dt} = \sum_j \mathbf{F}^c_{ij} + \sum_k \mathbf{F}^{nc}_{ik} + \mathbf{F}^f_i \ , \tag{1.44}$$

$$I_i\frac{d\omega_\mathbf{i}}{dt}\sum_j \mathbf{M}_{ij} \ , \tag{1.45}$$

where $\mathbf{u_i}$ and $\omega_\mathbf{i}$ are the particle translational velocity respectively. $\mathbf{F}^c_{ij}$ and $\mathbf{M}_{ij}$ are the contact force and torque acting on particle i by particle j or the walls, $\mathbf{F}^{nc}_{ik}$ the non-contact forces acting on particle i and $\mathbf{F}^f_i$ the fluid-particle interaction force. For each of the force considered, different terms can be added in function of the parametric range and the phenomenon studied. An overview is given in Zhu et al. (2007). Averaging methods can be used to describe the model continuously, in general to study granular flow (Zhu and Yu, 2002). The effect of collisions are calculated through a hard-particle or soft-particle models, more details are given in Section 1.6.

The point-particle models, and the discrete element method in particular, take a larger part of the physics into account than Eulerian models. Therefore, they are valid on a larger range of parameters. Moreover, particles are considered individually, such that it is easier to study their behaviour. One can also consider polydisperse distributions or particles with varying densities. However, at least one equation is associated to each particle, and additional computations are required to for the collisions between particles. It follows that the computational cost is much higher, especially when a large number of particles is considered.

1.5.2 Immersed boundary model

The immersed boundary method (IBM), created by Peskin (1972), was first used to compute the flow around heart valves, a challenging problem due to the flexible boundaries of the valves. The immersed boundary method has since been adapted to particulate flows (Peskin, 2002; Uhlmann, 2005). Interactions between fluid and particles are calculated through an elastic force density $\mathbf{f}/\mathbf{F}$ (for the Eulerian/Lagrangian formulations respectively). The main point of IBM is that the particles are fully modelled, allowing for a more accurate description of the particulate flow than the other models

seen so far. The fluid behaviour is given by the standard Navier-Stokes equations:

$$\rho\left(\partial_t \mathbf{u} + \mathbf{u}\cdot\nabla\mathbf{u}\right) + \nabla p = \mu\nabla^2\mathbf{u} + \mathbf{F}\,, \tag{1.46}$$

$$\nabla\cdot\mathbf{u} = 0\,, \tag{1.47}$$

where $\mathbf{u}$ is the fluid velocity, ρ its density and ν the kinematic viscosity. $\mathbf{f}$ is the force applied by the particles to the fluid. The Lagrangian-Eulerian transformation is done through a Dirac function δ, with $\mathbf{X}(q,r,s,t)$ the position curvilinear coordinates and $\mathbf{x}(x_1,x_2,x_3)$ the position in Cartesian coordinates. Uppercase letters are used for variables in the Lagrangian coordinates and lowercase letters for the variables in the Eulerian coordinates system. The conversion from curvilinear to Lagrangian coordinates for the fluid parameters is given by:

$$\rho(\mathbf{x},t) = \int_\Sigma \mathbf{M}(q,r,s)\delta(\mathbf{x}-\mathbf{X})\,\mathrm{d}q\,\mathrm{d}r\,\mathrm{d}s\,, \tag{1.48}$$

$$\mathbf{f}(\mathbf{x},t) = \int_\Sigma \mathbf{F}(\delta(\mathbf{x}-\mathbf{X})\,\mathrm{d}q\,\mathrm{d}r\,\mathrm{d}s\,, \tag{1.49}$$

$$\partial_t\mathbf{X}(q,r,t,s) = \mathbf{U}(\mathbf{X},t) = \int_\Sigma \mathbf{u}(\mathbf{x},t)\delta(\mathbf{x}-\mathbf{X})\,\mathrm{d}x\,. \tag{1.50}$$

Since the Dirac function is singular, it cannot be implemented in a numerical scheme. A smoothed Dirac function $\delta_h(\mathbf{x})$ is used to circumvent the problem:

$$\delta_h(\mathbf{x}) = \frac{1}{h^3}\,\phi\left(\frac{x_1}{h}\right)\phi\left(\frac{x_2}{h}\right)\phi\left(\frac{x_3}{h}\right)\,, \tag{1.51}$$

ϕ is a continuous function of the distance h, derivation details are given in Peskin (2002). The method is adaptable and can be used in different configurations, for example the dynamics of an elastic material.

Later, the immersed boundary method has been adapted in Uhlmann (2005) to be more suitable to particulate shear flows. The effect of the particle on the fluid is given through the force term, the term is equal to zero in nodes without particles. Each particles has a mesh on its surface, comprised of N_L evenly distributed points called Lagrangian force points (Uhlmann, 2005). The number of mesh points used for a particle of diameter r_c is

$$N_L \simeq \frac{\pi}{3}\left(\frac{12r_c^2}{h^2}+1\right)\,, \tag{1.52}$$

where h is the mesh width. These points follow the rigid body motion of the particle:

$$\mathbf{V}_d^i(X) = \mathbf{v}_c^i + \boldsymbol{\omega}_c\times\left(\mathbf{X}-\mathbf{x}_c\right)\,, \tag{1.53}$$

with $\mathbf{v}_c$ and ω_c being the velocity and angular velocity at the centre of the particle $\mathbf{x}_c$. The conversion between Eulerian and Lagrangian meshes uses the same function δ_h as Peskin (2002), so that:

$$\mathbf{U}(\mathbf{X}_l^{(m)}) = \sum \mathbf{u}(\mathbf{x})\delta_h(\mathbf{x}-\mathbf{X}_l^{(m)})h^3 \ , \mathbf{f}(\mathbf{x}) = \sum_{m=1}^{N_p}\sum_{l=1}^{N_L} \mathbf{F}(\mathbf{X}_l^{(m)})\delta_h(\mathbf{x}-\mathbf{X}_l^{(m)})\,\Delta V_l^{(m)} \ . \tag{1.54}$$

Kidanemariam and Uhlmann (2014a) extended and improved the immersed boundary method, including particle-particle interactions and sedimentation. Collisions are described with a force composed of an elastic, a damping and a frictional component when the distance between particles goes below a chosen threshold (Kidanemariam and Uhlmann, 2014b; Patankar and Joseph, 2001).

The Distributed Lagrange Multiplier method is a variant of the immersed boundary method developed by Glowinski et al. (1999). The main feature of the approach is the combination of the equations of motion for the fluid and particles into a single combined equation using a weak formulation of the problem. A variant of the standard fluid equations is used both outside and inside the particle; the flow inside particles is constrained by a rigid body motion. The distance between two points is kept constant, as in Equation (1.53), using a Lagrange multiplier representing the body force per unit volume needed to maintain the rigid-body motion inside the particle boundary. The Distributed Lagrange Multiplier model has the advantage of not requiring the explicit computation of hydrodynamics forces and torques.

Considering a domain Ω, the time-dependent part of the domain filled by particles is called $P(t)$ The fluid velocity is described by the standard equation of motion,

$$\rho_f \frac{d\mathbf{u}}{dt} = \rho_f \mathbf{g} + \nabla\cdot\tau \quad \text{in } \Omega\backslash P(t) \ , \tag{1.55}$$

where ρ_f is the particle density and τ the stress tensor. For the particle velocity $\mathbf{U_i}$ of a given particle i, Newton's second law yields:

$$m_i \frac{d\mathbf{U}_i}{dt} = m_i\mathbf{g} + \mathbf{F}_i + \mathbf{F}_i' \quad \text{in } P(t) \ , \tag{1.56}$$

where m_i is the particle mass and g is the gravitational force. $\mathbf{F}_i$ represents the effect of hydrodynamic forces on the particles. For high particle concentrations, the increase in near-collisions events leads to a marked increase in the number of grids points necessary to the simulation. This issue is mitigated by the addition of a fictitious repulsive force term $\mathbf{F}_i'$. The fictitious repulsive force exerted on the i^{th} particle is:

$$\mathbf{F}_i' = \sum_{\substack{j=1\\ j\neq 1}}^{N} \mathbf{F^p}_{ij} + \sum_{j=1}^{4} \mathbf{F^w}_{ij} \ , \tag{1.57}$$

where N is the numbers of particles, $\mathbf{F^p}$ the particle-particle repulsive force and $\mathbf{F^w}$ the particle-wall repulsive force. The particle-particle repulsive force between the i^{th} and j^{th} particles is given by:

$$\mathbf{F^p}_{ij} = \begin{cases} 0, & \text{if } d_{ij} > a_i + a_j + l_0. \\ \frac{1}{\varepsilon_c}(\mathbf{X_i} - \mathbf{X_j})(a_i + a_j + l_0 + d_{ij})^2, & \text{if } d_{ij} \leq a_i + a_j + l_0, \end{cases} \tag{1.58}$$

where $\mathbf{X}$ is the particle position, a its radius, d_{ij} is the distance between the two particles' center, l_0 the cut-off range and ε_c a (positive) swiftness parameter.

The addition of $\mathbf{F}'_i$ in Equation (1.56) prevents collisions between particles, thus avoiding the necessity of adding another set of equations to describe them. The same method is used for particle-wall collisions. The particle angular velocity is:

$$\frac{d}{dt} I_i \omega_i = \mathbf{T}_i \quad \text{in } P(t)\,, \tag{1.59}$$

with I_i being the moment of inertia and $\mathbf{T}_i$, the torque of the particle i. Equations (1.46), (1.56) and (1.59) are combined using a weak formulation in a single equation valid in the entire domain with the addition of a combined velocity space, $\mathbf{v}$ valid in $\Omega \backslash P(t)$ and $\mathbf{V}; \xi$, valid in $P(t)$ to incorporate the rigid body motion in the particles,

$$\begin{aligned} &\int_\Omega \rho_f \left(\frac{d\mathbf{u}}{dt} - \mathbf{g} \right) \cdot \mathbf{v}\, d\mathbf{x} - \int_\Omega p \nabla \cdot \mathbf{v} d\mathbf{x} + \int_\Omega 2\nu \mathbf{D}[\mathbf{u}] : \mathbf{D}[\mathbf{v}] d\mathbf{x} \\ &+ \left(1 - \frac{\rho_f}{\rho_p} \right) \left(M \left(\frac{d\mathbf{U}}{dt} - \mathbf{g} \right) \cdot \mathbf{V} + I \frac{d\omega}{dt} \xi \right) - \mathbf{F}' \cdot \mathbf{V} = \langle \lambda, \mathbf{v} - (\mathbf{V} + \xi \times \mathbf{r}) \rangle_{P(t)}\,, \end{aligned} \tag{1.60}$$

where λ is the Lagrange multiplier used to enforce the rigid-body motion condition. The particles motion is on a distinct mesh, the data is then linearly interpolated between the fluid and particle meshes.

Immersed boundary models are close to real-life particulate flows. However, they are very computationally demanding and thus far have been limited to low particle numbers, small domains and a limited number of runs.

1.5.3 Fully Lagrangian models

One can also approximate the fluid as a set of particles, so that a Lagrangian mesh can be used for the fluid. Fully Lagrangian methods include the smoothed particle hydrodynamics (SPH) method, first used in astrophysics to describe stellar models (Gingold and Monaghan, 1977) and expended to particulate flows (Monaghan, 2012, 1992), as well as moving particle semi-implicit (MPS) method

(Koshizuka and Oka, 1996). In both cases the motion of the fluid particles and solid particles depends on their interaction with the other particles of the flow. This interaction is controlled by a weight function or a chosen kernel function, with a range limit, to evaluate quantities at the particles position. For a given continuous quantity $\mathbf{f}$ one obtain

$$\mathbf{F}(\mathbf{r}) = \int \mathbf{f}(\mathbf{r}')\mathbf{W}(\mathbf{r}-\mathbf{r}',h)\mathrm{d}\mathbf{r}' \,, \tag{1.61}$$

where $\mathbf{W}$ is the kernel function to evaluate interactions between fluid particles, $\mathbf{r}'$ the differential volume element and h the length scale. $\mathbf{W}$ is normalised such that:

$$\int \mathbf{W}(\mathbf{r}-\mathbf{r}',h)\mathrm{d}\mathbf{r}' = 1 \,. \tag{1.62}$$

The integral in equation 1.61 is approximated by a Riemann summation over the particles to obtain the discrete value, for a particle j:

$$\mathbf{F}_j(\mathbf{r}) = \sum_i m_i \frac{W_i}{\rho_i}\mathbf{W}(\mathbf{r}-\mathbf{r_i},h) \,, \tag{1.63}$$

where m_i is the mass, ρ_i the density and $\mathbf{r_i}$ the position of the particle i. In theory the summation is done over all the particles. In practice $\mathbf{W}$ is chosen such that its value quickly falls off with the distance and that the effect of particles whose distance is larger than $2h$ can be neglected (Monaghan, 2005). Only the kernel is space dependant, thus the spatial derivative of $\mathbf{f}$ is:

$$\frac{\partial \mathbf{F_j}(\mathbf{r})}{\partial \mathbf{x}} = \sum_i m_i \frac{W_i}{\rho_i}\frac{\partial \mathbf{W}}{\partial \mathbf{x}} \,. \tag{1.64}$$

Navier-Stokes equations are written, within this model, as:

$$\frac{D\rho_j}{Dt} = \sum_i m_i \mathbf{u}_{ji}\frac{\partial \mathbf{W_{ji}}}{\partial \mathbf{x}_j} \,, \tag{1.65}$$

$$\frac{D\mathbf{u}_j}{Dt} = -\sum_i m_i \left(\frac{\sigma_j}{\rho_j}+\frac{\sigma_i}{\rho_i}\right)\frac{\partial \mathbf{W_{ji}}}{\partial \mathbf{x}_j} + \mathbf{F}_j \,, \tag{1.66}$$

where $\mathbf{u}_{ji} = \mathbf{u}_j - \mathbf{u}_i$, σ is the total stress tensor and F is the external forces. Because they are mesh-free, these methods are well-adapted to shifting boundaries and have been used to study two-phase flows with a DEM-SPH method (Sakai et al., 2012; Sun et al., 2013) combining an SPH approach for the fluid and a direct element method for the particles where each particle velocity $\mathbf{u_p}$ is given by second Newton's law:

$$m_p \frac{d\mathbf{u_p}}{dt} = \sum \mathbf{F_i} \,, \tag{1.67}$$

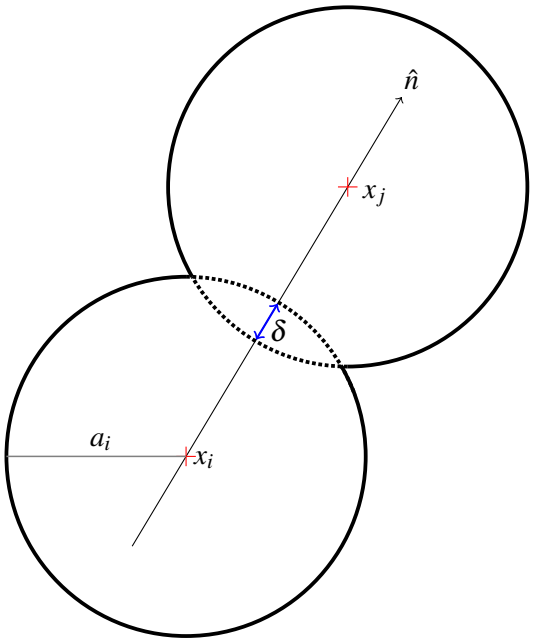

Figure 1.2: Illustration of the collision between particles i and j.

with $\mathbf{F_i}$ being the forces applied on the particles, such as drag force, buoyancy and contact forces. The solid and liquid phases are coupled using a kernel function as well. The DEN-SPH model has the same advantages and drawbacks as other Lagrangian models, the accuracy of the model is high as only minimal approximations are made but the large number of particles involved lead to high computational costs.

1.6 Collision processing

Four-way coupled models take into account particle-particle interactions, notably collisions. Several models of varying complexity can be used to compute the effect of a collision on the particles trajectories. The hard-particle collision model, used for example in Yamamoto et al. (2001), assumes that particles are not deformed during a collision, that the collision is instantaneous and involves at most two particles at a time, allowing for simplified collision dynamics. The conservation of momentum, both linear and angular, is used to compute the new velocity and angular velocity after a collision. Many models already assume the case of rigid particles; in these cases, the hard-particle collision model does not require additional assumption. For a collision between particles i and j, the particles translational velocities yields:

$$m_i(\mathbf{u_i^+} - \mathbf{u_i^-}) = \mathbf{J} \quad \Rightarrow \quad \mathbf{u}_i^+ = \mathbf{u_i^-} + \frac{\mathbf{J}}{m_i}\,, \tag{1.68}$$

$$m_j(\mathbf{u}_\mathbf{j}^+ - \mathbf{u}_\mathbf{j}^-) = -\mathbf{J} \quad \Rightarrow \quad \mathbf{u}_j^+ = \mathbf{u}_\mathbf{j}^- - \frac{\mathbf{J}}{m_j}\,, \tag{1.69}$$

with $\mathbf{J}$ the momentum transferred from one particle to the other, $\mathbf{u}$ the velocity, with the superscripts $+/-$ representing the value of a variable before and after the collision. The particles angular velocity change is given by:

$$I_i(\omega_i^+ - \omega_i^-) = a_i\hat{\mathbf{n}} \times \mathbf{J} \quad \Rightarrow \quad \omega_i^+ = \omega_i^- + \frac{a_i}{I_i}(\hat{\mathbf{n}} \times \mathbf{J})\,, \tag{1.70}$$

$$I_j(\omega_j^+ - \omega_j^-) = (a_i\hat{\mathbf{n}}) \times (-\mathbf{J}) \quad \Rightarrow \quad \omega_j^+ = \omega_j^- + \frac{a_j}{I_j}(\hat{\mathbf{n}} \times \mathbf{J})\,, \tag{1.71}$$

where I is the moment of inertia, a is the particle radius and ω the angular velocity. The expression of the momentum transfer $\mathbf{J}$ can be written in terms of normal and orthogonal components:

$$\mathbf{J} = (\mathbf{J}\cdot\hat{\mathbf{n}})\hat{\mathbf{n}} + (\mathbf{J}\cdot\hat{\mathbf{s}})\hat{\mathbf{s}}\,, \tag{1.72}$$

$$\hat{\mathbf{n}} = \frac{\mathbf{x}_i - \mathbf{x}_j}{d_{ij}} \quad ; \quad \hat{\mathbf{s}} = \frac{\Delta\mathbf{u} - [\Delta\mathbf{u}\cdot\hat{\mathbf{n}}]\hat{\mathbf{n}}}{|\,\Delta\mathbf{u} - [\Delta\mathbf{u}\cdot\hat{\mathbf{n}}]\hat{\mathbf{n}}\,|}\,, \tag{1.73}$$

with $\hat{\mathbf{n}}$ being the unit normal vector which goes through the centre of the two particles $\mathbf{x}_i$ and $\mathbf{x}_j$, as illustrated in Figure 1.2. It is orthogonal to the contact plane, d_{ij} is the distance between the centre of the particles i and j. The tangential unit vector, $\hat{\mathbf{s}}$, is orthogonal to $\hat{\mathbf{n}}$ and points in the direction of the relative velocity $\Delta\mathbf{u}$, defined as:

$$\Delta\mathbf{u} = (\mathbf{u_i} - \mathbf{u_j}) - (\omega_i \times a_i\hat{\mathbf{n}} + \omega_j \times a_j\hat{\mathbf{n}})\,. \tag{1.74}$$

The value of $\mathbf{J}$ in the normal direction is

$$\mathbf{J}\cdot\hat{\mathbf{n}} = m'(1+\varepsilon_N)(\Delta\mathbf{u}^-\cdot\hat{\mathbf{n}})\,, \tag{1.75}$$

where ε_N is the coefficient of restitution.

ε_N is bounded between 0 for a completely inelastic collision and 1 for a perfectly elastic collision. The value of $\mathbf{J}$ in the tangential direction is then:

$$\mathbf{J}\cdot\hat{\mathbf{s}} = \left(\frac{1}{m'} + \frac{a_i^2}{I_i} + \frac{a_j^2}{I_j}\right)^{-1}(1+\varepsilon_S)(\Delta\mathbf{u}^-\cdot\hat{\mathbf{s}})\,, \tag{1.76}$$

where m' is the effective mass such that: $\frac{1}{m'} = \frac{1}{m_i} + \frac{1}{m_j}$. The tangential coefficient of restitution is given by $\varepsilon_S \in [-1,\ 1]$, where $\varepsilon_S = -1$ corresponds to a frictionless collision and $\varepsilon_S = 1$, to a perfectly elastic one. $\varepsilon_S = 0$ corresponds to the no-slip case. Substituting Equations (1.75) and (1.76) into

Equation (1.72) yields:

$$\mathbf{J} = m'(1+\varepsilon_N)(\Delta\mathbf{u}^- \cdot \hat{\mathbf{n}})\hat{\mathbf{n}} + \left(\frac{1}{m'} + \frac{a_i^2}{I_i} + \frac{a_j^2}{I_j}\right)^{-1}(1+\varepsilon_S)(\Delta\mathbf{u}^- \cdot \hat{\mathbf{s}})\hat{\mathbf{s}}\,. \tag{1.77}$$

For a spherical particle of radius a, $I = 2/5\,ma^2$. The expression of $\mathbf{J}$ can be simplified as:

$$\mathbf{J} = m'(1+\varepsilon_N)(\Delta\mathbf{u}^- \cdot \hat{\mathbf{n}})\hat{\mathbf{n}} + \frac{2}{7}m'(1+\varepsilon_S)(\Delta\mathbf{u}^- \cdot \hat{\mathbf{s}})\hat{\mathbf{s}}\,. \tag{1.78}$$

As opposed to the hard-particle model, the soft-particle collision model accepts an overlap δ_0 between the two particles during a collision (as seen in Figure 1.2). However, it is assumed that the particles retain their shape during a collision so this model is limited to small deformations of the particles. The forces are divided between the normal component in the direction of $\hat{\mathbf{n}}$ and the tangential component along $\hat{\mathbf{s}}$. This category includes two models, the *Hertzian contact approximation* and the *Linear spring dashpot* model. The *Hertzian approximation*, first developed by Hertz (1882), assumes a small area of contact compared to the particles size. Moreover, the friction is neglected. The equation for a pure elastic deformation is of the form:

$$m_i\ddot{\mathbf{x}}_i = \mathbf{F}_i = -k_{Hz}\delta^{3/2}\,, \tag{1.79}$$

$$m_j\ddot{\mathbf{x}}_j = \mathbf{F}_j = k_{Hz}\delta^{3/2}\,. \tag{1.80}$$

with $\delta(t) = \mathbf{x}_i - \mathbf{x}_j < \delta_0$, the overlap between the particles.

The initial conditions are $\delta(0) = 0$ and $\dot{\delta}(0) = \Delta\mathbf{u}$. k_{Hz} is the Hertzian stiffness given by:

$$k_{Hz} = \frac{4}{3}a'^{1/2}E'\,, \tag{1.81}$$

where a' is the effective particle radius defined as: $\frac{1}{a'} = \frac{1}{a_i} + \frac{1}{a_j}$ and E' is the effective Young's modulus, defined such that $\frac{1}{E'} = \frac{1-\nu_i}{E_i} + \frac{1-\nu_j}{E_j}$.

The *Linear spring dashpot model* was introduced in Cundall and Strack (1979), the spring represents the elastic deformation and the dashpot represents the viscous dissipation occurring during the collision. The model is, as the previous one, valid only for small particles overlap and has been used by Sun et al. (2013). The overlap equation between two particles is represented by a second order ordinary differential equation:

$$m'\ddot{\delta} + \nu_c\dot{\delta} + k_c\delta = \ddot{\delta} + 2\lambda\dot{\delta} + \omega_0^2\delta = 0\,, \tag{1.82}$$

where k_c is the spring stiffness, ν_c is the damping coefficient, λ is the damping ratio and ω_0 is the undamped natural frequency. Equation (1.82) solution is of the form:

$$\delta(t) = A(\dot{\delta}(0)/\Omega)\exp\left(-\frac{\lambda}{2}t\right)\cos(\omega_1 t - \phi_c)\,, \tag{1.83}$$

with

$$\omega_1 = \left(\omega_0^2 - \frac{\lambda^2}{4}\right)^{0.5}. \tag{1.84}$$

The initial conditions at the time of contact are $\delta(0) = 0$ and $\dot{\delta}(0) = \dot{\delta}_0$, where $\dot{\delta}_0$ is the difference between the two particles velocity at the time of collision. With these two conditions, one can find the value of A and ϕ, replacing A and ϕ in Equation (1.83) yields:

$$\delta(t) = \frac{\dot{\delta}_0}{\omega_1}\exp\left(-\frac{\lambda}{2}t\right) \quad \text{and} \quad \cos\left(\omega_1 t - \frac{\pi}{2}\right)\,. \tag{1.85}$$

The particle angular velocity can also be described with a second order ordinary differential equation and derived using the same method.

Another mechanism is the aggregation of particles. Aggregation mainly occurs for small or sticky particles in dense suspensions. As this work focus on dilute and semi-dilute suspensions, aggregation is not relevant.

1.7 Summary of particles modelling methods

The models presented have diverse characteristics and the best suited model depends on the phenomena studied. A summary of the models used for particulate flows presented in this work is given in Table 1.1, giving each model characteristics and physical assumptions under which it is valid.

Model	Characteristics	Physical assumptions
Modified fluid eqs.	Modified Navier-Stokes equations depending on particle volume concentration (dusty gas method) Variable viscosity dependent on the particle volume concentration (suspension rheology).	One-way coupling (particle $\rightarrow$ fluid). Small particles act as tracers (in the limit of very small Stokes number), considers a homogeneous particle distribution with monodisperse spherical particles.
Eulerian modelling		

Equilibrium Eulerian	Particle velocity depends only on the surrounding fluid characteristics.	One-way coupling (fluid → particle), particles are assumed to be very small, monodisperse and spherical.
Fully Eulerian	Particles are approximated as a continuous medium. Fluid and particles phases are treated as inter-penetrating media.	Two-way coupling, allows for larger particles than the models above, as well as polydisperse particles, but particles are still assumed to be spherical.
Mesoscopic Eulerian formalism	Models turbulent flows by combining a Eulerian for fluid-particle interactions and Lagrangian approach for random motion.	One-way coupling (fluid → particle), monodisperse spherical particles.
Lagrangian particle tracking		
Point particle model	Particles are approximated as points, each particle is associated with its equation of motion.	Two or four-way coupling, particles are still assumed to be small, can handle polydisperse as well as nonspherical particles.
Immersed boundary model	Fully modelled particles, the fluid-particle interactions are defined through an elastic force. A combined Lagrangian - Eulerian method is used.	Four-way coupling, no particle size limit, well suited for particles with complex shapes and flexible boundaries.
Fully Lagrangian	Both fluid and solid phases are modelled as particles	Four-way coupling, possibility for polydisperse particles distributions and particles of nonspherical shape.

Table 1.1: List of the different methods usable for particles modelling with their associated characteristics

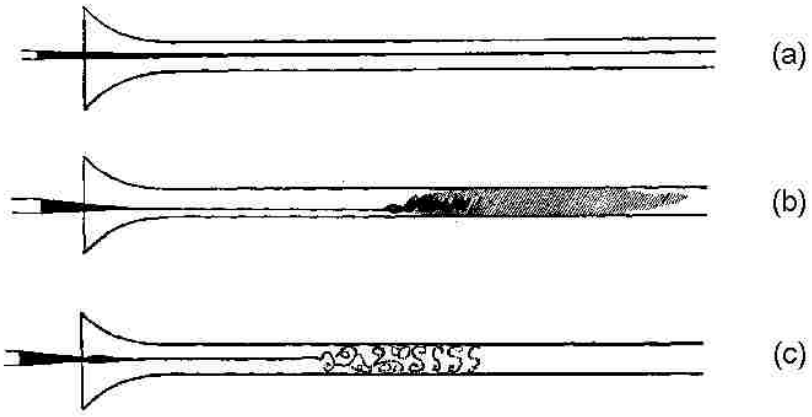

Figure 1.3: Illustrations of laminar (a), transitional (b), and turbulent (c) flows from Reynolds experiment (image from Reynolds (1883)).

1.8 Stablity in single phase flows

The stability of pipe flow has been extensively studied in the literature. The first study of flow stability was the experimental work of Reynolds (1883) from which the concepts of laminar flow, turbulent flow and transitional flow in a pipe are originated; these three states are illustrated in Figure 1.3. Reynolds found that the state of the flow is governed by a single dimensionless parameter, the Reynolds number $Re = \frac{UL}{\nu}$, with L a characteristic length of the flow (here the diameter of the pipe), U its characteristic velocity and ν the kinematic viscosity. In a pipe, the flow exhibits the first signs of turbulence for Reynolds number ranging from 2000, to 13000, depending on the initial conditions and the smoothness of the pipe. The transition to turbulence is not a straightforward process. It depends on several parameters and the distinction between transitional flow and turbulent flow can be difficult to define. Adding particles furthermore increases the complexity of the process. Numerous theoretical models have been created in the last decade to describe the conditions of the transition to turbulence in shear flows. A steady flow is stable to a perturbation if the perturbation energy converges towards 0 in the limit of infinite times. Mathematically, this writes out as:

$$\lim_{t\to\infty} \frac{E(t)}{E(0)} \to 0\,, \tag{1.86}$$

where $E(0)$ is the perturbation initial energy. There are other way of defining stability relying on more stringent conditions. A flow is said to be *conditionally stable* if there exists a threshold energy E_T such that for any initial energy $E(0) < E_T$, the flow is stable. If the threshold is infinite the flow is *globally stable*. In the other hand if the flow is unstable even to infinitesimal perturbations, it is *linearly unstable*. Finally, a flow is defined as *monotonically stable* if the amplitude of all perturbation decreases at all times. In the case of the single phase pipe flow the critical Reynolds number for monotonic stability is $Re_{E_f} = 81.5$ (Schmid and Henningson, 2012).

1.8.1 Linear stability analysis

Mathematically, Equation (1.4) is linearised around a steady state $\mathbf{U}$, in the case of the pipe flow the steady state is called the Hagen-Poiseuille flow with, for a cylindrical set of coordinates $(\mathbf{r}, \theta, \mathbf{z})$: $\mathbf{U} = (1-r^2)\hat{\mathbf{z}}$. The stability of the flow is then studied through the addition of a small perturbation $\mathbf{u}'$ to this steady solution. The perturbation has a wavelike solution: $\mathbf{u}' = u(r)\exp(i(\alpha z + m\theta - \omega t))$ where α and m are the wavenumbers of the perturbation and the real and imaginary parts of ω correspond to the perturbation frequency and growth rate respectively. Additionally, Squire's theorem states that for incompressible shear flows, including pipe flows, if there is, for a given Reynolds number Re_{3D}, a three-dimensional perturbation for which the flow is linearly unstable, then also exists a two-dimensional disturbance for which the flow is linearly unstable at a Reynolds number $Re_{2D} < Re_{3D}$. Using a streamfunction φ, Equation (1.4), whose velocity is originally three-dimensional, with $\mathbf{u} = u_1\mathbf{e_1} + u_2\mathbf{e_2} + u_3\mathbf{e_3}$, can be rewritten as a single equation, first derived in Orr (1907) and called the Orr-Sommerfeld equation:

$$\frac{1}{i\alpha Re}\left(\partial_z^2 - \alpha^2\right)^2 \varphi = (U-\omega)\left(\partial_z^2 - \alpha^2\right)\varphi - U''\varphi \,, \tag{1.87}$$

where $c = \omega/\alpha$ is the phase speed. Equation (1.87) can be arranged in a matrix form:

$$i\omega\mathbf{A}\varphi = \mathbf{B}\varphi \,, \tag{1.88}$$

this system can be solved to find the value of ω and to assess the linear stability of the flow.

Schmid and Henningson (2012) gave an overview on stability analysis for shear flows, including pipe Poiseuille flows. A flow is globally stable if a perturbation of any amplitude decay exponentially, Joseph and Carmi (1969) found that the pipe flow is energetically stable (any perturbation monotonically decreases at all times) for $Re < 81.49$. Another concept is the linear stability of flow, in order to study linear stability an infinitesimal perturbation is added to the flow. Given sufficient time, the perturbation must either decay away with the flow returning to the laminar state or grow into a much larger disturbance. If all such perturbations to the flow eventually decay away then the flow is linearly stable, so that an infinitesimal perturbation cannot trigger transition. Pipe flows are considered to be linearly stable for all Reynolds number, even though there is no definitive theoretical proof as of yet, there is significant evidence. Sexl (1927) give a theoretical proof for inviscid flow. Pfenniger (1961) managed to experimentally delay the transition to $Re = 10^6$ by suppressing ambient perturbations. Numerically speaking, linear stability has been studied using eigenvalue analysis (Lessen et al., 1968) and pipe flow has been found to be linearly stable, Meseguer and Trefethen (2003) studied the stability for Reynolds numbers up to $Re = 10^7$ and did not find linear instability either. The linear stability analysis of a flow is a very convenient tool to study the stability of a flow. However, the study of infinitesimal perturbations only gives limited information on the flow behaviour, as most shear flows

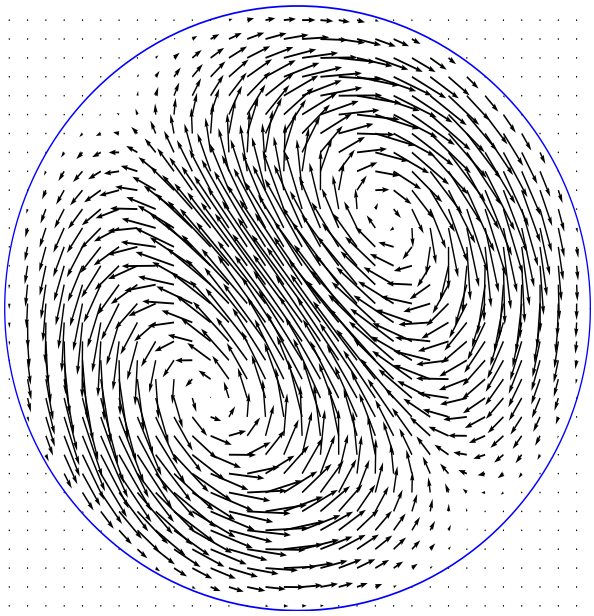

Figure 1.4: Cross-section of the optimal perturbation for a linearised pipe flow.

exhibit subcritical transition. In single phase pipe flow in particular the linear stability analysis results do not match experimental results, since transition to turbulence is observed for Reynolds number around 2000 while it is linearly stable for any Reynolds number.

1.8.2 Transient growth analysis

Linear stability analysis focus on the long term decay or growth of a perturbation, before this eventual decay, however, perturbations can initially grow over a finite period of time. The transient growth corresponds to the ratio between the maximum energy a flow can have at a time T, E_T for a perturbation of energy E_0,

$$G(T,Re) = \max_{\mathbf{u_0}} \frac{E_T}{E_0} \, . \tag{1.89}$$

The perturbation $\mathbf{u_0}$ which causes the largest amount of growth in a flow for a given set of parameters is often referred to as the optimal disturbance. The linearised Navier-Stokes equation is of the form:

$$\frac{D\mathbf{u}'}{Dt} = \mathscr{L}\mathbf{u}' \, , \tag{1.90}$$

where $\mathbf{u}'$ is the base flow perturbation and $\mathscr{L}$ a linear operator. The flow is normal if the adjoint of operator, $\mathscr{L}^*$, commutes with $\mathscr{L}$, i.e. $\mathscr{L}\,\mathscr{L}^* = \mathscr{L}^*\,\mathscr{L}$. Otherwise, such as in the case of the pipe flow, the flow is non-normal. Interactions between the disturbance and the underlying flow can then lead to large distortions of the base flow due to the non-normality of the problem. Indeed, if the problem is normal, then the combination between two or more decaying modes necessarily decays, whereas when the problem is non normal, the superposition of decaying mode can produce shot-term growth. This optimal perturbation was calculated for pipe flows (Bergström, 1992, 1993; Zikanov, 1996), as well as by Reshotko (2001) in the case of spatial growth. It was found that the linear transient growth is primarily driven by streamwise independent rolls which generates streaks (an illustration is given in Figure 1.4). Bergström (1992) studied the optimal growth and the time of its peak, finding that the time at which the peak in energy is reached increase linearly with the Reynolds number of the flow while the optimal linear transient growth scales with Re^2 for all modes. While the value depends on the Reynolds number, the optimal growth is roughly two orders of magnitude larger than the initial perturbation, for example, the optimal energy growth is, for a Reynolds number $Re = 1000$, is $G_{max} = 72.4$ and occurs at a time $T_{max} = 48.8$.

A linear transient growth analysis is limited in scope, the perturbation experiencing the most growth is not necessarily the most susceptible to trigger turbulence as it only takes into account the growth caused by linear effects. Even for very small perturbations for which the nonlinear terms can initially be safely neglected, one may run into difficulty as the disturbance grows, leading to nonlinearity having a significant impact. The natural next step is to retain the nonlinear term of the Navier-Stokes equation.

1.8.3 Mechanisms leading to the formation and sustenance of turbulence

The perturbation the most capable of causing transition to turbulence is not necessarily the one found by a linear analysis. Perturbations that are the most likely to trigger transition have been studied over the last few decades. One example of such perturbations are Tollmien-Schlichting (T-S) waves, which are two-dimensional streamwise waves arising in the viscous boundary layer (Baines et al., 1996; Wu et al., 1996). Baines et al. (1996) focused on temporal stability, considering two parts of the disturbance: an inviscid mode propagating on the vorticity gradient of the velocity profile with the free-slip boundary condition and a damped spatial viscous mode in an infinite uniform shear with no slip condition inside the boundary. Baines found that the excitation of the least stable viscous mode produces a positive feedback in the inviscid mode propagating on the vorticity gradient causing wave growth which is the first step towards instability. Wu et al. (1996) performed a weakly nonlinear study of the T-S waves using high Reynolds number asymptotic methods. Their model describe the evolution of spanwise T-S wavetrains in the boundary layer for the nonlinear case. They found that the nonlinear effects arose mostly from the critical and diffusion layers. As spanwise modulated

waves can also lead to a singularity, they notably highlighted the possibility of the existence of a velocity jump, especially for three-dimensional perturbations. In the case of perturbations having an energy around one percent of the mean flow, Klebanoff et al. (1962) described the pattern as "peak and valley regions", and observed that spikes occurred in peak regions before breakdown. In this case, the transition is characterised by a disturbance frequency approximately five time the frequency of the T-S wave and with aligned lambda-vortices (vortices with two elongated legs of oppositely signed streamwise vorticity and a tip of spanwise vorticity). This is referred as a K-type secondary instability or fundamental transition. For a weaker disturbance, the three-dimensional waves have a smaller frequency, which is around two times the frequency of T-S waves, and are said to be subharmonic (Herbert, 1988). K-type secondary instabilities have an higher growth rate than the K-type waves so are, theoretically, more likely to occur. At later stages, the structures are mostly similar than K-type instabilities, although they are more staggered in this case. They are in general referred to as H-type secondary instabilities or subharmonic transitions. Craik (1971) highlighted the existence of a case where only the spanwise wavelength changes. A pair of oblique waves and a two-dimensional wave of twice the frequency of the two oblique waves form a resonant triad which extract energy from the shear flow. This is defined as C-type transition or subharmonic-resonance mechanism. Schmid and Henningson (2012) studied another way the transition can occur which they call oblique transition. Oblique transition is described in Berlin et al. (1994) by three stages. First, nonlinear generation of streamwise vortices by a pair of oblique waves, then the streaks go through a transient growth process and finally breakdown of the flow if the amplitude of the streaks exceed a given threshold. All these different possibilities for transition have common points, as they follow a similar process of exponential growth instabilities. The bypass transition is the specific process where turbulence is generated directly from the primary growth (the secondary transition is "bypassed"). In he case of bypass-transition, the transient growth is mostly caused by lift-up effects. These lift-up effects, first noticed by Landahl (1975), are caused by the effect of the wall normal velocity on fluid particles in shear flows (or, mathematically, from interactions between non-orthogonal eigenmodes). The fluid particles are displaced in the cross-stream direction and induce a perturbation in the streamwise velocity. Brandt (2014) studied more thoroughly the lift-up effect. He found that the effect was resilient to external noise and is favoured over exponential instabilities for moderate to high noise level. The lift-up effect affects mainly the streamwise vortices, generating large amplitude streaks. The transition to turbulence has been found by Kreiss et al. (1994) to be the result of a secondary instability of these streaks. The question naturally following is how turbulence is sustained. Waleffe (1995) presented a mathematical argument for a self-sustaining process using the following simplified model in place of the Navier-Stokes equations. The self-sustaining process consists of three steps:

- Streamwise rolls redistribute the mean momentum into streaks (spanwise modulation of the streamwise velocity).
- The spanwise varying flow breaks down due to wavelike instabilities in the spanwise direction.

- The nonlinear development of the instability feeds back energy into the streamwise rolls, sustaining them.

Waleffe (1997) extended the results to wall-bounded flows with a lower order model where the Navier-Stokes equations are projected on a suitable set of orthogonal modes.

1.8.4 Localised turbulence, puffs and slugs

There is, between laminar and space-filling turbulent states, an intermediate window where there is spatial coexistence of the laminar and turbulent phases, corresponding to the transitional state observed in Reynolds (1883). It follows that the first step of the transition to turbulence is the creation of localised turbulent patches. This coexistence occurs in two distinct configurations, discussed in Wygnanski and Champagne (1973) and numerically studied in (Reuter and Rempfer, 2004; Shan et al., 1999). For lower Reynolds numbers, from $Re = 1600$ to around $Re = 2000$, the patches are called "turbulent puffs". They are localised pockets of turbulence between ten and twenty diameters long with lower turbulent intensity than fully turbulent flow. Puffs have several characteristics described in Wygnanski et al. (1975). Their length is constant for a given Reynolds number. Turbulence intensity is stronger towards the centre of the pipe than close to the wall. Lengthwise, it increases towards the rear of the puff with a peak at the downstream front. Transition to turbulence occurs gradually at the upstream front, with no clear distinction between puff and laminar flow, while the downstream front is characterised by a sudden relaminarisation. Turbulence is created upstream by drawing energy from the laminar flow, on the other hand, the downstream front has a flat profile, typical of turbulent flows which has a stabilising effect. Puffs propagate down the pipe at approximately the mean velocity of the laminar flow with a slightly faster upstream front and a slow diffusive downstream front (Nishi et al., 2008). In both cases, the difference in velocity increases with the Reynolds number so puffs length growth faster as the Reynolds number increases. Puffs can also split, as they grow in size until relaminarisation occurs in the middle causing the structure to break into two puffs (Shimizu et al., 2014; Wygnanski et al., 1975); puffs can also decay spontaneously (Faisst and Eckhardt, 2004). For Reynolds numbers above 2500 (the exact value depends on various parameters such as initial conditions), another type of structure, called ‘slugs’ is formed. The interior of these slugs is very similar in shape and in intensity to fully turbulent flows. Contrary to puffs, slugs fill the entire cross-section, and both their upstream and downstream fronts are sharply defined. Turbulence is formed at both fronts and the turbulence intensity is constant except at both its extremities where it peaks. The front edge travels significantly faster than both the average flow and the back edge, so the slug expands as it propagates. Therefore, the presence of slugs leads to the development of a fully turbulent flow. Nishi et al. (2008) studied more cases, and showed that the distinction between puffs and slugs is not clear cut, puffs at higher Reynolds numbers have a sharper front edge and can sustain a zone of turbulence.

1.8.5 Statistical nature of the flow

The critical Reynolds number Re_c is often characterised as the Reynolds number defined such that for any Reynolds number $Re \geqslant Re_c$ the created turbulence holds forever. Therefore studies have to be done with very long pipes over large periods of time in order to determine the critical Reynolds number, for both experimental (Darbyshire and Mullin, 1995; Peixinho and Mullin, 2006) and numerical studies (Faisst and Eckhardt, 2004; Hof et al., 2006). Faisst and Eckhardt (2004) were able to observe decays up to $Re = 2250$, Peixinho and Mullin (2006) found similar results, albeit with a lower Reynolds of 1750. Hof et al. (2006) conducted an experimental study using a 7500 diameter pipe but did not find such a cut-off value. The justification for the absence of a critical Reynolds is that decay times become too large, as $Re > 2300$, to be able to realistically observe turbulence decay through either numerical simulation or experimental means. It is now commonly accepted that there is no such critical Reynolds for pipe flows and that turbulence always decays over a sufficient long period of time, albeit it is impossible to formally verify this assumption.

Even if the turbulence eventually decays, one can study its lifetime and how this lifetime depends on factors such as the Reynolds number and the perturbation amplitude. Darbyshire and Mullin (1995) studied the state whether a perturbation created at the pipe onset had decayed or not 120 diameters after its creation, as a function of its initial amplitude and the Reynolds number of the flow. They found that while increasing Re increases the likelihood of having the perturbation persist, as one would expect, the relationship between Re and the probability of turbulence is non-monotonic. Eckhardt et al. (2007) wrote a review about transition to turbulence from the statistical point of view. He studied the lifetime of a perturbation in function of its amplitude and Re, obtaining a wider range and results. The result is highly non-monotonic, with peaks and valleys; small changes in parameters resulting in large difference in either direction.

Since the lifetime of turbulent puffs depends dramatically on small variations of the initial conditions, the study of turbulence's lifetime is highly challenging. A way to bypass these issues is to study the flow as a dynamical system. The flow is considered in its state space, the space of all velocity fields satisfying the problem conditions (corresponding to the equations describing the flow behaviour plus the boundaries conditions). The state space contains both laminar and turbulent profiles, and coherent structures observed during transition such as vortices, T-S or travelling waves are present within the space state at different points. In the region dominated by the laminar flow, the parabolic flow is a fixed point attractor. All points close (in the state space) to the attractor evolve towards it, forming a basin of attraction of the laminar flow. In the region of the space state dominated by the turbulent flow there are similar but not identical attractors, not all neighbouring points are attracted to turbulence dynamics since there is a probability of decay. Those attractors are called strange saddles or chaotic saddles; they are not persistent, contrary to fixed points attractors.

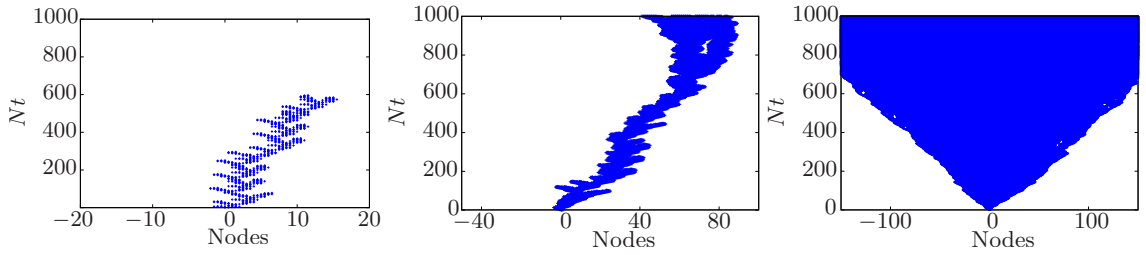

(a) $p < p_c$ (b) $p \simeq p_c$ (c) $p > p_c$

Figure 1.5: Examples of directed percolation in the case of a subcritical state (left), critical state (centre) and supercritical state (right).

An important feature of the state space is the boundary, often called edge of chaos, between the laminar and turbulent regions (Schneider et al., 2007). In particular, one has to consider the mechanisms and conditions for which the edge can be crossed, corresponding to a transition from laminar to turbulent state, or vice-versa. One way to find the edge is nonlinear transient growth, the concept was introduced in Pringle and Kerswell (2010), and extended in Pringle et al. (2012). The first paper analysed the difference between linear and nonlinear transient growth in a pipe; they found a significantly higher maximum energy gain in the nonlinear case, and that the form of the optimal perturbations in linear and nonlinear cases is distinctly different. The methods also allows, by way of very small variations of the perturbation amplitude, to study the edge between laminar and turbulent flow states. Turbulence can spontaneously decay, implying the existence of a decaying trajectory going from the turbulent saddle to the laminar basin of attraction, thus going through the edge. Chantry and Schneider (2014) postulate that the edge does separate laminar and turbulent space globally in state space, but is rather wrapped around the turbulent state and part of the chaotic saddle, therefore leaving a path for trajectory to go from turbulent to laminar state without crossing the edge. Chantry and Schneider (2014) worked with a numerical simulation of a Couette flow, but it is quite possible that the result can be generalised to other shear flows, including pipe flows.

Since the behaviour of the perturbation close to transition is chaotic, it is more pertinent to work with the statistics of the lifetime. Numerical studies (Eckhardt et al., 2007; Faisst and Eckhardt, 2004) found that for a large enough data sample the process is memoryless, and the rate of decay is independent of time. One can, therefore, express the probability of a puff to persist until time t as $P(t) \propto \exp(-t/\tau)$. Combining dynamical systems theory with the statistical nature of the transition in shear flows leads to describing the life time of turbulence using percolation theory. A subset of percolation theory, direct percolation, can model the behaviour of liquid in a network for a given vertice (or site) where the "value" is present. Each neighbouring site has a probability p to allow the value diffusion to the given site. The key parameter is the critical probability p_c:

- $p < p_c$: subcritical state, the probability of any point to contain the value decreases exponentially towards zero with the increase of the network size (Figure 1.5a).

- $p = p_c$: critical value, expresses the phase transition between subcritical and supercritical regimes (Figure 1.5b).

- $p > p_c$: supercritical state, the probability of any point to contain the value increase exponentially toward zero with the increase of the network size (Figure 1.5c).

The percolation theory for transitions in pipe flows is applied in Barkley (2011), Sipos and Goldenfeld (2011) and Avila et al. (2011). Each node of the network corresponds to a region of the size of the viscous length scale. If the turbulent intensity in a node is above a given threshold it is considered turbulent, otherwise it is laminar. The probability p is linked to Re so one can study the statistical behaviour of the flow depending on its Reynolds number, in particular, the time scale of the puffs. One can determine the critical Reynolds number by comparing the time scales of puffs' decay and split. If the former is larger, then turbulence is more likely to spread in the flow. Avila et al. (2011) found the critical Reynolds number for which time scales of puffs' split and decay are equal, at $Re = 2040$. The study of transition to turbulence using percolation theory also has been applied to other shear flows, such as Couette flows (Lemoult et al., 2016) and plane Poiseuille flows (Sano and Tamai, 2016).

While percolation theory gives a way to characterise transition to turbulence in shear flows, it does not reveal any of the mechanisms behind the creation or dissipation of turbulence. Puff dynamics occur over large distances and perturbations, and in the transitional regime puffs decay after extended periods of time (Hof et al., 2006). So, when conducting an experiment or running a numerical simulation, a long pipe and a large number of particles are necessary to capture the dynamics of the transition to turbulence of particulate flows. Furthermore, the statistical and chaotic nature of the problem as well as the large parameter space, the particle density, their size, number and spatial distribution added to the usual parameters for single phase flow, require a substantial number of runs in order to producer general results. These factors make the study of transition to turbulence for particulate flows a particularly challenging problem.

1.9 Effect of the solid phase in the transition to turbulence for shear flows

1.9.1 Effect of the particles on the stability

While turbulence transition has been less extensively studied for particulate flows than single phase flows, a number of aspects of particulate flows have been investigated. The majority of the literature focuses on the trajectory of particles; their clustering and deposition in laminar or turbulent flows. In comparison little interest has been shown in the transition between the two states.

Particulate Hagen-Poiseuille flows have been studied experimentally, notably in Matas et al. (2003), using neutrally buoyant particles. It has been found that the effect of particles on the transition to turbulence varies depending on the particles' size and volume concentration. The transition to turbulence is delayed for small particles, when $r_0/a \geqslant 65$. For these values of r_0/a the Reynolds number for which the transition to turbulence occurs increases monotonically with the particle volume concentration. For high particle volume concentrations ($\phi \geqslant 20\%$), the critical Reynolds number, Re_c, does not depend on the particle size. For bigger particles ($r_0/a \leqslant 65$), the value of Re_c decreases. For small particle volume concentrations, Re_c decreases rapidly with the concentration. However, past a threshold of $\phi \simeq 5-10\%$, the transition is delayed as the concentration increases. They also state the hypothesis that the particles alter the threshold of the subcritical transition through coupling of the base flow with the velocity perturbation rather than through changes in the base flow itself. The main difficulty encountered in the experiment is the lack a of clear definition of when exactly the flow is considered turbulent in the case of particulate flows. Furthermore, the pressure measurement method used in this experiment to determine the flow rate is not reliable for high particle concentrations. To circumvent the problem, Matas et al. (2003) measured the pressure drop between the two ends of the pipe The pressure drop is much higher when the flow is turbulent due to the turbulent puffs, allowing them to make a clear distinction between laminar and turbulent states.

Numerically, very little has been done about transition to turbulence for pipe flows and the work is very specific. Yu et al. (2013) studied very large buoyant particles. Yu found that for low concentrations, the transition is facilitated by the presence of particles whereas it is delayed for high concentrations; their results are in accordance with Matas et al. (2003). They also studied the evolution of the position of particles with time. In order to define when turbulence was occurring they considered the size of the flow eddies compared to the size of the particles. More precisely, they looked at the normalised energy of the streamwise velocity fluctuation directly linked to the size of the eddies. The minimum normalised energy for which the flow is considered turbulent is between 0.013 and 0.02.

Several other numerical studies have been done for the plane Poiseuille flow. The results cannot be directly applied to pipe flows, but since both are shear flows, one can expect similarities in their properties. A linear stability analysis is done by Klinkenberg et al. (2011) and Klinkenberg et al. (2013). In their model, they consider very small particles and the hypothesis that continuity is not broken by their presence. A modal study (exponential growth) and a non-modal one (transient growth) are performed in the first paper. In the modal case, they observe a stabilising effect for intermediate particle size, whereas very large particles are decorrelated from the flow and have no effects. On the other hand very small particles behave like tracers, only modifying the critical Reynolds number through a change in the average density of the flow. The transient growth itself is still dominated by the lift-up mechanism. The particles delay the rate of the disturbance growth but the energy gain is increased by a factor $(1+f)^2$, f being the particle mass concentration. Klinkenberg et al. (2011)

found that the particles have a very different effect on exponential and transient growth suggesting that this is due to the different time scales associated with each phenomenon. Klinkenberg et al. (2013) uses the same model for the particles, but now includes two-way coupling. The fluid flow equations are solved with an Eulerian mesh while the particles evolution is determined through Lagrangian tracking in order to make a fully nonlinear analysis of the transition. Two classic cases are studied, oblique waves and streamwise independent counter-rotating vortices associated to a three-dimensional mode; the main interest being the study of the influence of particles on later stages of the transition not covered by the previous modal and non-modal studies. For high concentrations of particles, there is an increase of the energy threshold necessary to trigger turbulence in both cases, the effect is stronger for oblique waves. It is argued that particles hinder the generation of streamwise vortices through nonlinear interaction with the oblique modes, thus stabilising the flow. In the second case the streak evolution is unaffected but the three-dimensional modes are weakened by the presence of particles, delaying the transition.

Particles migration has been shown to have a significant effect on the transition to turbulence for shear flows. Boronin and Osiptsov (2008) and Boronin and Osiptsov (2016) studied the stability of solid-gas boundary layer flows with a nonhomogeneous distribution. Three particle distributions are considered in Boronin and Osiptsov (2008); a uniform distribution as well as both exponential decay and increase as a function of the distance with the boundary layer. As for the forces acting on the particle, their model take into account the effect of Stokes and Saffman lift. In the case where only the Stokes force is taken into account, for all three distributions the addition of particles increased the critical Re of the flow; this stabilising effect is significantly more pronounced for particle distribution concentrated near the boundary. The critical Reynolds number, Re_c is around 350 for pure fluid, 900 for a constant particle distribution and almost 2500 for a particle distribution increasing towards the wall. When the Saffman lift effect is taken into account a singularity appears in the critical values for certain values of the governing parameters.

Boronin and Osiptsov (2016) study the effect of particles on nonmodal instability and transient growth for particulate plane Poiseuille flows. They used a nonuniform particle distribution with the particle concentrated in two Gaussian symmetric layers shown in Figure 1.1. The largest growth is attained when the particles are concentrated halfway between the wall and the centre. There is also general increase in the transient growth as the particles get more localised. The addition of particles induces, in the most extreme case an increase of the transient growth of almost three orders of magnitude larger compared to the single phase flow.

1.9.2 Particles distribution across the pipe

As mentioned in Section 1.9.1, particles migration is a key element of the stability of bounded shear flows. The study of how the particles are distributed in Pipe flows is closely related to the problem of particulate flow stability. The distribution of particles in the pipe is an important facet of the flow dynamics, including the flow stability, and has been a topic of interest for decades. The distribution of particles in a pipe flow has been first investigated experimentally in Segre and Silberberg (1962). The experiment, concentrated on the lower range of Reynolds numbers, ranging from $Re = 3.7$ to $Re = 694$. Segre and Silberberg (1962) found that the particles converged towards a single radius, also called the Segré-Silberberg radius at $r/r_0 = 0.6$, with r_0 being the pipe radius. Immigration of particles had been observed in previous experiments, Segre gives as example the study of blood flow in Poiseuille (1836) and Taylor (1955). Particles are affected simultaneously by radial forces in opposites directions due to the the Magnus effect, directed towards the centre of the pipe (Rubinow and Keller, 1961), and the Saffman lift directed towards the wall (Saffman, 1965). There is an equilibrium position where the two forces balance each other. Segre derived a theoretical argument that this position's radius is around 0.6. The term *tubular pinch effect* has been coined to express the convergence of the particles towards this equilibrium position. This position does not depend on the particle distribution at the inlet, theoretically all the particles position themselves at the equilibrium radius after a long enough time. Jeffrey and Pearson (1965) studied the repartition of particles in a pipe for laminar flows with a Reynolds number ranging from $Re = 67$ to $Re = 2400$, and a particle volume fraction under one percent. They found that neutrally buoyant particles migrate towards $r = 0.67$. For heavier particles, the radial velocities of particles are higher and the particles radial migration occurs in a smaller time scale.

A more recent and comprehensive study on the topic has been done by Matas et al. (2004b). The position of the particles is measured 310 diameters downstream where the flow can be assumed to be fully established. Particles are randomly distributed at the entrance. Particles are of a relative size r_0/a ranging from 8 to 42, with the following intermediate values, $r_0/a = 9, 10.5, 15, 17$ (where r_0 is the pipe radius and a the particles radius). The particle volume fraction is small enough for the dilute assumptions to be valid, so that particle-particle interaction are of negligible importance. Matas found that the radial position at which the particles migrate to depends on Re. Particles migrate closer to the wall as the Reynolds number increases. Moreover, as the Reynolds increases a fraction of the particles start to settle to a second radial position as well, closer to the centre of the pipe around $r = 0.5$. The value of Re at which it appears is dependent on the particle relative size, the threshold is $Re = 600$ for $r_0/a = 9$ to $r_0/a = 17$ and $Re = 1200$ for $r_0/a = 42$.

The peak closer to the wall is very sharp while the other one is more diluted with a non negligible particle concentration from 0.3 to 0.7. As the Reynolds number continues to increase, particles migrate to the inner annulus until only the peak closer to the wall subsists for $Re = 1650$. Finally,

for $Re = 2400$, the particles are almost evenly distributed, with a less pronounced maximum at $r = 0.4 - 0.5$. The length necessary for radial particles migration depends on the particle size. For the largest particle considered ($r_0/a = 8$), the migration only appeared to be partial at the measurement point.

Small density differences between particles and fluid can affect the distribution through particle sedimentation. Radial inertial force dominates buoyancy for higher Re, the settling length for buoyancy force is also longer than settling length one for radial inertial effect. Therefore if Re is sufficiently high, transient phenomena still occur even for non-buoyant particles.

Asmolov (1999) performed a numerical simulation using the asymptotic theory to find the lift force applied on a spherical particle. The simulation also takes into account the effect of the Stokes drag force and the buoyancy. Asmolov's code has been used in Matas et al. (2004b) to establish a comparison with their data. Simulations and experiments agree on the radial position where the particles are concentrated. However, more particle are on the "equilibrium" radius in the simulation, this is especially true in the case of large pipe length, where nearly all particles are concentrated at the same radius. A more recent numerical study has been done in Shao et al. (2008), using a slightly modified version of the fictitious domain method with an explicit scheme, considering two particle sizes, $a/r_0 = 0.10$ and $a/r_0 = 0.15$, as well as two pipe sizes: $L = 2r_0$ and $L = 4r_0$ with r_0 the pipe radius. For one particle, they find that for higher Reynolds number, when $Re > 10^3$, the particles migrate towards a radius $r \simeq 0.5$; in the same region as observed in Matas et al. (2004b) experiment.

Axial particle distribution has been studied in Matas et al. (2004a), in an experimental study using the same set-up as Matas et al. (2004b). They observed, during measurements, the appearance of trains consisting of up to 40 particles in the flow direction. They are located at the Segré-Silberberg radius and visible for $Re > 100$. The proportion of the particles in trains depends on the Reynolds number. It increases with the Reynolds number at first until a peak is reached for Re varying from 500 to 1000, depending on the particle-pipe length ratio r_0/a. Past this Reynolds number the proportion of particles in trains decays. This decay is due to the change of regime in the particles distribution from the outer Segré-Silberberg radius to the inner radius occurring around similar value of Re. Matas et al. (2004a) explained the phenomenon of train formation by the dilute suspensions used in the experiment, with a particle volume fraction $\phi \leqslant 0.24\%$. Coupled with more evenly distributed particles in the radial distribution for higher values of Re, particles are in this case too far apart to form trains. The authors also argued that the distance between particles in trains depends on the particle Reynolds number $Re_p = Re(a/r_0)^2$. Data show a mostly linear decrease with Re_p. The phenomenon is hypothesised to be due to flow patterns around a sphere changing around $Re_p = 1$ (Matas et al., 2004a; Mikulencak and Morris, 2004). When $Re_p \gg 1$ the influence of the particle on the flow far away from the body does not depend upon the motion on the surface of the particle. It also implies that for stationary flows in these conditions, flows patterns behind fixed and free bodies are identical.

1.9.3 Particles' impact on turbulent flows

For turbulent flows, particles are distributed non-homogeneously (Eaton and Fessler, 1994). While very small particles follow the motion of the fluid and are evenly distributed while larger particles tend to cluster, as for particle density effects, heavier particles accumulate in regions where the strain rate is dominant while lighter particles accumulate in regions where the viscosity is stronger.

A plane Poiseuille flow experiment by Kussin and Sommerfeld (2002) found that while the average turbulent velocity profile of the fluid does not significantly change with the addition of particles, the particle average velocity profile is significantly different from the parabolic fluid profile, being almost flat. As the particle concentration increased, the velocity fluctuations decreased due to particle-particle interactions using an increasing part of the flow total energy. Experimental work by Gore and Crowe (1991) showed that particles had a strong effect on turbulence intensity in pipe flows. The direction of the effect depends on the particle size ratio; small particles dampen the turbulence while particles with a ratio between particle and turbulent length scale larger than one increase it. The turbulence intensity can be more than doubled in some cases. The effect also depends on the particle location in the pipe; it is more pronounced close to the centre of the pipe. Turbulence modulation has also been found in jet and is impacted by particle size in a similar fashion. However, the effect size is smaller with an increase below 50% and is independent of the radial location. Boivin et al. (1998) studied this phenomenon with a two-way coupled point particle method, they found a similar result to Gore and Crowe (1991); an attenuation of turbulence by the addition of particles, although the effect was smaller. Underlying mechanisms for the turbulence modulation are given in Balachandar and Eaton (2010) and Gore and Crowe (1991). Turbulence dissipation is due to the increased drag caused as small particles follow larger eddies and sap part of its energy through the drag force, as well as a change in effective viscosity and enhanced inertia of the flow. Turbulence kinetic energy increase is caused by the creation of turbulent motion in the wake of particles and buoyancy driven instabilities due to non-homogeneous particle distributions.

1.10 Experimental techniques for particulate and transitional flows

The first experimental study of transition to turbulence in pipe flow was done by Reynolds (1883) and relied on dye visualisation of the phenomenon. Experimental techniques have come a long way since then. The main challenge in experimental works is measuring the flow pressure and velocity. Various methods have been developed for this purpose. A historically popular method is to measure the fluid velocity using an hot-wire anemometer, an electrically heated wire probe placed inside the flow, where the wire is cooled by the flow proportionally to the flow velocity. By measuring the wire resistance which depends on its temperature, one then can obtain the flow velocity. Pressure

based flow-meters measure the differential pressure difference between two points and derive the flow velocity through Bernoulli equation. Inertial flow meters rely on the Coriolis force, within which a vibrating tube is placed into the flow, its vibration frequency is proportional to the mass flux. All these methods use intrusive measurement tools, and are only of limited utility for particulate flows since they are vulnerable to collisions for larger particles. Moreover, they do not allow for the measurement of particle velocities.

Laser-based flow measurement techniques, being non-obtrusive methods, are more suited to particulate flows. One such tool is the laser-Doppler anemometry (LDA). Tracer particles are introduced in the flow. Their velocity is assumed to be equal to the surrounding fluid and their size sufficiently small, such that the particles influence on the fluid can safely be neglected (Melling, 1997). The flow is illuminated by two lasers, and the light scattered by the particles is detected by a photodetector. The interference between the two lasers yields a signal measured by the photodetector which is directly proportional to the velocity of the tracer particle, allowing to determine the tracer particles velocity. The data from the tracers particles can be used to obtain the velocity profile of the fluid. The signal depends on the size of the particle considered; therefore, with a suitable calibration the velocity of larger particles can be measured, making LDA methods well-suited to particulate flows. Stock et al. (1975) used two processors to process the photodetector data, the first had a low gain and could detect objects with high signal amplitude corresponding to the particles, while the second with a high gain, detected the tracers with their low signal amplitude.

A similar measurement method, particle image velocimetry (PIV), is nowadays the most commonly used method for particle measurement. Similarly to LDA, the flow is seeded with tracer particles and the flow is illuminated by a laser. However, in PIV methods, a high speed camera is used to capture images of the flow; a particle velocity can be calculated with the distance travelled between two subsequent images. The data can also be processed to obtain various particles characteristics such as vorticity or path-lines. In addition to 2D-PIV, there are several methods that have been developed for three-dimensional measurements field. Lawson and Wu (1997) used stereoscopic techniques; Hassan et al. (1992) used cross-correlation methods and Okamoto et al. (1995) used spring model methods. Hassan (1998) used a PIV set-up to study two-phase flows with fluid and air bubbles. The tracking of larger particles can be achieved with the same methods used for the tracer particles, as larger particles scatter more they are easier to track with a camera. However, laser based methods can only be used for lower particles concentrations. Matas et al. (2003) used pressure drop measurement to bypass the issue and observed dense suspensions using pressure drop measurements at both extremities of the pipe. The pressure gradient in turbulent flows cause stronger pressure drops than laminar flows. While this method allows to characterise the flow transition, it gives no information on the fluid and particles velocities.

Due to the chaotic nature of transition in pipe flows and the long timescales involved (Eckhardt et al., 2007); one need a pipe whose length is sufficiently long (at least of the order of a hundred

diameters) in order to capture the transitional dynamics of the flow, which represents a challenging engineering problem. For example, Darbyshire and Mullin (1995) used a pipe of 190 diameters for their experiment, Peixinho and Mullin (2006) studied puff decay with a 785 diameters pipe. Faisst and Eckhardt (2004) and Hof et al. (2006) considered length over a thousand diameters in their numerical simulations.

Because pipe flows are linearly stable, they are highly sensitive to the nature of the perturbation. This is especially true for larger values of the Reynolds number. Therefore, experiments need to both control the amplitude and the form of the perturbation to study its effect on the flow transition and avoid other sources of perturbation that can disturb the flow. Often the disturbance is created directly injecting an impulsive jet to the flow (Darbyshire and Mullin, 1995; Hof et al., 2003; Peixinho and Mullin, 2007), while this allows to control the amplitude of the perturbation this is not the case for its shape; Nishi et al. (2008) used an iris diaphragm to provoke a small flow blockage, triggering puff generation. Wygnanski et al. (1975) connected the pipe to a small outside reservoir, the vibration of a speaker placed against the reservoir provokes the creation of a perturbation inside the pipe.

1.11 Numerical methods

The Navier-Stokes equations describing the fluid do not have a single analytical solution in most cases, their evolution needs to be computed incrementally from a chosen initial state. In the case of turbulent flows, several numerical methods can be used to simulate the flow. The most commonly used models to describe turbulent flows are $k-\varepsilon$ and $k-\omega$ models. They both describe turbulence through a set of two partial differential equations. The variables are, in the $k-\varepsilon$ model, the turbulence kinetic energy k and the rate of dissipation of turbulence energy ε while the $k-\omega$ model uses specific rate of dissipation of the turbulent energy, ω, with the turbulence kinetic energy k. The $k-\varepsilon$ and $k-\omega$ models are only valid in the framework of fully turbulent flows, they are not suited to our problem as we focus on the transition between laminar and turbulent states. Another commonly used method is the Direct Numerical Simulation (DNS), where the entire scale range is simulated, and to a lesser extent; Large Eddy Simulation (LES) where only the larger length scales are fully described and the smaller scales are approximated through a sub-grid stress tensor. While a DNS is more numerically costly, the general increase in computational resources have facilitated its use. Furthermore, in the case of discretely modelled particles with more than a few dozens particles, the cost of simulating the solid phase is significantly higher than the cost of simulating the fluid phase. Therefore, the choice between LES and DNS has little influence on the total running cost of a particulate flow numerical simulation.

1.11.1 Particle modelling

Another critical point of the numerical simulation method is the modelling of the particles themselves. The optimal strategy strongly depends on the theoretical model considered. If the particles are described with a fully Eulerian framework, such as the models described in Section 1.4.2, the particle modelling can be built directly upon the code describing the fluid phase. The solid phase is modelled through a modification of the set of equations used to describe the fluid while the rest of the numerical procedure can be kept identical. Since the particles are described as a continuous medium, the existing mesh and numerical methods used to solve the fluid behaviour can be used. In the case of one-way coupling, since the flow evolution is not dependent on the particles characteristics, one can consider simultaneously several particles parameters set at little additional cost; as done in Février et al. (2005) by simulating the fluid phase first and using it repeatedly while varying particles parameters. The processing power needed to use these numerical methods is of the same order of magnitude as single phase flow simulations with an increase of a factor two as it is an equivalent procedure with a larger number of equations to solve. Another advantage of fully Eulerian simulations is that their cost is independent of the number of particles, whose increase is represented by a change of the parameter representing the local particle concentration. For models using Lagrangian tracking, the addition of particles is more costly, as the simulation of discrete entities is a complex and expensive procedure. The point particle model represents each particle as a point, therefore Lagrangian and Eulerian meshes do not need to directly interact and there are no moving boundaries to consider. Moreover, an equation is needed to describe the trajectory of each particle; and the size of the equation system increases linearly with the number of particles so the number of particles considered is strongly limited by the processing power available. Uhlmann (2005) uses 512 force points per particle, however, only the fluid-particle interactions depend on this number. Because of the solid-body approximation the solution of the particle motion scales with the number of particles. Finally, in their study the majority of the computational cost was due to the simulation of the fluid. Consequently adding more particles only added a marginal cost to the simulation. Similarly for the Physalis method, Prosperetti and Oguz (2001) noted that the computational cost scales less than linearly with the number of particles.

1.11.2 Detection and processing of particle-particle collisions

Four-way coupled numerical simulations need to include a way to detect collisions between particles and compute the resulting changes in velocity. Immersed boundary methods (Glowinski et al., 1999; Uhlmann, 2005), bypass the issue with the addition of a fictitious repulsive force to avoid collisions. Point particle models directly look for and simulate the effect of collisions. To detect collisions in a simulation containing N particles, one can use a brute force method that checks for every possible collision between any two particles. Scaling with N^2, this method is simple to implement but

inefficient. The scaling makes it an unattractive options when large numbers of particles are involved. The efficiency can be improved by checking for collisions of a given particle only with particles in their neighbourhood (Vance et al., 2006; Yamamoto et al., 2001; Zhao et al., 2006). The domain is separated into cells, the particles are then sorted by cell, the collision detection procedure can then be made independently for each cell. The efficiency of this method depends on the particle concentration and the cell size. Mio et al. (2005) found that the optimal cell size should contains, on average, 0.7 to 0.8 particle. This value shows little variation with the particle size. The nearest neighbour method assigns a radius to each particle. Only the particles within this radius are checked for a potential collision. Both the cell and nearest neighbour method scale with N with the right choice of parameters, making them significantly more efficient than the brute force method, at the cost of additional memory needed to store information about particles.

1.11.3 Conversion from Eulerian to Lagrangian and Lagrangian to Eulerian frame of reference

In the case of Eulerian-Lagrangian mixed simulations, the fluid data needs to be interpolated at the particles position and, in turn, the particulate force is interpolated to the Eulerian mesh. In most cases, polynomial interpolation is used to obtain the fluid data in the Lagrangian framework. Boivin et al. (1998) and Vance et al. (2006) used respectively third and fourth order Lagrange polynomials. Ferrante and Elghobashi (2003) used a Hermite cubic interpolation polynomial. The interpolation from the Lagrangian to Eulerian mesh is done either independently for each particle or averaged. Ferrante and Elghobashi (2003) distribute the particle force to the 8 surrounding nodes with a linear projection. Averaging methods are studied in Zhu and Yu (2002) and Zhu et al. (2007), where the local average $\bar{\mathbf{X}}(\mathbf{r},t)$ of a property $\mathbf{X}(\mathbf{r},t)$ to interior cells can be generally written as:

$$\bar{\mathbf{X}}(\mathbf{r},t) = \int_{T_1} \sum_i h_i \mathbf{X}_i(\tau) \mathrm{d}\tau \,, \tag{1.91}$$

where $\mathbf{h}(\mathbf{r},t)$ is a weighting function.

1.12 Selection of the models used in this work

We have, in this Chapter, described some of the most common model used to describe particulate flows as well as the tools used to study the stability of shear flows. A key choice in this work has been the selection of the physical models used and the choice of problem to study. Let us go through the methods chosen, with the explanations and justifications behind these choices.

First, we have to consider the choice of the model used to describe the particulate flow. Our work focuses on the transition to turbulence, and in particular the particles influence on the flow stability. Therefore, the chosen model needs to take into account the effect of the solid phase on the fluid. Some models do so while neglecting the effect of the fluid on the particles, e.g. the models presented in Section 1.3. However, they require restrictions that would strongly limit the validity of any result. Indeed, particles behaviour is nontrivial during transition and one should expect the solid phase to have a significant effect on the fluid. Consequently, the model used needs to be two or four-way coupled, reducing the number of available options. On the other hand, the more computationally demanding models with a more accurate particle description, the fully Lagrangian and immersed boundary methods, do not, in spite of their accuracy, suit the needs of this work. The aim of this work is to investigate the transition to turbulence in a more general way and study different processes as a function of the particles characteristics, requiring a large amount of runs to accumulate data. In the interest of reaching the optimal trade-off between accuracy and cost-efficiency, two models were used in this thesis: a fully Eulerian model, used in Chapter 2 and 3 and a Lagrangian-Eulerian model with a point particle approximation in Chapter 4. These two models rely on fundamentally different assumptions: the fully Eulerian model has a smaller parameters validity range and is less suited to the study of particles behaviour. Moreover, it is valid for small, heavy particles in dilute distributions. In this regime the Stokes drag is the dominant force and the other fluid-particles interaction force can be neglected (more details are given section 2.1). The collisions between particles are also neglected as we assume that the solid concentration is dilute. On the other hand, point particle model is more realistic and versatile at the expense of the computational cost. As the point-particle code aims to be valid for larger particles and higher particle volume fraction, other fluid-particle interactions forces, such as the buoyancy and the added mass force, were added. Furthermore, collisions between particles are also accounted for with a hard-particle collision model. The combination of these two models, which possess different strength and weaknesses, allows for greater flexibility.

The second question is the choice of the tool to study the flow stability. There are many options to approach the topic to transition to turbulence, we chose to begin with a linear stability analysis using the fully Eulerian model. The continuous approximation made for the particle phase in the fully Eulerian model allows to write the equations of motion as a linearised system which can be solved numerically (see Section 2.4). Each run is then very fast, such that we could obtain a significant amount of data-points over several parameters. The linear stability analysis give insight on the asymptotic behaviour of flows. The linear stability analysis is complemented by a linear transient growth study, also using the fully Eulerian method to describe the solid phase. The linear transient growth aims to observe the flow stability at finite times, and in particular if it can lead to new mechanism for instability. The point particle model is still in development. It has only been used to study the behaviour of fully turbulent particulate flows, but it can be used to study transitional flows or the stability of laminar flows to perturbations.

Chapter 2

Linear instability of particulate pipe flow with a Eulerian description

In this chapter the linear stability of particulate pipe flows is studied using a fully Eulerian approach for the description of the solid phase. This model used to describe the solid phase is similar to the one introduced in Klinkenberg et al. (2011) and described in Section 1.4.2. While the fully Eulerian model yields less accurate results than fully described particles, or even point-particles models, it has the advantage of being significantly faster and requiring less computational resources. Moreover, the consideration of independently defined objects is not suitable to the study of linear stability, as the number of equations would quickly grow too large to be solvable through this method.

The limitations of the model used in this work are similar to the ones encountered for a single phase flow linear stability analysis. Nonlinear interaction of the modes are not taken into account and this model can describe neither the turbulent regime nor the nonlinear transient growth. There are additional conditions due to the limitations of the Eulerian model. The model is considered in the dilute limit, so interactions between particles such as collisions and clustering are neglected. Particles are also assumed to be smaller than the characteristic scale of the flow, significantly heavier than the fluid and of spherical shape.

Even when the flow is linearly stable, linear stability analysis still yields information on the particles influence on the long term stability through the value of the perturbation growth rate. Linear stability analysis is done by solving an eigenvalue system. Each computation is fast, of the order of ten seconds using a single core of an average personal computer. This way we were able to obtain a large number of data points and cover a wide range over the flow parameters.

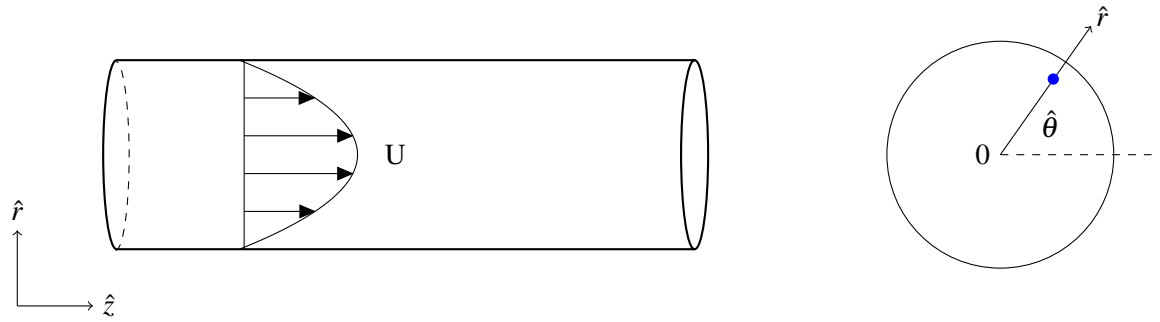

Figure 2.1: Diagram of the geometry in this work. It is a pipe of length L and of radius r_0, and the coordinates used are, in the radial direction $r \in [0,\ 1]$, where r is normalised by r_0; the azimuthal angle $\theta \in [0,\ 2\pi]$ and in the streamwise direction, $z \in [0,\ L]$.

2.1 Range of validity of the model

The fully Eulerian model used in this chapter is valid in the limit of small particles and low particle volume concentrations. Moreover, the only force affecting the particles in this model is the Stokes drag. Other forces often considered, such as the virtual mass force, the buoyancy, the Basset history force, the Magnus and Saffman forces, are neglected. This choice is justified by the difference in scaling with the particle size, a. Indeed, while the Stokes drag force, $F_D \equiv |6\pi a\mu U_0|$, depends linearly on the particle radius, other forces have a quadratic or above dependency with the particle radius. Therefore, the Stokes drag becomes dominant when $a \to 0$ (Boronin and Osiptsov, 2008; Klinkenberg et al., 2011). For the dimensionless problem, the dimensionless relaxation time is defined as: $S = \frac{\tau_p}{\tau_f} = \frac{2}{9}\frac{a^2}{r_0^2}\frac{\rho_p}{\rho_f}$, with τ_p the particle relaxation time and τ_f the fluid viscous time scale. In order for S to remain finite as $a \to 0$, one needs the particle density to scale with the particle radius such that: $\rho_p \propto a^{-2}$. This leads to an additional condition, indeed the buoyancy force can be expressed as:

$$F_B = (\rho_p - \rho_f)\frac{4}{3}\pi a^3 g \,, \tag{2.1}$$

the first term, called F_{B1} from now on, is proportional to $\rho_p a^3$. If $\rho_p \propto a^{-2}$, then this term decays linearly with a, similarly to the Stokes drag. Our model is only valid when the buoyancy is negligible in front of the drag force. In order to determine the condition for which it is true, let us consider the ratio between F_D and F_{B1} is:

$$\frac{F_D}{F_{B1}} = \frac{\frac{4}{3}\pi a^3 \rho_p g}{6\pi a \rho_f \nu U_0} = \frac{2}{9}\frac{\rho_p}{\rho_f}\frac{a^2 g}{\nu U_0} \,. \tag{2.2}$$

Equation (2.2) can be rearranged such that:

$$\frac{F_D}{F_{b1}} = \frac{2}{9}\frac{\rho_p}{\rho_f}\frac{a^2}{r_0^2}\frac{r_0^2 g}{\nu U_0} = \frac{2}{9}\frac{\rho_p}{\rho_f}\frac{a^2}{r_0^2}\frac{r_0^3 g}{\nu^2}\frac{\nu}{r_0 U_0} = S\frac{Ga}{Re} \,, \tag{2.3}$$

where $Ga = \frac{r_0^3 g}{\nu^2}$ is the Galilei number. Assuming a fixed value of S, buoyancy can be neglected when $Ga \ll Re$. There are other concerns to address when considering the averaging process of the equations describing the solid phase behaviour, in particular equations closure. A summary of the framework and assumptions made for averaged models is given in Jackson (2000). Neglecting buoyancy allows us to treat the averaging process of this model as a simplified version of Jackson's approach in the limit of small particles. Lastly, the continuum approach requires the average distance between particles to be as small as possible. This is valid in the limit of dilute particles only. The particles volume ratio V_p/V_f scales as a^3. On the other hand the particle mass fraction scales as: $f \propto N\rho_p a^3 \equiv Na^{-2}a^3 \equiv Na$. It follows that, for a fixed value of f, N increases linearly as a decreases. Therefore, as the particle radius decreases, the volume mass fraction decreases but the number of particles increases. The average distance between particles can be approximated as $< d > \propto 1/n^{1/3}$

with $n = N/V_f$, using $N \propto a$, $< d >$ can be written, since V is constant, as $< d > \propto 1/a^{1/3}$. While the average distance between particles does increase as particles get smaller, the scaling is much slower than the decrease in particle volume fraction as a decrease. Consequently, there exists a regime of particles radius for which both the dilute regime assumption and a low average particle distance are true. The parameter range studied in this chapter is:

- $V_p/V_f < 10^{-2}$, with V_p/V_f corresponding to the particles volume fraction. This condition ensures that the dilute assumptions made to neglect collisions is valid.
- $f \in [0, 0.1]$. As the particles are much heavier than the fluid and $V_p/V_f = f\,\rho_p/\rho_f$, the dilute suspension assumption is valid even in the case $f = 0.1$ when $\rho_p/\rho_f \ll 1$.
- $S \in [10^{-4}, 10^{-1}]$; considering a density ratio between particles and fluid ρ_p/ρ_f to be around 1600 (the ratio between air and sand) as an example, This corresponds to particle diameter/ pipe diameter ratio ranging from approximately $a/r_0 = 5 \times 10^{-4}$ to $a/r_0 = 1.5 \times 10^{-2}$.
- Re are considered up to $Re = 10^6$, the majority of the data lays between $Re = 5 \times 10^2$ and $Re = 10^4$.

The ranges of particle volume ratio and particle size considered in this work fall within the assumptions of dilute suspension with small particles made by the model.

2.2 Governing equations

The fluid phase behaviour is described using the standard Navier-Stokes set of equations to which a Stokes drag force is added to account for the interaction between fluid and solid phases,

$$\frac{\partial \mathbf{u}}{\partial t} = -\frac{\nabla p}{\rho} - (\mathbf{u}\cdot\nabla)\mathbf{u} + \nu\nabla^2\mathbf{u} + \frac{KN}{\rho}(\mathbf{u_p} - \mathbf{u}), \tag{2.4}$$

$$m\frac{\partial \mathbf{u_p}}{\partial t} = -mN(\mathbf{u_p}\cdot\nabla)\mathbf{u_p} + KN(\mathbf{u} - \mathbf{u_p}), \tag{2.5}$$

$$\frac{\partial N}{\partial t} = -\nabla\cdot(N\mathbf{u_p}), \tag{2.6}$$

$$\nabla\cdot\mathbf{u} = 0, \tag{2.7}$$

with $\mathbf{u}$ and $\mathbf{u_p}$ representing the fluid and particles velocities, N is the number of particles per unit volume and p the pressure, ν is the fluid kinematic viscosity, m is a particle mass, K is the Stokes drag ($K = 6\pi a\mu$), with a the particle radius. Equation (2.4) describes the motion for the fluid

velocity is the incompressible Navier-Stokes equation with an additional Stokes term for fluid-particle interaction. Equation (2.5) gives the evolution of the continuous particle velocity using standard momentum conservation without a pressure force and viscous dissipation. Equation (2.6) is the continuity equation for particles, it ensures the conservation of the total number of particles. Equation (2.7) is the standard mass conservation equation for an incompressible fluid. The boundary conditions is for the fluid velocity, no slip at $r = 1$;

$$\mathbf{u}(r = 1) = 0\,. \tag{2.8}$$

For the particles, only the non-penetration condition is kept, particles are allowed to slide against the wall,

$$\mathbf{u_{pr}}(r = 1) = 0\,, \tag{2.9}$$

The non-dimensional parameters for this problem are the Reynolds number, $Re = \frac{ur_0}{\nu}$ with r_0 being the pipe radius and ν the fluid kinematic viscosity. The mass concentration $f = m_p/m_f$, corresponding to the ratio between the particles and fluid mass over the entire pipe. $S = \frac{\nu m}{K r_0^2} = \frac{2}{9}\frac{a^2}{r_0^2}\frac{\rho_p}{\rho_f}$ is the dimensionless relaxation time. The value SRe is equivalent to a Stokes number. A small value of S represents a small particle with a short relaxation time, adapting quickly to the flow. In the lower limit $S \to 0$, the particles behave as passive tracers. A large value of S implies larger particles with longer timescales that are less affected by the flow. In the upper limit, $S \to +\infty$, the particles are decoupled from the flow. In this case they do not have any influence on the flow stability. This non-physical behaviour illustrates a limit of the model, which only applies to particles of small to moderate size. The system of equations (2.4)-(2.7) can be, using the dimensionless parameters previously introduced, non-dimensionalised to yield:

$$\frac{\partial \mathbf{u}}{\partial t} = -\nabla p - (\mathbf{u}\cdot\nabla)\mathbf{u} + \frac{1}{Re}\nabla^2\mathbf{u} + \frac{fN}{SRe}(\mathbf{u_p} - \mathbf{u})\,, \tag{2.10}$$

$$\frac{\partial \mathbf{u_p}}{\partial t} = N(\mathbf{u_p}\cdot\nabla)\mathbf{u_p} + \frac{1}{SRe}(\mathbf{u} - \mathbf{u_p})\,, \tag{2.11}$$

$$\frac{\partial N}{\partial t} = -\nabla\cdot(N\mathbf{u_p})\,, \tag{2.12}$$

$$\nabla\cdot\mathbf{u} = 0\,. \tag{2.13}$$

N is normalised so that $\int NVdV = 1$, for a given position $\mathbf{x}$, $N(\mathbf{x}) > 1$ implies than the local concentration of particles is higher than average, $N(\mathbf{x}) < 1$; the opposite.

2.3 Linearised problem

The stability of the flow is studied through the addition of a small perturbation to the steady solution for each variable. The base state is composed of $\mathbf{U} = (1-r^2)\hat{\mathbf{z}}$, the Hagen-Poiseuille flow, for the fluid velocity. $\mathbf{U_p}$ is the base particle velocity and is assumed to be equal to $\mathbf{U}$. N_0 is the average particles concentration.

$$\mathbf{u} = \mathbf{U} + \mathbf{u}' \ , \ \mathbf{u_p} = \mathbf{U_p} + \mathbf{u_p}' \ , \ p = P + p' \ , \ N = N_0 + N' \ . \tag{2.14}$$

Linearising equations (2.10) - (2.13) around this base state yields:

$$\partial_t \mathbf{u}' = -\nabla p' \ - \mathbf{U}\cdot\nabla\mathbf{u}' \ - \mathbf{u}'\cdot\nabla\mathbf{U} + \frac{1}{Re}\nabla^2\mathbf{u}' + \frac{fN_0}{SRe}\left(\mathbf{u}'_\mathbf{p} - \mathbf{u}'\right) , \tag{2.15}$$

$$\partial_t \mathbf{u_p}' = -\mathbf{u_p}'\cdot\nabla\mathbf{U} - \mathbf{U}\cdot\nabla\mathbf{u_p}' + \frac{1}{SRe}\left(\mathbf{u}' - \mathbf{u}'_\mathbf{p}\right) , \tag{2.16}$$

$$\partial_t N = -N_0\nabla\cdot\mathbf{u}'_\mathbf{p} - \mathbf{u}'_\mathbf{p}\cdot\nabla N_0 - \mathbf{U}\cdot\nabla N' \ , \tag{2.17}$$

$$\nabla\cdot\mathbf{u}' = 0 \ . \tag{2.18}$$

Equations (2.15), (2.16) and (2.18) are independent of N', and Equation (2.17) is decoupled from the other equations of the system. $\mathbf{u}'$ and $\mathbf{u_p}'$ satisfy the same boundary condition as $\mathbf{u}$ and $\mathbf{u_p}$. The set of equations (2.15)-(2.18) is solved numerically with two different methods, a linear stability analysis and a linearised Direct Numerical Simulation (LDNS). From now on the primes are dropped for the sake of simplicity.

2.4 Linear stability analysis

Due to the linearity of the problem the modes are independent. Thus, a linear stability analysis study the behaviour of a single mode at a time. The solutions to the linear set of equations can be written as Fourier expansions with regards to the time:

$$\mathbf{g}(r,\theta,z,t) = \hat{\mathbf{g}}(r,\theta,z)e^{-i\omega t} \ , \tag{2.19}$$

with g being any of the fields of interest. Since our geometry is a pipe, there is by default a 2π-periodicity in the azimuthal direction, a L-periodicity (where L is the pipe length) can also be assumed in the streamwise direction for large values of L. The invariance of the problem along the azimuthal and streamwise directions implies that the perturbation has a wave-like solution in these directions; a Fourier decomposition can be used in the azimuthal and streamwise direction as well as in time. A

field $\mathbf{g}$ can then be written as:

$$\mathbf{g}(r,\theta,z,t) = \sum_{\alpha}\sum_{m} \hat{g}(r) e^{i(\alpha z + m\theta - \omega t)} \,, \tag{2.20}$$

where α and m are the streamwise and azimuthal wavenumbers and are fixed for a given case.

It follows that Equations (2.15)-(2.18), with their associated boundary conditions (2.8) and (2.9), can be written as a generalised eigenvalue problem:

$$i\omega \mathbf{A}\phi = \mathbf{B}\phi \,, \tag{2.21}$$

where ω is the eigenvalue and $\phi = (\hat{u_r}, \hat{u_\theta}, \hat{u_z}, \hat{p}, \hat{u_{pr}}, \hat{u_{p\theta}}, \hat{u_{pz}})^T$ the variables, also called eigenfunctions. The imaginary part of the eigenvalue, $\Im\{\omega\}$ corresponds to the flow asymptotic growth rate. For a given pair of modes (α, m), $\mathbf{A}$ and $\mathbf{B}$ are defined as:

$$diag(\mathbf{A}) = \begin{bmatrix} -1 & -1 & -1 & 0 & -1 & -1 & -1 \end{bmatrix} \,, \tag{2.22}$$

$$\mathbf{B} = \begin{bmatrix} a_1 & -\frac{2im}{r^2} & 0 & -\partial_r & \frac{fN_0}{SRe} & 0 & 0 \\ \frac{2}{Re}\frac{im}{r^2} & a_1 & 0 & -\frac{im}{r} & 0 & \frac{fN_0}{SRe} & 0 \\ -U' & 0 & a_3 & -i\alpha & 0 & 0 & \frac{fN_0}{SRe} \\ \frac{\partial_r}{r} + \frac{1}{r^2} & \frac{im}{r^2} & \frac{i\alpha}{r} & 0 & 0 & 0 & 0 \\ \frac{1}{SRe} & 0 & 0 & 0 & -Ui\alpha - \frac{1}{SRe} & 0 & 0 \\ 0 & \frac{1}{SRe} & 0 & 0 & -iU\alpha - \frac{1}{SRe} & 0 & 0 \\ 0 & 0 & \frac{1}{SRe} & 0 & -U' & 0 & -iU\alpha - \frac{1}{SRe} \end{bmatrix} \,, \tag{2.23}$$

with:

$$a_1 = -iU\alpha + \frac{1}{Re}\left(\partial_r^2 + \frac{1}{r}\partial_r - \frac{m^2+1}{r^2} - \alpha^2\right) - \frac{fN_0}{SRe} \,, \tag{2.24}$$

and

$$a_3 = -iU\alpha + \frac{1}{Re}\left(\partial_r^2 + \frac{1}{r}\partial_r - \frac{m^2}{r^2} - \alpha^2\right) - \frac{fN_0}{SRe} \,. \tag{2.25}$$

In order for the system to be solved numerically the problem needs to be discretised. In the radial direction, the value of the variables is approximated using the Chebyshev polynomials T spanning

from $r = 0$ to 1,

$$\hat{g}(r) = \sum_{n=1}^{M} \bar{g}_n T_n(r) \,, \tag{2.26}$$

where T_n is the n^{th} Chebyshev polynomial. $\hat{g}(r)$ is approximated using M Chebyshev polynomials.

To discretise in the radial direction, M points are taken. These points are placed at the Chebyshev roots that have a higher concentration close to the centre and the wall of the pipe, where accuracy is most needed. The points are defined by:

$$r_l = \cos\left(\frac{2l-1}{2M}\pi\right), \quad l = 1, ..., M \,. \tag{2.27}$$

A and **B** are matrices of size $7M \times 7M$. The boundary conditions are included by replacing the last six rows of the matrices. This does not affect the rest of the problem if the number of Chebyshev polynomials is high enough. The resulting discretised problem is solved in Fortran using the LAPACK library.

2.5 LDNS simulation

A linearised version of a DNS code is implemented with the solid phase modelled using the same fully Eulerian method and the same set of equations, in order to cross-check the results obtained by the linear eigenvalues simulations.

The basis for the LDNS computation is a well established code for the simulation of single phase pipe flow (Willis, 2017). It has been modified to account for the presence of particles, and incorporates Equations (2.15)-(2.18). The code uses a fourth order implicit finite difference scheme, the grid points in the radial direction are defined using Gauss-Lobatto collocation points, and Fourier transforms in the azimuthal and streamwise direction. The variable is represented as $\mathbf{f}(r,t,z) = \sum_{k,m} k(r) a_{km} e^{i(\alpha kz + m_0 m\theta)}$. Temporal discretisation is done through a second-order predictor-corrector scheme. More details on the code are given in Section 3.3. The growth rate of the leading eigenvalue is proportional to the energy decay rate of the flow in the limit of infinite time. Indeed, as the leading eigenvalue is the slowest to decay, the effect of all others eigenvalues become negligible as the time grow large enough. In order to assess whether a given time large enough for the decay rate to converge, we considered two intervals of time, $[t_1,\, t_2]$ and $[t_3,\, t_4]$. The average decay rate over each interval is computed. If the difference between the two decay rates is below a chosen threshold, we consider the run to have converged.

Number of Chebyshev modes	$Re = 10^4$	$Re = 10^6$
70	2.4015×10^{-4}	4.2460×10^{-1}
100	1.1451×10^{-4}	3.2291×10^{-2}
150	4.7985×10^{-5}	4.1129×10^{-5}
200	2.4848×10^{-5}	1.5846×10^{-5}
300	8.4055×10^{-6}	9.4246×10^{-6}

Table 2.1: Normalised difference $\frac{\Im\{\omega\}-\Im\{\omega\}^{M=500}}{\Im\{\omega\}^{M=500}}$ between the growth rate and its converged value (using 500 Chebyshev polynomials) for the single phase flow, $(\alpha, m) = (1, 0)$.

Number of Chebyshev modes	$S = 10^{-4}$	$S = 5 \times 10^{-2}$
100	3.1458×10^{-5}	8.8386×10^{-2}
150	1.3681×10^{-5}	3.7026×10^{-4}
200	5.1509×10^{-6}	1.9357×10^{-4}
300	1.1547×10^{-6}	7.1197×10^{-5}

Table 2.2: Normalised difference $\frac{\Im\{\omega\}-\Im\{\omega\}^{M=500}}{\Im\{\omega\}^{M=500}}$ between the growth rate and its converged value (using 500 Chebyshev polynomials) for the particulate flow with $(\alpha, m) = (1, 0)$ and $Re = 10^4$.

The LDNS is much slower than the eigenvalue solver as it needs to simulate the flow at large times. Therefore, the LDNS was only used to verify the growth rates found with the eigenvalue solver in Section 2.6.2.

2.6 Validation of the numerical simulations

2.6.1 Convergence tests

To validate the code, the leading eigenvalues of the single phase flow, corresponding to $f = 0$, are compared with the results from Meseguer and Trefethen (2003). For the wavenumbers $(\alpha, m) = (1, 0)$, the relative error is below 10^{-9} for 100 Chebyshev polynomials for any $Re < 10^4$. For $(\alpha, m) = (1, 1)$, the relative error is higher, close to 10^{-7} for both $Re = 10^3$ and $Re = 10^4$. For $(\alpha, m) = (1, 1)$, the relative error is of 10^{-9} for $Re = 1000$, and 2.87×10^{-9} for $Re = 10^4$.

Re	α	m	Eigenvalue solver	LDNS	ε
1000	0	1	-1.4682×10^{-2}	-1.4681×10^{-2}	5.5853×10^{-5}
3000	0	1	-4.8940×10^{-3}	-4.8866×10^{-3}	1.5121×10^{-3}
5000	0	1	-2.9364×10^{-3}	-2.9344×10^{-3}	6.9658×10^{-4}
1000	1	0	-7.0864×10^{-2}	-7.0898×10^{-2}	4.7956×10^{-4}
3000	1	0	-4.1276×10^{-2}	-4.1317×10^{-2}	1.0131×10^{-3}
5000	1	0	-3.2043×10^{-2}	-3.2087×10^{-2}	1.3604×10^{-3}
1000	1	1	-9.0443×10^{-2}	-9.0483×10^{-2}	4.3953×10^{-4}
3000	1	1	-5.1973×10^{-2}	-5.2018×10^{-2}	8.7257×10^{-4}
5000	1	1	-4.0200×10^{-2}	-4.0246×10^{-2}	1.1504×10^{-3}

Table 2.3: Single phase flow comparison, $\varepsilon = \frac{|\omega_{lsa}-\omega_{LDNS}|}{\omega_{LDNS}}$, $dt = 10^{-3}$.

The convergence of the results as a function of the number of Chebyshev polynomials has been verified as well. Table 2.1 and Table 2.2 show the relative difference with the fully converged value using 500 polynomials, for the single phase and particulate flows respectively. The convergence for the single phase flow is fairly good with a relative difference of the order of 10^{-4}; even for 70 Chebyshev polynomials in the case $Re = 10^4$, this result holds true in the lower range of Reynolds numbers. Convergence is slower for very high Reynolds numbers, but it is not a large concern as these Reynolds numbers are outside our span of interest.

For the particulate flow, the relative error ε is higher; 10^{-2} for some combinations of parameters; in these cases a higher number of Chebyshev polynomials (150 or 200) were used. ε increases for higher values of S and f, from $\varepsilon = 10^{-6}$ for $S = 10^{-3}$ to $\varepsilon = 10^{-5}$ for $S = 0.1$ and 100 and 150 polynomials. The effect of α on ε is less pronounced, with a relative error difference below 10% with every other parameters fixed. The convergence is also slower for $m = 1$.

2.6.2 Comparison between eigenvalue solver and LDNS computation

Table 2.3 and Table 2.4 show the leading eigenvalue found with linear stability analysis and LDNS simulation, for a single phase and particulate flow respectively. The normalised difference is always below 10^{-3}, and the difference also tends to be lower for lower values of Re and S. For single phase flows, the difference between Meseguer values and our data is smaller in the case of the linear stability analysis than for the LDNS, either because Meseguer and Trefethen (2003) used linear stability analysis as well, or because the LDNS gave a less accurate growth rate.

S	α	m	Eigenvalue solver	DNS	ε
10^{-4}	0	1	-1.4526×10^{-2}	-1.4526×10^{-2}	5.5075×10^{-6}
10^{-3}	0	1	-1.4536×10^{-2}	-1.4523×10^{-2}	8.3513×10^{-4}
10^{-2}	0	1	-1.4513×10^{-2}	-1.4501×10^{-2}	8.7025×10^{-4}
10^{-1}	0	1	-8.4935×10^{-3}	-8.4931×10^{-3}	4.8274×10^{-5}
10^{-4}	1	0	-8.9988×10^{-2}	-9.0029×10^{-2}	4.5108×10^{-4}
10^{-3}	1	0	-8.9981×10^{-2}	-8.9977×10^{-2}	4.7790×10^{-5}
10^{-2}	1	0	-8.9791×10^{-2}	-8.9855×10^{-2}	7.5478×10^{-4}

Table 2.4: Particulate phase flow comparison, $\varepsilon = \frac{|\omega_{lsa}-\omega_{LDNS}|}{\omega_{LDNS}}$, $Re = 1000$, $f = 0.01$, $dt = 10^{-3}$.

2.7 Linear stability analysis of the flow with homogeneous particle distribution

At first, a uniform particle distribution N_0 in the pipe is considered. In this case, $\nabla N_0 = 0$ in Equation (2.17), and the particle concentration fN_0 is constant in Equation (2.15). The least stable eigenvalue ω_p tends towards zero as the Reynolds number increases but remains negative for all Reynolds numbers considered, such that the flow remains linearly stable. This result holds true in all studied cases. It can be concluded that the addition of uniformly distributed particles is not sufficient to introduce linear instability in a pipe flow with the two-fluid model.

2.7.1 Topology

Figure 2.2 shows the eigenvalue spectra for single phase and particulate flows. Both spectra have a similar shape where the classical A, P, S branches are clearly defined, with the leading eigenvalue located in the 'P'-branch for both single phase and particulate flows (Mack, 1976). This holds true for all values of f and S. The changes in eigenvalues due to the addition of particles are mild, with the shape of the spectrum qualitatively unchanged.

2.7.2 Eigenmodes profiles

It is possible to retrieve the radial velocity profile from the eigenvectors $\mathbf{q}$: $\hat{\mathbf{u}}(r) = \sum_n^N q_n T_n(r)$.

Figure 2.3 shows the distribution of the fluid energy in the leading eigenmode (located in the A-branch as seen in Figure 2.2) for various Reynolds and dimensionless relaxation times. The amplitude

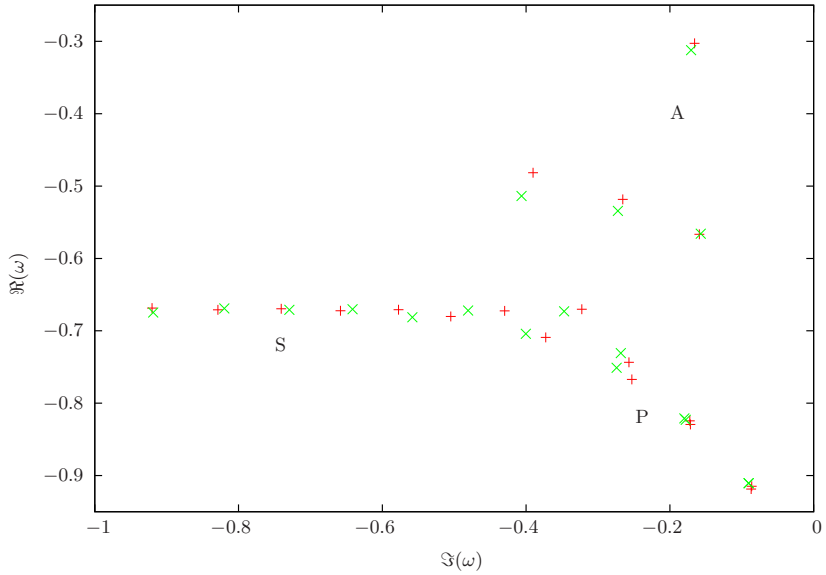

Figure 2.2: Eigenvalue spectra for the generalised eigenvalue problem given in Equation (2.21) for $Re = 1000$, $S = 10^{-3}$, $\alpha = 1$, $f = 0.1$. The classical single phase eigenvalues are represented by green crosses while the eigenvalues for the particulate flow are in red. The three branches of the eigenvalue spectrum are labelled A, P and S.

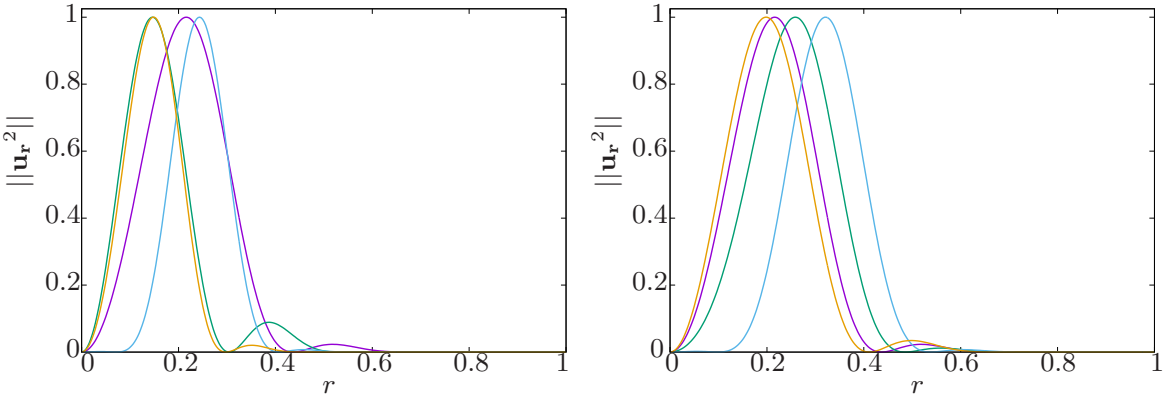

Figure 2.3: Fluid energy profile of the leading mode for uniform particle distribution, $f = 0.01$, $\alpha = 1$, $m = 0$. **Left:** $Re = 1000$, $S = 10^{-4}$ (blue), $S = 10^{-3}$ (green), $S = 2 \times 10^{-3}$ (purple), $S = 10^{-2}$ (orange). **Right:** $S = 10^{-3}$, $Re = 1000$ (purple), $Re = 2000$ (green), $Re = 3000$ (blue), $Re = 5000$ (orange).

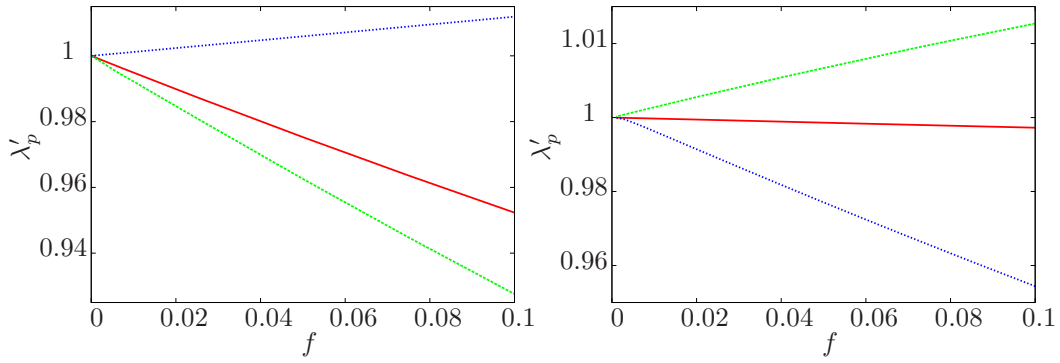

Figure 2.4: Normalised growth rate, λ_p', as a function of f for $S = 10^{-3}$ (red), $S = 10^{-2}$ (green), $S = 10^{-1}$ (blue) with $Re = 1000$, $\alpha = 1$ and $m = 0$ (left) or $m = 1$ (right). In all cases examined, λ_p' is very close to being linearly proportional to f.

of the eigenvalue obtained has no physical meaning, therefore, it has been normalised for ease of read. For all the considered cases, the energy is concentrated close to pipe centre, between $r = 0.15$ and $r = 0.3$. There is a second, much smaller peak closer to the wall (at $r \simeq 0.4 - 0.5$). There are variations as a function of S and Re but they do not seem to form a pattern.

2.7.3 Effect of the Reynolds number Re and particle concentration f

We now consider the leading eigenvalues of the particulate flow normalised by the leading eigenvalue of the single phase flow with the same Reynolds and wavenumber in order to highlight the particles effect on the growth rate:

$$\lambda_p'(Re, \alpha, m, f, S) = \frac{\Im\{\omega_p(Re, \alpha, m, f, S)\}}{\Im\{\omega_f(Re, \alpha, m)\}} \,. \tag{2.28}$$

Assuming that both $\Im\{\omega_p\}$ and $\Im\{\omega_f\}$ are negative, $\lambda_p' > 1$ implies that the growth rate is smaller (more negative) due to the addition of particles. It can be interpreted as a stabilising effect on the flow. If $\lambda_p' < 1$; the effect is opposite, the growth rate of the particulate flow is closer to 0. In the critical case, $\lambda_p' = 1$, the addition of particles has no effect on the stability.

Let us focus first on the influence of the particle concentration, for a given α, Re and S. We consider $f \in [10^{-4}, 0.1]$, as the model loses its physical relevance for $f > 0.1$.

Figure 2.4 shows λ_p' as a function of f for $Re = 1000$ for various values of S and both $m = 0$ and $m = 1$. The normalised eigenvalue depends almost linearly on the mass concentration f for all values of S, regardless of whether the flow is stabilised or made less stable by the addition of particles. If $\lambda_p' > 1$ for any given value of f, then $\lambda_P' > 1$ for all f, this results holds true for all values of Re, S, α and m considered. Consequently, f has no influence on whether adding particles will have a

Reynolds number	Particulate flow	Single phase flow	Normalised error
Re	$\Im\{\omega_p\}$	$\Im\{\omega_f\}$	$(\Im\{\omega_p\}-\Im\{\omega_f\})/\Im\{\omega_f\}$
10^3	-9.035363×10^{-2}	-9.035360×10^{-2}	2.11979×10^{-5}
5×10^3	-4.020116×10^{-2}	-4.020116×10^{-2}	9.436171×10^{-8}
10^4	-2.838510×10^{-2}	-2.838510×10^{-2}	3.883010×10^{-8}
10^5	-8.954544×10^{-3}	-8.954547×10^{-3}	5.844879×10^{-7}

Table 2.5: Comparison of leading growth rates between single phase and particulate flows for $S\to\infty$ (numerically, we fixed $S=10^3$), theoretically, $\Im\{\omega_p\}=\Im\{\omega_f\}$.

stabilising effect on the flow or not. Moreover, as the relation between λ_p' and f is almost linear, if one knows how the the value of λ_p' for a given f, it is straightforward to extrapolate a reasonably accurate approximation of λ_p' for any f. The linear relation between f and λ_p' seems at first glance to be an artefact of the simplified system of equations used in this work. However, we were unable to find the relation through theoretical analysis. f can be removed from the list of relevant parameters without losing information besides the magnitude of the effect. For the uniform problem, we fix $f=0.01$, keeping in mind that effect sizes would be increased with f. The flow stays stable as $Re\to+\infty$, consequently, we expect the variation in eigenvalue due to the particles not to increase with Re; this is confirmed in Figures 2.5 and 2.6. The particles only have limited effect on the growth rate of the perturbations (the difference is below 5%), although this value depends on the f. For $S=10^{-3}$, the normalised growth rate λ_p' only varies slightly as a function of Re. The values for $m=0$ and $m=1$ are almost equal, except for a small peak below $Re=1000$ for $m=1$. There is more variation for $S=10^{-1}$ and $S=10^{-2}$; the effect of the solid phase gets smaller as Re increases, with $\lambda_p'\to1$ as $Re\to+\infty$.

2.7.4 Influence of the relaxation time S

The effect of particle size or relaxation time is represented by the variation of λ_p' with S, for fixed values of Re, f and α. We recall that S is a measure of either the particle size or the density ratio but is not directly linked to the concentration.

2.7.5 Effect on the growth rate in the small and large Stokes limits

In the ballistic limit $S\to+\infty$, Klinkenberg et al. (2011) found that in the case of a plane Poiseuille flow, particles are too massive to be affected by the flow and the particle motion becomes independent of the flow. This is true for the pipe flow as well, as shown in Table 2.5. The growth rate for $S\to+\infty$

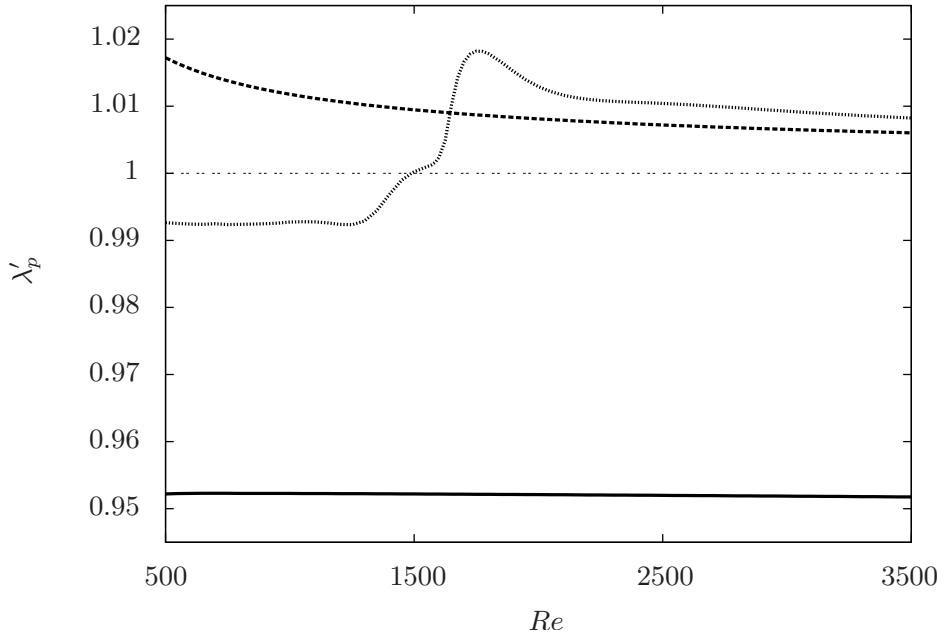

Figure 2.5: Normalised leading growth rate, λ_p' for $m = 0$ as a function of Re, for $S = 10^{-3}$ (line), $S = 10^{-2}$ (dots), $S = 10^{-1}$ (dashed) with $f = 0.01$, $\alpha = 1$ and $m = 0$. While the largest and smallest values of S present straightforward, monotonic behaviour, the intermediate $S = 0.01$ presents non-trivial variation with the Reynolds number.

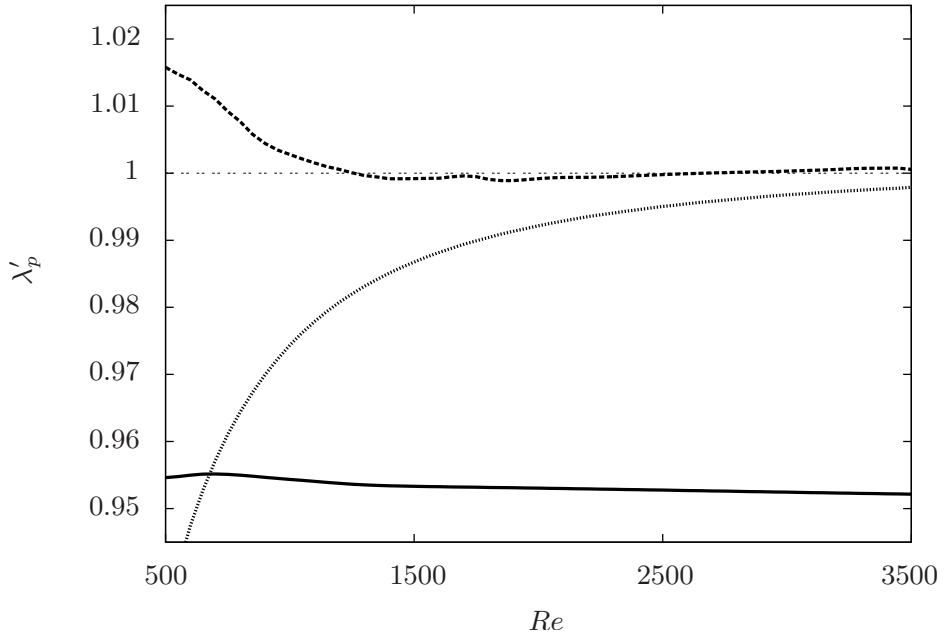

Figure 2.6: Normalised leading growth rate, λ_p' for $m = 1$ as a function of Re, for $S = 10^{-3}$ (line), $S = 10^{-2}$ (dots), $S = 10^{-1}$ (dashed) with $f = 0.01$, $\alpha = 1$ and $m = 1$. The behaviour for $S = 10^{-3}$ is very similar to the streamwise independent case. The other cases are more distinct, both converges towards 1 as Re increases.

$Re(Re')$	f	α	$\Im\{\omega_p(Re)\}$	$\Im\{\omega_f(Re')\}$	Normalised error
$10^3(1.1\times10^3)$	0.1	1	-8.614154×10^{-2}	-8.615602×10^{-2}	1.680672×10^{-4}
$10^4(1.1\times10^4)$	0.1	1	-2.706733×10^{-2}	-2.706213×10^{-2}	1.921504×10^{-4}
$10^3(1.1\times10^3)$	0.05	1	-8.818362×10^{-2}	-8.818405×10^{-2}	4.876165×10^{-6}
$10^4(1.1\times10^4)$	0.05	1	-2.769711×10^{-2}	-2.770116×10^{-2}	1.462030×10^{-4}
$10^3(1.1\times10^3)$	0.1	2	-6.191476×10^{-2}	-6.194126×10^{-2}	4.278247×10^{-4}
$10^4(1.1\times10^4)$	0.1	2	-3.850213×10^{-2}	-3.850214×10^{-2}	1.688218×10^{-8}

Table 2.6: Comparison of leading growth rates for $S\to0$ (numerically, we fixed $S=10^{-6}$).

is very close by the growth rate of the single phase flow, the difference due to numerical error. The limit $S\to0$ corresponds to small particles with a small relaxation time. The particles behave like passive tracers, they closely follow the fluid and do not affect the behaviour of the flow. However, as particles, much heavier than the fluid, are added to the flow, its average density is increased by a factor $(1+f)$. Consequently, the effective Reynolds number of the flow becomes $Re'=Re(1+f)$. This implies that if the growth rate of a particulate flow obtained at a Reynolds number Re is equal to the growth rate of the single phase flow at a Reynolds number $Re'=(1+f)Re$, both exhibits identical properties, the difference in growth rate only being due to a difference in average density. This is what occurs when $S\to0$, as illustrated in Table 2.6 which shows examples of growth rates for particulate flows and single phases flow with Reynolds numbers Re and $(1+f)Re$ respectively, for $S=10^{-6}$. The normalised difference is consistently below 5×10^{-4}. In this case, the addition of particles makes the flow less stable, but only through the modification of the average density of the fluid. Klinkenberg et al. (2011) found a similar result in the case of the plane Poiseuille flow. It has also been found that the normalised leading eigenvalue stays almost constant for S in the range 10^{-7} to 10^{-4}.

2.7.6 Effect on the growth rate for moderate values of S

Figure 2.7 shows the variations of λ_p' with S for fixed values of Re and α respectively. All curves have the same shape. λ_p' first decreases for small particles, reaching a minimum $\lambda_p'^m$ for a relaxation time S^m. λ_p' then increases above one for larger particles; in this case the addition of particles makes the flow further away from linear instability. A similar result has been found in Klinkenberg et al. (2011) for a plane particulate Poiseuille flow. A maximum $\lambda_p'^M$ is then reached for a relaxation time S^M; λ_p' converges towards unity as $S\to+\infty$. The range around the two peaks can be described as an "effective range" where the flow is most affected by the particles and where the effect changes sharply with little particle size variation. The curves are shifted towards smaller relaxation time as the Reynolds number increases.

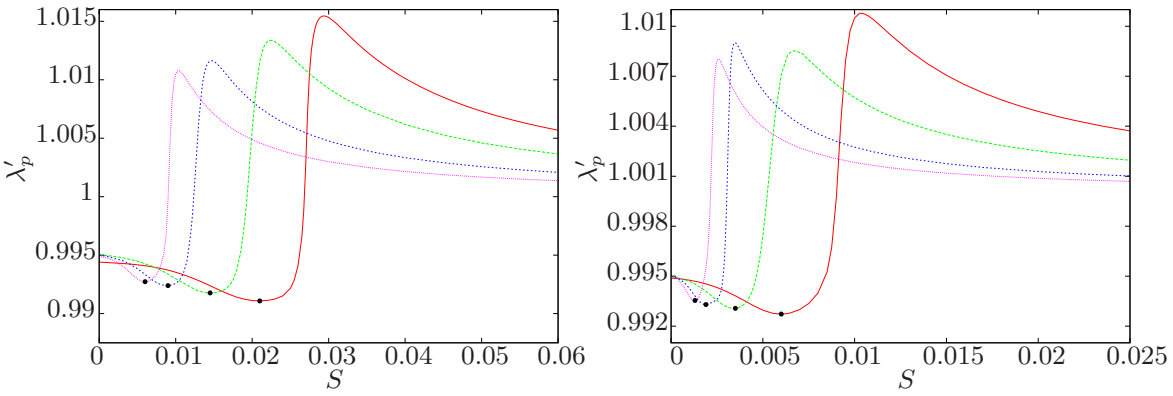

Figure 2.7: Normalised leading growth rate as a function of S, $f = 0.01$. **Left:** $\alpha = 2$, $Re = 10^3$ (red), $Re = 3 \times 10^3$ (green), $Re = 10^4$ (blue), $Re = 2 \times 10^4$ (purple). **Right:** $Re = 1000$, $\alpha = 0.2$ (red), $\alpha = 0.4$ (green), $\alpha = 1$ (blue), $\alpha = 2$ (purple).

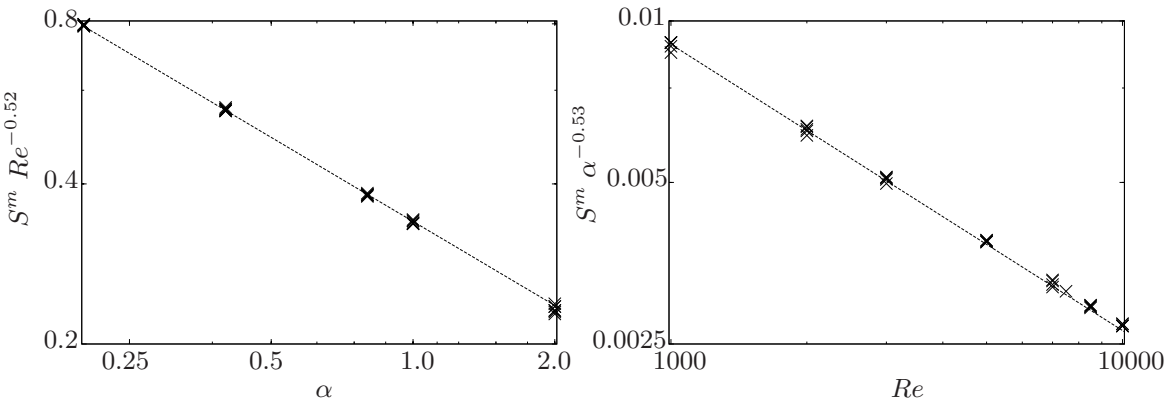

Figure 2.8: The variation of S^m with Re and α. The data can be collapsed down on to a single line by using an appropriate rescaling for the Reynolds and wavenumbers. **Left:** $S^m Re^{-0.52}$ (exponent approximated up to two significant digits) as a function of α. The collapsing of the data onto a single line suggests that $S^m \propto Re^{0.52}$. **Right:** $S^m \alpha^{-0.53}$ as a function of Re. The data again collapses onto a single line, though not as cleanly as for the scaling in Re. Nonetheless, suggesting that $S^m \propto \alpha^{-0.53}$.

The overall shape of the variations of λ_p' as a function of S is almost invariant when α varies as seen in Figure 2.7. However the peak is larger and the following slope is less steep for small α, suggesting that perturbations with smaller wavenumbers are affected by a broader range of particles size, but for larger wavenumbers, small changes in particle size can have greater effects. Both extrema shift towards smaller values of S as α increases, this implies that perturbations with shorter wavelength are more affected by smaller particles. Similarly, the extrema shift towards smaller values of S as Re increases. This can be explained by the dampening of the viscosity when the Reynolds number gets higher, allowing for smaller scale dynamics.

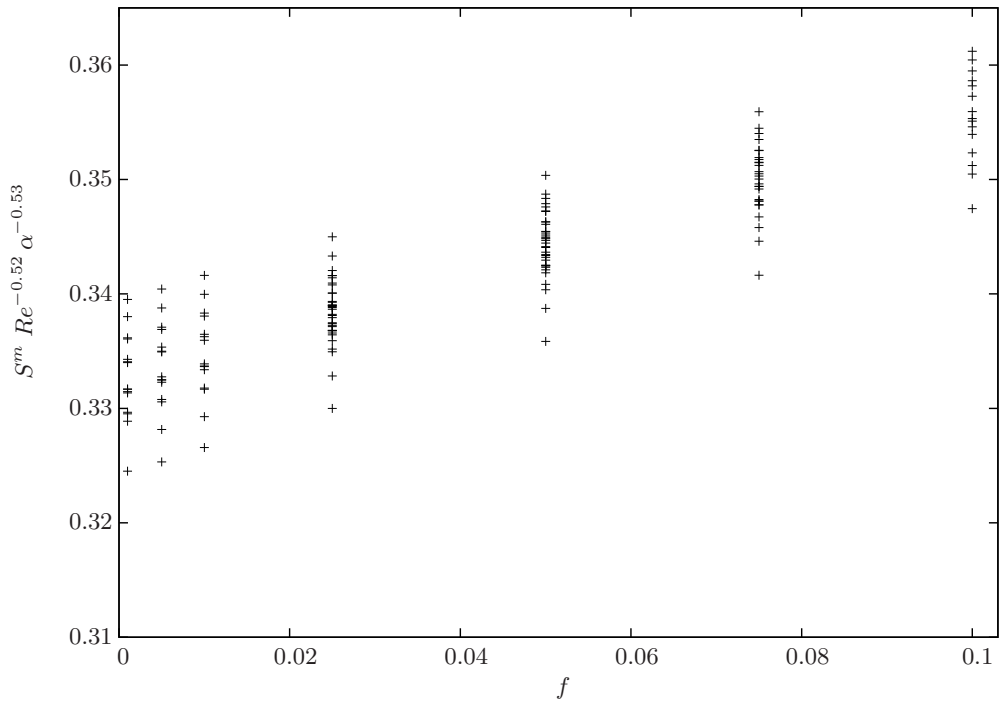

Figure 2.9: Variation of $S^m Re^{-0.52}\alpha^{-0.53}$ as a function of the mass concentration, f. While the scaled value increases with f, the variation due to f is smaller than the variation along a fixed f between different cases.

2.7.7 Reynolds and wavenumber scaling

Let us now analyse the positions and values of the extrema of $\lambda_p'(S)$ in order to determine which dimensionless relaxation time has the most effect on the linear stability. Using the two scaling simultaneously, Figure 2.8 shows that for any value of f from 10^{-3} to 10^{-1}, all data points collapse when normalised by $Re^{-0.52}$ and $\alpha^{-0.53}$. Depending on the case, the standard deviation is quite low, ranging from 1.2×10^{-3} to 3.2×10^{-3}.

Figure 2.9 shows that S^m also scales with f. However, the scaling is weak, with a variation under 10% for values of f spanning three orders of magnitude. The scaled value also shows some variation along a fixed f, but this variation is fairly low, below 10%.

Although the addition of particles for a homogeneous particle distribution only has a small to moderate effect on the growth rate, a non trivial relationship as a function of the relaxation time is still observed. There are physical explanations for the direction of the scaling with Re and α (as mentioned in Section 2.7.6). However, there are no physical or mathematical explanations, as far as our knowledge goes, for the values if the scaling. This dimensionless relaxation time for which the flow is most affected follows a scaling law with both Re and α.

2.8 Nonuniform particle distributions

So far, only uniformly distributed particles have been considered. This is however not inherent to our fully Eulerian model and one can introduce nonhomogeneous particle distributions, allowing us to consider a more general problem. Moreover, as discussed in Chapter 1, experimental work suggests that for low to moderate *Re*, particles congregate at a particular radius forming an annulus from their distribution centred in the region closer to the wall, at a radius between $r = 0.5$ and $r = 0.8$ (Jeffrey and Pearson, 1965; Matas et al., 2004b; Segre and Silberberg, 1962). From now on, we capture the essence of this by considering particle distributions varying in the radial direction, described by a function of the form:

$$N(r) = \tilde{N} \exp\{-(r - r_d)^2 / 2\sigma^2\}, \tag{2.29}$$

with $\tilde{N}$ chosen such that $\int_0^1 N(r) r dr = 1$. We still consider a uniform distribution over the azimuthal and streamwise direction. The choice is made to only consider Gaussian distributions, as they are simple and relatively close to what is observed experimentally, as seen in Section 2.9. However, in some cases the particles are shown to congregate over two distinct radius (Matas et al., 2004b) or in a non-symmetrical distribution. This work could be expended by considering more complex distribution without needing further modifications to the model. Until the end of this chapter, in order to reduce the set of parameters being considered, a portion of the problem parameters are fixed: $S = 10^{-3}$, $f = 0.1$ and $m = 1$. The values chosen for S and f are consistent with experimentally realistic parameters (see Section 2.9) while $m = 1$ is the only azimuthal wavenumber for which we observed linear instability.

2.8.1 The onset of instability

Figure 2.10 shows the leading eigenvalues for a localised distribution of particles at $r = 0.6$ compared with the uniform distribution result for both the A-branch and P-branch. While the uniform particle distribution remains stable for all *Re*, the non-uniform distribution is linearly unstable. As the particles are non-homogeneously distributed, the local particle concentration is significantly higher at the radius $r = r_d$ than in the case of an homogeneous distribution. It could be considered that the particle concentration going over a threshold could produce linear instability. However, a homogeneously distributed flow whose particle concentration is everywhere as high as the local particle concentration at $r = r_d$ of a linearly unstable flow is found to still be linearly stable. It follows that the linear instability is caused in part by the the gradient of particle concentration. Moreover linear instability only occurs for *moderate* Reynolds number, but *not* for either high or low *Re*. This result, albeit counter-intuitive, consistently holds for all cases studied. It can be explained by the Stokes term being proportional to $1/Re$ (Equations 2.10 and 2.11) i.e. for very large *Re*, there is no coupling between the fluid and solid phases, hence the flow is stable. For low *Re*, diffusion dominates and imposes stability.

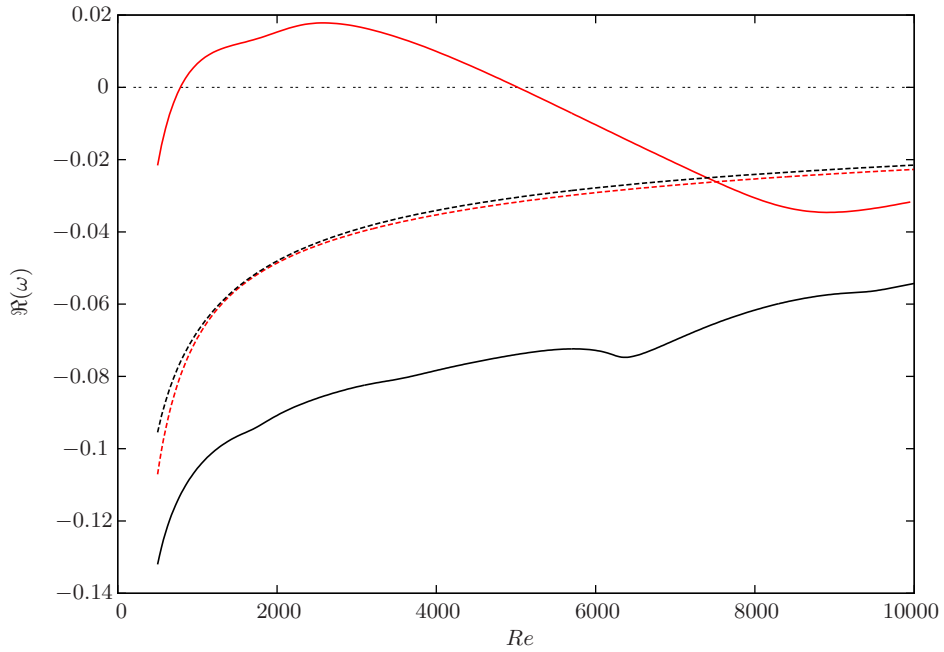

Figure 2.10: The leading eigenvalues of the A- and P branches for uniform (black) and non-uniform particle distributions, centred at $r = 0.6$ (red). The dashed lines represents the P-branch, the solid line the A-branch. The uniform distribution is stable for all Re, but the non-uniform distribution is unstable for a range of Re. For higher Re the leading eigenmode switches between A and P branches for the non-uniform distribution at the point where the two red lines meet on the graph.

Of note, the coupling between fluid and particles decaying linearly as the Reynolds number increases in only true insofar as only the Stokes drag is considered. Therefore, the fact that the flow is linearly stable for very high Reynolds numbers would not necessarily hold true for different parametric regimes where other coupling forces have to be considered. Therefore, linear instability is only feasible for intermediate values of the Reynolds number. Another point is that while the change is quite dramatic for the leading eigenvalue of the A-branch, the leading eigenvalue of the P-branch, which is the least stable eigenvalue in the single phase flows and particulate flows with uniform distribution, is much less affected by the change in the particle distribution. For higher Re, after the flow has restabilised, we observe that there is a switching of the leading eigenvalue at around $Re = 6000 - 8000$, after which the dominant eigenvalue appears to be the same as for the uniform problem. The eigenvalue spectrum (Figure 2.11) shows that for an unstable configuration, the leading eigenvalue is not in the P-branch as in the case of both the non-particulate and uniformly distributed problems but rather in the A-branch. This is in agreement with what is shown in Figure 2.10. The reason for the switching of the least stable eigenvalue from the P-branch to the A-branch can be explained by looking at the eigenmodes associated with the leading eigenvalues for a homogeneous and nonhomogeneous particle distributions and how they differ. In Figure 2.12, the leading eigenmodes of the two branches are plotted for a homogeneous distribution and a nonhomogeneous one with $r_d = 0.7$ and $\sigma = 0.1$. The overall shape is relatively insensitive to the distribution of particles, but the modes of the two branches

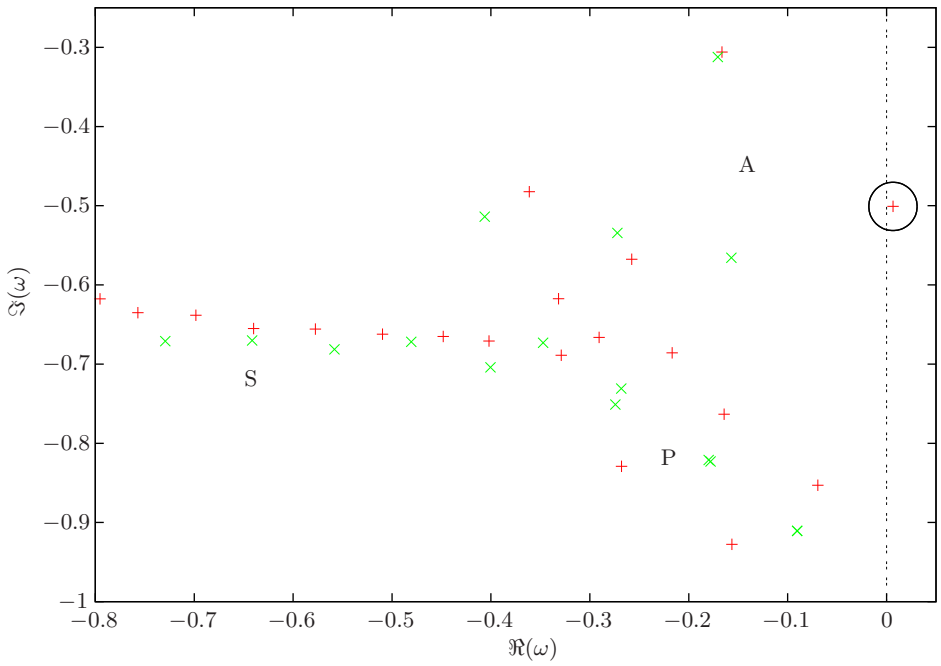

Figure 2.11: Eigenvalue spectra for the non-particulate (green) and particulate cases (red). In both cases, $Re = 1000$, $\alpha = 1$ and $m = 1$ while the particles were non-uniformly distributed with $f = 0.1$, $r_d = 0.6$ and $\sigma = 0.1$.

are primarily active in different parts of the pipe. For the P-branch, the eigenmode is localised at a closer to the centre of the pipe (with the eigenmodes centred around at $r \simeq 0.3$). This is similar to what was observed in Figure 2.3 for a uniform particle distribution. On the other hand, the A-branch mode is located closer to pipe wall ($r \simeq 0.7$). It is therefore unsurprising that when the particle distribution is centred near this outer location, these are the eigenmodes that are primarily excited, as seen in Figure 2.10. Figure 2.13 shows more eigenmodes energy distribution for varying values of r_d. In the case $Re = 500$ (left graph), all the modes are associated to linearly stable cases while most modes are unstable in the case $Re = 1500$. The eigenmodes profiles are not significantly affected by whether their associated eigenvalue is unstable or not. All profiles have two peaks, one situated between $r = 0.5$ and $r = 0.7$, and another between $r = 0.75$ and $r = 0.9$; their shape is, however, dependent on r_d. Some cases have a peak closer to the centre which is almost an order magnitude larger than the other, such as $r_d = 0.65$ in Figure 2.13, while other cases have peaks of near-equal magnitude, for example when $r_d = 0.70$.

In addition to being unstable for a finite range of Re, the flow is also only unstable for a finite range of streamwise wavenumbers α as illustrated in Figure 2.14. For both small and large wavenumber disturbances, the flow is stable. The later is to be expected due to the stabilising influence of viscosity, but it is important to note that the instability exists at very moderate wave numbers for which the model is valid.

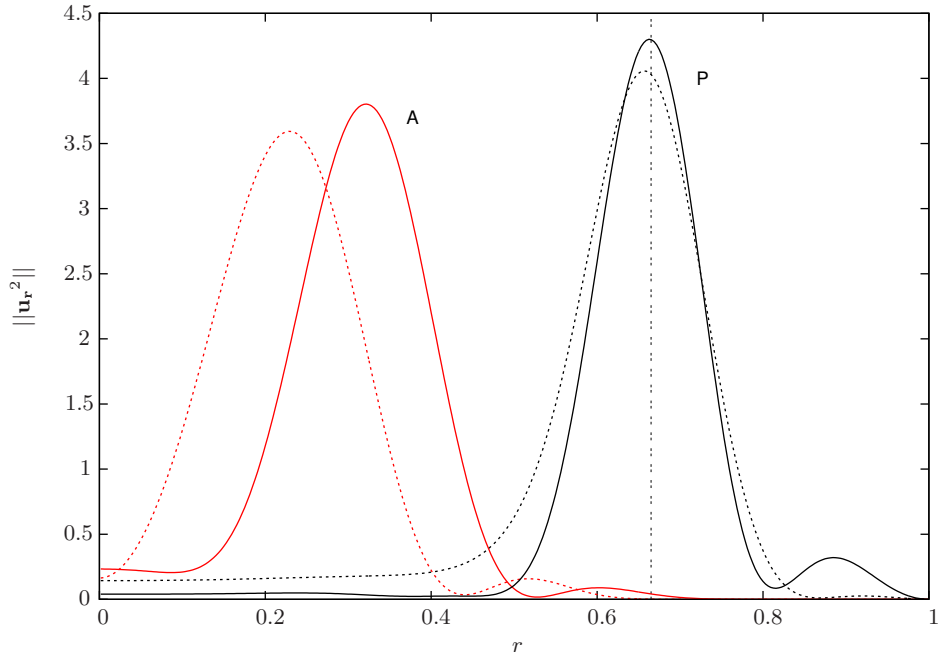

Figure 2.12: The distribution of the fluid energy in the leading eigenmode for the non particulate (solid line) and particulate case (dashed). The two that peak on the left (in red) are the leading P-branch modes while the black lines represent the leading A-branch modes. For the particulate case the particles are non-uniformly distributed with $Re = 1000$, $m = 1$, $f = 0.1$, $S = 10^{-3}$, $r_d = 0.7$ and $\sigma = 0.1$. The vertical line is at $r_d^* = 0.666$.

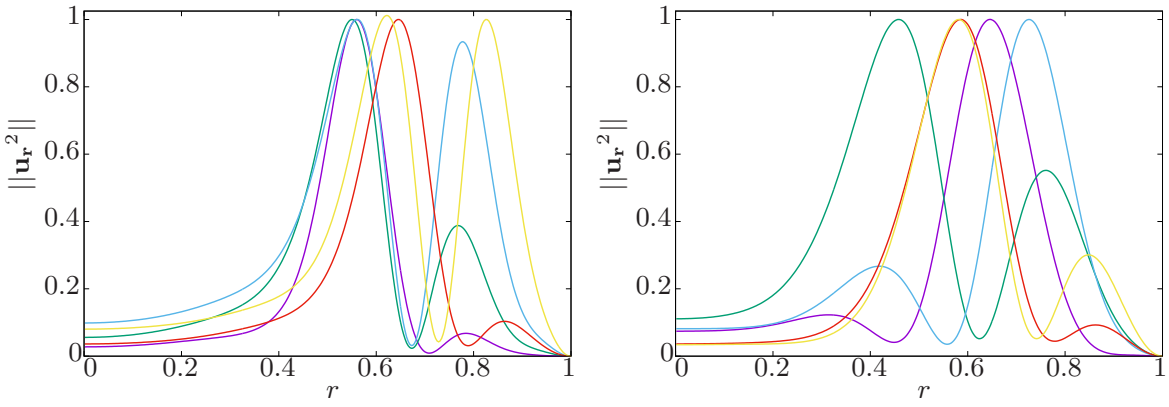

Figure 2.13: Fluid energy profile of the leading mode for nonhomogeneous particle distribution centred around varying radii, $f = 0.01$, $S = 10^{-3}$, $\alpha = 1$, $m = 1$, $\sigma = 0.1$. $r_d = 0.50$ (purple), $r_d = 0.55$ (green), $r_d = 0.60$ (blue), $r_d = 0.65$ (red), $r_d = 0.70$ (yellow). **Left:** $Re = 500$. **Right:** $Re = 1500$.

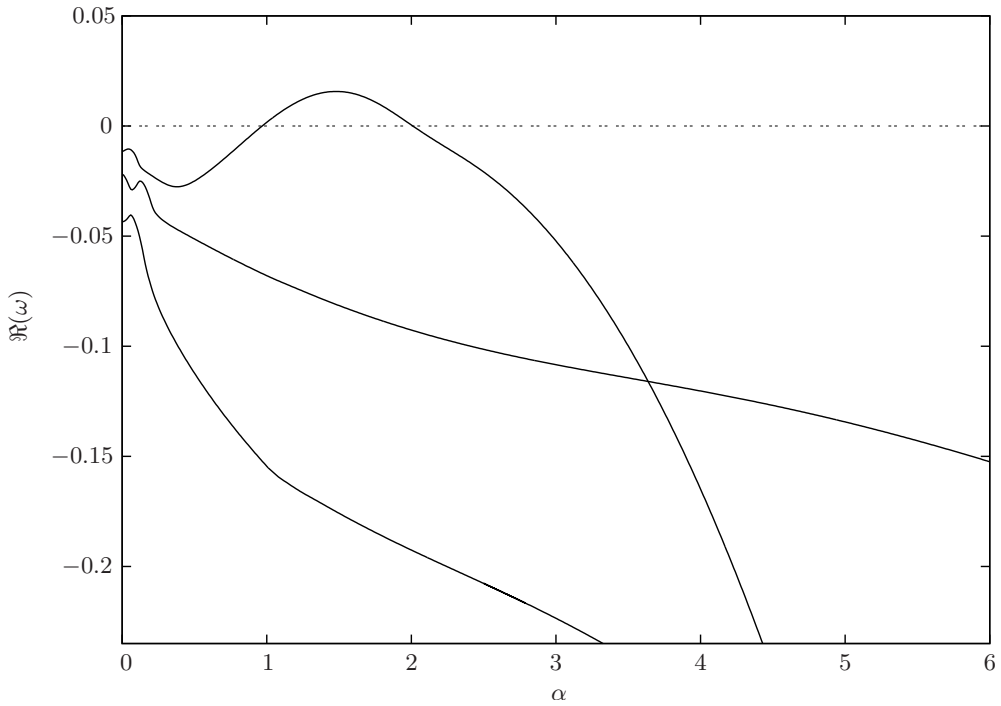

Figure 2.14: The particulate flow three leading growth rates for $Re = 1000$, $m = 1$, $f = 0.1$, $S = 10^{-3}$, $r_d = 0.65$ and $\sigma = 0.1$. Instability ($\Re\{\omega\} > 0$) occurs for a finite range of α.

2.8.2 Effect of the particle concentration and streamwise wavenumber on the critical Reynolds number

Figure 2.15 gives neutral stability curves for varying values f and r_d. Slight changes of either f or r_d have drastic effects on the stability, even as all others parameters are kept constant. All curves are closed, confirming the restabilisation with increasing Re (and α). The cut-off values of α for which linear instability is observed is dependent on the other flow parameters, but the minimum and maximum values of α where linear instability are observed are in the same region, between $\alpha = 0.5$ and $\alpha = 2.5$. The left graph in Figure 2.15 illustrates the purely destabilising effect of the particle concentration f. The unstable area of a smaller f is entirely comprised inside the one of a larger f, forming concentric circles.

On the other hand, there are overlaps when varying r_d, the size of the unstable area as well as the minimum Re_c change with r_d. The overall shape of the contour is also dependent on r_d, while in all cases Re_c only weakly depends on α, with the exception of the edges where the value of α for which Re_c is minimised can significantly vary with r_d and α. The maximum Re for which the flow is unstable mostly depends on α.

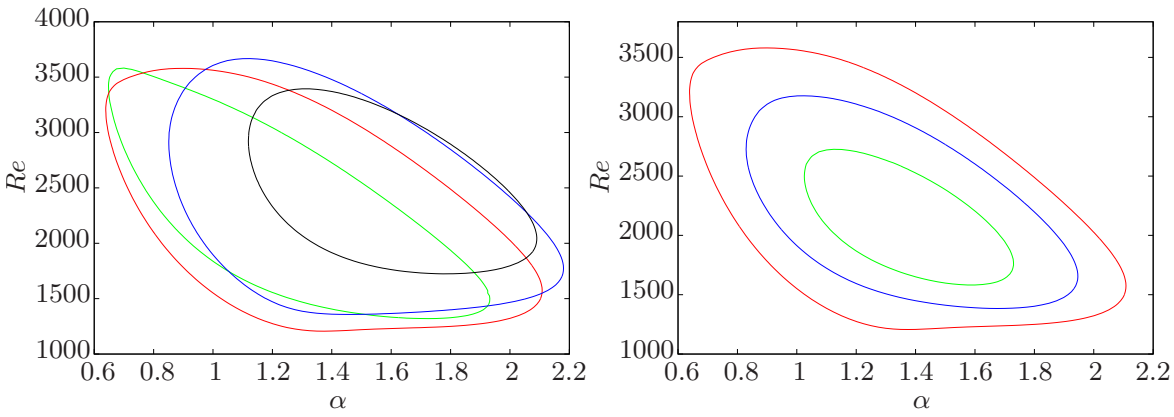

Figure 2.15: **Upper:** Contours of neutral stability in $Re-\alpha$ space for values of f and r_d, the enclosed region is the unstable region. **Left:** Fixed $f=0.075$, $r_d=0.55$ (black), $r_d=0.60$ (blue), $r_d=0.65$ (red), $r_d=0.55$ (green). **Right:** Fixed $r_d=0.7$, $f=0.055$ (green), $f=0.065$ (blue), $f=0.075$ (red).

2.8.3 Effect of the radial distribution of particles

The exact location where the particle concentration annulus, r_d, is centred as well as how sharply the distribution peaks around this location is of critical importance in determining whether the flow becomes unstable or not. By searching over α we can trace out neutral stability contours in $Re-r_d$ space for differing values of σ (Figure 2.16). The enclosed regions are unstable, all the contours are closed. The fact that there is a minimum/maximum value of Re for which the flow is unstable is consistent with our earlier observations, while the fact that there are bounds on the value of r_d supports the hypothesis of needing to excite the P-branch in order to destabilise the flow. We note that for all values of σ the curves are concentric and the broadest range of unstable Re occurs when r_d is in the region $0.6-0.7$.

We track the maximum and minimum values of r_d for which instability exists in Figure 2.16 (lower). There is a maximum value of σ beyond which instability isn't possible, this is coherent with our earlier findings. Indeed, in the case of an homogeneous particle distribution the flow is always linearly stable, and as σ increases the particle distribution becomes more similar to an homogeneous particle distribution. The minimum degree of localisation required to trigger instability corresponds to $\sigma^*=0.111$, for which the particle distribution must be centred at $r_d^*=0.666$.

2.9 Relevance to experimental configurations

As mentioned in Section 1.9.2, particles have been experimentally observed to converge at a certain radius in pipe flows. Matas et al. (2004b) notably highlight the clustering of particles at preferential radii but they do not report evidence of a linear instability. This springs our motivation for the

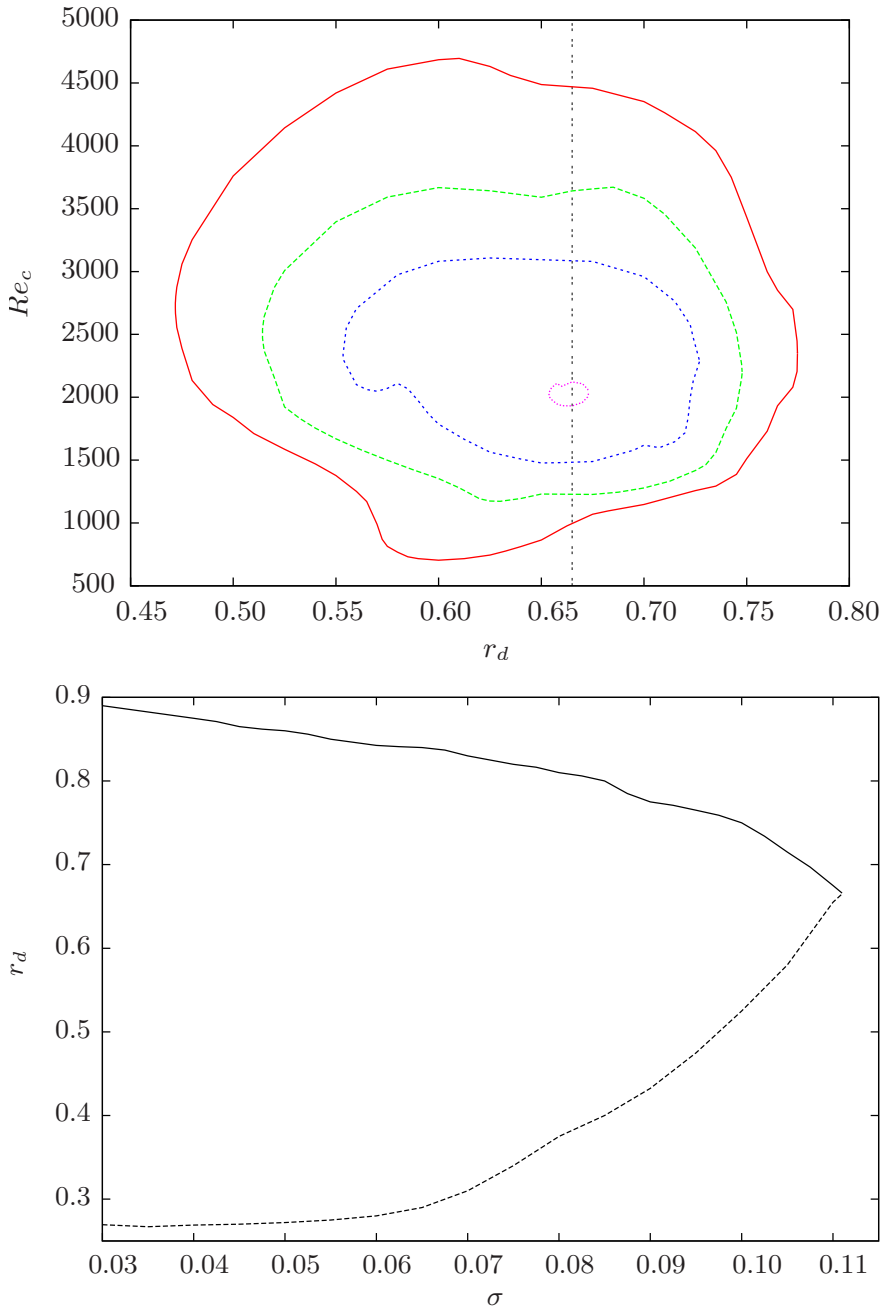

Figure 2.16: **Upper:** Contours of neutral stability in $Re - r_d$ space for values of $\sigma = 0.110$ (purple), 0.105 (blue), 0.100 (green) and 0.095 (red). In each case, the enclosed region is the unstable region. All the contours are closed, which indicates that there is a maximum/minimum value of both Re and r_d for which flow is unstable. **Lower:** The maximum (solid)/minimum (dashed) values of r_d for which the flow becomes unstable as σ is varied, across all Re and α.

following section where we analyse the configurations observed by Matas et al. (2004b) and show that our numerical results are consistent with the experiments - i.e. we find the configurations to be linearly stable. In the experimental work, four configurations of particles are explicitly given (see

Figure 2.17), corresponding to $Re = 67$, 350, 1000 and 1650, from top right to bottom left. At low Re, all the particles cluster at a single radius consistent with the behaviour observed in Segre and Silberberg (1962). As Re is increased, two preferential radii emerge and coexist. We capture these distributions within the linear stability analysis with two approaches. Firstly, we fit either one or two Gaussian distributions through the data using least squares. These fits and the corresponding fitting parameters are those given in 2.17. Secondly, the raw data from Matas et al. (2004b) is used to produce a discontinuous distribution, the value $N_0(r)$ being estimated constant between any two mesh points (see Figure 2.17).

Re	S	λ_f	λ_G	λ_d
67	2.743×10^{-3}	-0.58409	-0.55828	-0.56033
350	2.743×10^{-3}	-0.14605	-0.17752	-0.16606
1000	7.689×10^{-4}	-9.1143×10^{-2}	-0.10635	-0.10480
1650	7.689×10^{-4}	-7.4771×10^{-2}	-9.9083×10^{-2}	-9.4478×10^{-2}

Table 2.7: Comparison of leading eigenvalues for the linear stability problem obtained in cases without particles, with particle distributions experimentally found by Matas et al. (2004b), and the closest Gaussian fit respective of particle distributions.

Table 2.7 gives the growth rates of the leading eigenvalues for a non-particulate flow (λ_f), particles distributed continuously (λ_G), and distributed discontinuously (λ_d) for the four different configurations reported by Matas et al. (2004b). For the lowest Reynolds number, $Re = 67$, both distributions of particles reduce the stability of the flow, but not so far as to make it unstable. On the other hand, for higher values of Re the particles have a stabilising effect on the flow. These effects apply to both the Gaussian and discontinuous particle distributions, all growth rates agree within 7%, much less than the discrepancy with the non-particulate case. We conclude that within the set of cases experimentally studied, our numerical results are fully consistent with the observations.

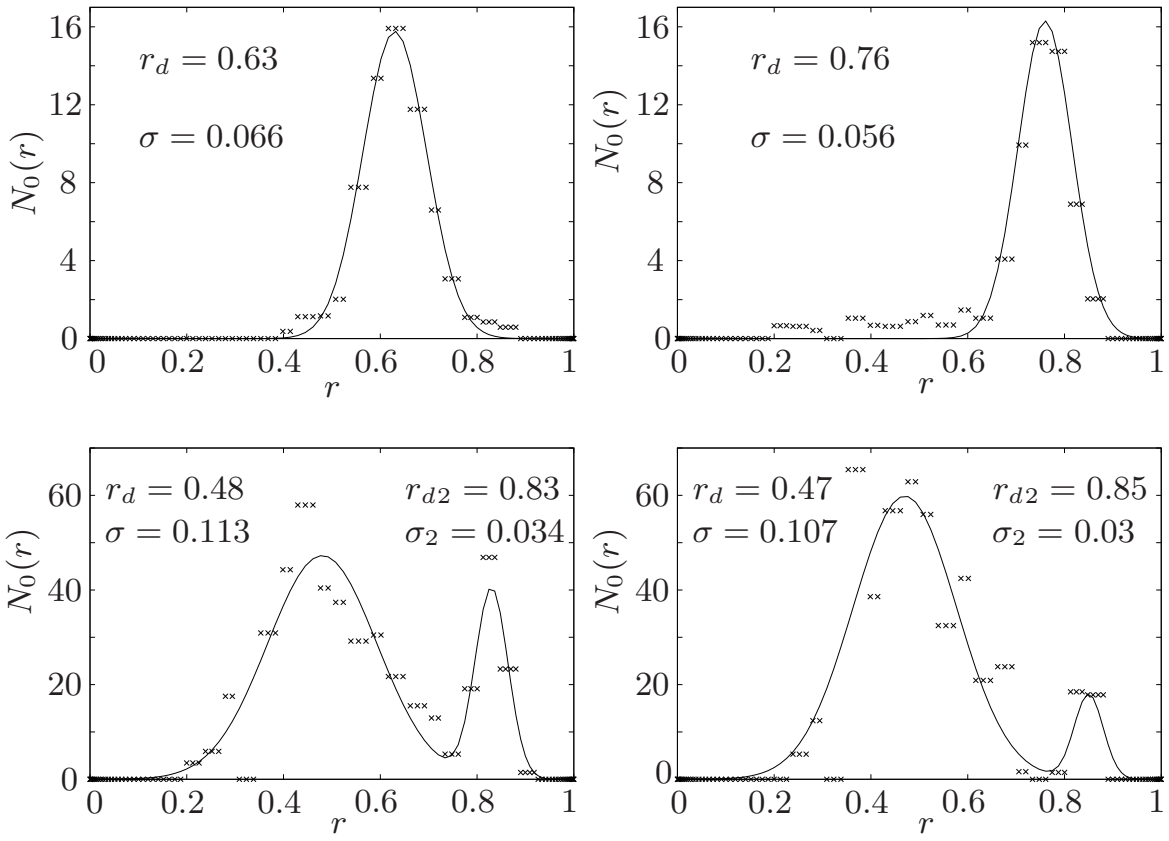

Figure 2.17: Particles concentration as a function of the radius. The crosses show the experimental results of Matas et al. (2004b) while the lines are our fitted distributions. The top two graphs, ($Re = 67$ (left) and $Re = 350$ (right)) were fitted using a single Gaussian distribution centred at r_d and of width σ. For the bottom graphs ($Re = 1000$ (left) and $Re = 1650$ (right)) each set of data was fitted with the sum of two Gaussian distributions.

2.10 Conclusion

We studied the effect of the addition of particles on the linear stability of particulate pipe flows with a fully Eulerian method. For homogeneous particle distribution, the effect is limited; the particulate pipe flow remains stable for all parameters considered. The effect of the particle mass concentration f is monotonic and almost linear. Re also has a limited effect on the growth rate which tends to decrease as Re increases. The effect of the dimensionless relaxation time on the growth rate shows a more complex behaviour, with a nonmonotonic curve and two extrema. Moreover, both these extrema scale with α and Re.

Nonhomogeneous particle distribution have also been studied in the form of Gaussian distributions centred around a radius r_d with a standard deviation σ, close to the particle distribution observed experimentally in Matas et al. (2004b). The addition of particles has a much stronger influence on the linear stability of the flow for nonhomogeneous particle distributions, and linear instability occurs for

a window of Re and α, condition to the azimuthal wavenumber $m = 1$. Interestingly, linear instability only occurs for intermediate Reynolds numbers. This intermediate regime is sandwiched between low Re flows dominated by viscous diffusion and high Re flows where fluid and solid phase are not coupled any more. The effect of particles gets stronger as particles get more clustered, corresponding to a decrease of σ in our problem. The radius where particles are positioned is a critical parameter. Closer to the pipe centre, for $r_d < 0.3$, particles have a stabilising effect on the flow; for $0.4 < r_d < 0.9$, the particles strongly destabilise the flow. The particles' influence is strongest around $r_d \simeq 0.66$, close to the peaks observed in the eigenfunctions in Figure 2.12 and to the Segré-Silberberg radius. Another point only briefly mentioned are physical explanations for the effect of particles on the flow. Giving the physical mechanism leading to our results is tricky as our model is fairly simplistic and not completely realistic, we can still make hypothesis as the most likely mechanisms. In case of smaller particles, linear instability is possible, but only when the particles are concentrated where the eigenfunction is the highest. The instability is possibly caused by the particles excite one of the mode of the perturbation, with the effect magnified around $r_d \simeq 0.65$. Larger particles have a stabilising effect on the flow, possibly due to the increased dissipation added by the Stokes drag (Klinkenberg et al., 2011). The results obtained in this Chapter are not sufficient to give a full picture of transition to turbulence in particulate flows as only linear stability is considered and some of the physical mechanisms have been neglected. The linear instability found within this framework reveals a new possible transition scenario and highlight the complexity of the problem.

Chapter 3

Linear transient growth of the particulate pipe flow

As seen in Chapter 2, the addition of particles can, within the framework of the Eulerian model used, lead to linear instability in a pipe flow. Even when the particulate flow is linearly stable, interactions between the disturbance and the underlying flow can lead to large distortions of the base flow due to the non-normality of the linear problem, such that perturbations can still experience growth at finite time (Bergström, 1993; Waleffe, 1995). The linear stability analysis allowed the study of the asymptotic behaviour of the particulate flows and showed that the addition of particles could have a drastic impact. The main goals of this linear transient growth study is to observe the effect of the particles on the stability at finite times, and in particular if it can lead to new mechanism for instability in the case of nonhomogeneous particle distributions. This transient growth can lead to different mechanisms for the transition to turbulence. The subsequent chapter deals with the transient growth of particulate flows. The model used for the particles is the same two-way coupled, fully Eulerian method used in Chapter 2. In this chapter, we study the effect of the particles on the energy stability as well as the transient growth and the velocity profiles associated.

3.1 Theory

As discussed in Section 1.8.2, the transient growth corresponds to the ratio between the maximum energy a perturbation that evolves according to the linearised equations of motion can have at a time T, given an initial energy E_0.

$$G(T,Re) = \max_{\mathbf{u}(0)} \frac{E(\mathbf{u}(T))}{E(\mathbf{u}(0))} \,. \tag{3.1}$$

The perturbation $\mathbf{u}(0)$ causing the largest amount of growth is often referred to as the optimal disturbance. By optimising over T, one can find the maximum possible growth at a given Reynolds number, $G_{max}(Re)$. The values of interest are then this maximum growth and its associated time, T_{max}.

In the case of the single phase pipe flow, the transient growth is primarily driven by streamwise-independent rolls ($m = 1$) which generate streaks (Bergström, 1992). The time at which the peak in energy is reached increases linearly with the Reynolds number of the flow while the optimal linear transient growth scales with Re^2 for all modes (Bergström, 1993). The transient growth problem can be solved using either a matrix-based or a variational method (Kerswell, 2011). The matrix-based

method uses the same formulation as the linear stability analysis. The linear Navier-Stokes equations can be written as an eigenvalue equation system, equivalent to the one used for the linear stability analysis in Section 2.4:

$$i\lambda \mathbf{A}\phi = \mathbf{B}\phi \quad \text{or} \quad i\lambda\phi = \mathbf{L}\phi \,, \tag{3.2}$$

with λ being the eigenvalue vector and ϕ, the eigenfunctions of the problem, here $\mathbf{L}$ is a linear operator. The optimal growth can be computed from ϕ using a Singular Value Decomposition method. The matrix-based method has the advantage of being solved without a time-based computation.

However, the number of modes M needed to obtain convergence make the method unwieldy. as $M > 400$ are often needed to converge. While for linear stability analysis, only the value of the leading eigenvalue and eigenfunction are needed, linear transient growth require at least the first ten eigenvalues, therefore the number of modes necessary is significantly higher and the accuracy lower. This issue is even more salient in our problem as there are seven variables, so the effective size of the matrix is $7M \times 7M$. In this case, the matrices get too large to be handled with the LAPACK libraries. Therefore, in order to find the optimal growth, a variational method approach which does not require the use of matrices has been used. The problem described by Equations (2.15)-(2.18) can be characterised with the following functional $\mathscr{L}$:

$$\begin{aligned}
\mathscr{L} = &\left\langle \frac{1}{2}\left(m_f \mathbf{u}^2(T) + m_p \mathbf{u_p^2}(T)\right)\right\rangle - \lambda\left[\left\langle \frac{1}{2}\left(m_f \mathbf{u^2}(0) + m_p \mathbf{u_p^2}(0)\right) - E_0\right\rangle\right] \\
&- \int_0^T \left\langle \Upsilon \cdot \left(\partial_t \mathbf{u} + \nabla p + \mathbf{U}\cdot\nabla\mathbf{u} - \mathbf{u}\cdot\nabla\mathbf{U} - \frac{1}{Re}\nabla^2\mathbf{u} - \frac{fN_0}{SRe}(\mathbf{u_p} - \mathbf{u})\right)\right\rangle \mathrm{d}t \\
&- \int_0^T \left\langle \Upsilon_p \cdot \left(\partial_t \mathbf{u_p} + \mathbf{u_p}\cdot\nabla\mathbf{U} + \mathbf{U}\cdot\nabla\mathbf{u_p} - \frac{1}{SRe}(\mathbf{u} - \mathbf{u_p})\right)\right\rangle \mathrm{d}t \\
&- \int_0^T \langle \Pi \cdot \nabla\cdot\mathbf{u}\rangle \,\mathrm{d}t - \int_0^T \langle \Gamma \cdot (\partial_t N + N_0 \nabla\cdot\mathbf{u_p} + \mathbf{u_p}\cdot\nabla N_0 + \mathbf{U}\cdot\nabla N)\rangle \,\mathrm{d}t \,,
\end{aligned} \tag{3.3}$$

where λ, Υ, Υ_p, Γ and Π are the Lagrange multipliers enforcing the constraints of the problem: λ enforces that the energy is fixed, Υ and Υ_p enforce that Equations (2.15) and (2.16) hold true over $t \in [0,T]$, Π and Γ enforces the incompressibility of the flow and the conservation of the total number of particles. The brackets represent a normalised volume integral over the pipe, given any function f: $\langle f\rangle = \int f \,\mathrm{d}V/V_p$ with V_p the pipe volume. This approach has been developed by Andersson et al. (1999) and Guégan et al. (2006) and used for single phase pipe flows by Pringle and Kerswell (2010).

Finding the initial perturbation that will maximise energy growth is equivalent to maximising $\mathscr{L}$, done here through finding the root of its derivative $\delta\mathscr{L}$. By reordering $\delta\mathscr{L}$, one can obtain the adjoint system of equations of our problem. Since integral and differentiations are linear operators,

each term of $\mathscr{L}$ can be considered individually when computing $\delta\mathscr{L}$. A complete version of the derivation of the adjoint equations is given in Appendix A, but the process is similar for most terms. Let us take the second part of the advective term of Equation (2.15) as an example:

$$\int_0^T \langle \delta\ (\Upsilon \cdot \mathbf{U}\,\partial_z \mathbf{u})\rangle\ \mathrm{d}t = \int_0^T \langle \delta\Upsilon \cdot (\mathbf{U}\,\partial_z \mathbf{u})\rangle\,\mathrm{d}t + \int_0^T \langle \Upsilon \cdot \delta(\mathbf{U}\,\partial_z \mathbf{u})\rangle\,\mathrm{d}t\,, \tag{3.4}$$

using integration by part on the last term of Equation (3.4) one can obtain:

$$\begin{aligned}\int_0^T \langle \Upsilon \cdot \delta(\mathbf{U}\,\partial_z \mathbf{u})\rangle\,\mathrm{d}t\ &= \int_0^T \langle \Upsilon \cdot \mathbf{U}\,\partial_z(\delta\mathbf{u})\,\rangle\,\mathrm{d}t\ = \\ \int_0^T \langle \mathbf{U}\cdot\partial_z(\Upsilon\,\delta\mathbf{u})\rangle\,\mathrm{d}t\ &- \int_0^T \langle\,\delta\mathbf{u}\cdot\,\mathbf{U}\,\partial_z\Upsilon\rangle\,\mathrm{d}t\,,\end{aligned} \tag{3.5}$$

$\int_0^T \langle \mathbf{U}\cdot\partial_z(\Upsilon\,\delta\mathbf{u})\rangle\,\mathrm{d}t$ can be shown to be equal to 0 due to the periodicity of our problem in the z-direction:

$$\int_0^T \langle \mathbf{U}\cdot\partial_z(\Upsilon\,\delta\mathbf{u})\rangle\,\mathrm{d}t = \int_0^T \langle\,\partial_z(\mathbf{U}\cdot\Upsilon\,\delta\mathbf{u})\rangle\,\mathrm{d}t - \int_0^T \langle\,(\Upsilon\,\delta\mathbf{u})\cdot\partial_z\mathbf{U}\rangle\,\mathrm{d}t\,, \tag{3.6}$$

as we know, $\partial_z\mathbf{U} = 0$. Moreover, the brackets represent a volume integral over the pipe so that, using the L-periodicity in the z-direction, the second term of Equation 3.6 can be written as:

$$\int_0^T \langle\,\partial_z(\mathbf{U}\cdot\Upsilon\,\delta\mathbf{u})\rangle\,\mathrm{d}t = \int_0^T\int_r\int_\theta \left[\mathbf{U}\cdot\Upsilon\,\delta\mathbf{u}\right]_0^L \mathrm{d}r\,\mathrm{d}\theta\,\mathrm{d}t = 0\,. \tag{3.7}$$

Consequently, Equation (3.5) becomes:

$$\int_0^T \langle \delta\ (\Upsilon \cdot \mathbf{U}\,\partial_z \mathbf{u}\,\rangle\ )\,\mathrm{d}t = -\int_0^T \langle\,\delta\mathbf{u}\cdot\ (\mathbf{U}\,\partial_z\Upsilon)\rangle\,\mathrm{d}t + \int_0^T \langle \delta\Upsilon \cdot (\mathbf{U}\,\partial_z \mathbf{u})\rangle\,\mathrm{d}t\,. \tag{3.8}$$

The equations of motion for fluid and particles are given in Equation (3.3). The adjoint system of equation is:

$$\partial_t\Upsilon = -\mathbf{U}\cdot\nabla\Upsilon\ + \Upsilon\cdot\nabla\mathbf{U} - \nabla\Pi - \frac{1}{Re}\nabla^2\Upsilon + \frac{fN_0}{SRe}\Upsilon - \frac{1}{SRe}\Upsilon_p\,, \tag{3.9}$$

$$\partial_t\Upsilon_p = -\mathbf{U}\cdot\nabla\Upsilon_p + \Upsilon_p\cdot\nabla\mathbf{U} - N_0\nabla\Gamma - \frac{fN_0}{SRe}\Upsilon + \frac{1}{SRe}\Upsilon_p\,, \tag{3.10}$$

$$\partial_t\Gamma = -\mathbf{U}\cdot\nabla\Gamma - \mathbf{u_p}\cdot\nabla\Gamma\,, \tag{3.11}$$

$$\nabla\cdot\Upsilon = 0\,. \tag{3.12}$$

where Υ and Υ_p are the fluid and particles velocities respectively; Γ being the adjoint particle local concentration while Π is the adjoint pressure. Another set of conditions are obtained by enforcing $\delta\mathscr{L} = 0$ (the details of the derivation are given in Sections A.1 and A.2 of the Appendix):

$$\mathbf{u}(T) = \Upsilon(T) \quad , \quad \mathbf{u_p}(T) = \Upsilon_p(T) \, , \tag{3.13}$$

$$\lambda\mathbf{u}(0) - \Upsilon(0) = 0 \quad , \quad \lambda\mathbf{u_p}(0) - \Upsilon_p(0) = 0 \, . \tag{3.14}$$

3.2 Description of the iterative variational method

The model uses an iterative procedure in order to minimise $\delta\mathscr{L}$, akin to the one from Pringle et al. (2012). Initially, a first guess of the initial perturbation: $\mathbf{u}^{(0)}(t=0) = \mathbf{u_0}^{(0)}$, $\mathbf{u_p}^{(0)}(t=0) = \mathbf{u_{p0}}^{(0)}$, is made. One can use random values for the initial perturbation but at the cost of a larger number of iterations needed, around 50 in our case, to obtain convergence. The iteration process is as follows:

- The flow direct variables, $\mathbf{u}, \mathbf{u_p}$, p and N, are integrated forward until a target time $t = T$ is reached, using Equations (2.15)-(2.18) to obtain $\mathbf{u}^{(0)}(T)$ and $\mathbf{u_p}^{(0)}(T)$, $\Upsilon^{(0)}(T)$ and ${\Upsilon_p}^{(0)}(T)$ are then computed using conditions (3.13).

- $\Upsilon^{(0)}$ and ${\Upsilon_p}^{(0)}$ are integrated backward using the adjoint system of Equations (3.9)- (3.12) to find $\Upsilon^{(0)}(0)$ and ${\Upsilon_p}^{(0)}(0)$.

- The conditions left after the previous steps are:

$$\frac{\partial\mathscr{L}}{\partial\mathbf{u_0}} = -\lambda\mathbf{u_0} - \Upsilon \, , \quad \frac{\partial\mathscr{L}}{\partial\mathbf{u_{p0}}} = -\lambda_p\mathbf{u_{p0}} - \Upsilon_p \, . \tag{3.15}$$

  Both $\frac{\partial\mathscr{L}}{\partial\mathbf{u_0}}$ and $\frac{\partial\mathscr{L}}{\partial\mathbf{u_{p0}}}$ are supposed to be equal to 0. It is a priori not true with this method, as it does not give an exact solution, there will be the residues ε and ε_p left. The initial perturbations for the next iteration are given as:

$$\mathbf{u}^{(1)}(0) = \mathbf{u}^{(0)}(0) + \varepsilon(\lambda\mathbf{u}^{(0)} - \Upsilon^{(0)}(0)) \tag{3.16}$$

  for the fluid velocity, and:

$$\mathbf{u_p}^{(1)}(0) = \mathbf{u_p}^{(0)}(0) + \varepsilon_p(\lambda_p\mathbf{u_p}^{(0)}(0) - {\Upsilon_p}^{(0)}(0)) \, , \tag{3.17}$$

  for the particle velocity. The aim of the process being the iterative decrease of ε. The previous steps are repeated until convergence is reached, numerically it corresponds to both ε and ε_p becoming smaller than an arbitrary value chosen as threshold.

3.3 Description of the code and numerical method

The code is derived from a standard DNS code, (Willis, 2017), and is the same as the one described in Section 2.5. This code has been modified to account for the presence of particles with the model from Klinkenberg et al. (2011).

3.3.1 Time-stepping scheme

The equations for the evolution of the fluid velocity, $\mathbf{u}$ and particles velocity, $\mathbf{u_p}$ are of the form:

$$\partial_t \mathbf{u} = \mathbf{L}\mathbf{u} + \mathbf{N}\,, \tag{3.18}$$

$$\partial_t \mathbf{u_p} = \mathbf{N_p}\,. \tag{3.19}$$

Where $\mathbf{L}$ is a linear operator (the Laplacian in our case) and $\mathbf{N}\,/\,\mathbf{N_p}$ the advective and Stokes terms for Equations (3.18) and (3.19) respectively, which cannot directly be expressed as a function of $\mathbf{u}$ or $\mathbf{u_p}$. Temporal discretisation is done through a second-order predictor-corrector scheme.

The predictor equation for the fluid velocity between the timesteps q and $q+1$ is given below:

$$\mathbf{u}_1^{q+1} = \mathbf{u}^q - \Delta t\left(c\nabla^2\mathbf{u}_1^{q+1} + (1-c)\nabla^2\mathbf{u}^q + \mathbf{N}^q\right)\,, \tag{3.20}$$

where c is the implicitness, the scheme is of second order for $c = 0.5$. However, the value recommended by Willis (2017) is $c = 0.51$. Even though for this value of c the scheme is only first order; the error margin is small enough that the accuracy is almost as good as a second order scheme while improving the stability of the numerical computation. The corrector step is iterated from the step j to $j+1$, yielding:

$$\mathbf{u}_{j+1}^{q+1} = \mathbf{u}^q - \Delta t\left(c\nabla^2\mathbf{u}_j^{q+1} + (1-c)\nabla^2\mathbf{u}^q\,, + c\mathbf{N}_j^{q+1} + (1-c)\mathbf{N}^q\right)\,, \tag{3.21}$$

the operation is iterated until convergence is achieved, i.e. when $\mathbf{u}_{j+1}^{q+1} - \mathbf{u}_j^{q+1}$ is below the threshold. In our case he threshold is fixed to 10^{-5}. A similar process is used for the particle velocity. Without diffusion, the equations are reduced to:

$$\mathbf{u_p}_1^{q+1} = \mathbf{u_p}^q + \Delta t\,\mathbf{N_p}^q\,, \tag{3.22}$$

for the predictor operation, and

$$\mathbf{u_p}_{j+1}^{q+1} = \mathbf{u_p}^q - \Delta t\left(c\mathbf{N_p}_j^{q+1} + (1-c)\mathbf{N_p}^q\right)\,, \tag{3.23}$$

for the correction operation.

The numerical method uses one equation to describe the motion of both $\mathbf{u}$ and $\mathbf{u_p}$ at each radial point, such that the set of equations can be written as a matrix problem of the form:

$$\frac{\mathbf{f}^{q+1}}{\Delta t} = \mathbf{A}\mathbf{f}^{q} + \mathbf{B} \, . \tag{3.24}$$

Matrices $\mathbf{A}$ and $\mathbf{B}$ are of dimension $(N_r \times N_r)$ with N_r, the number of points in the radial direction and $\mathbf{f} = (u_r, u_\theta, u_z, u_{pr}, u_{p\theta}, u_{pz})$. $\mathbf{A}$ is constant and do not need to be calculated at every time step. The pressure is calculated using the Poisson equation: $\nabla^2 p = \nabla u^{q+1}$.

The time used from now on corresponds to the numerical time of the code (Willis, 2017); it is equal to $t = r_0/U_{cl}$ where r_0 is the pipe radius and U_{cl} is the centreline velocity of the steady Hagen-Poiseuille flow.

3.3.2 Spatial discretisation method

The spatial discretisation is done using a fourth order implicit finite difference scheme in the radial direction, and with Fourier transforms in the azimuthal and streamwise direction. The variable is represented as: $f(r,t,z) = \sum_{k,m} \hat{f}(r) a_{km} e^{i(\alpha k z + m_0 m \theta)}$. The code uses a single index in order to simplify the variables storage. Values for $m < 0$ are inferred from the conjugate symmetric property and do not need to be calculated. In the radial direction, the mesh is composed of N_r points distributed unevenly at the roots of the N_r first Chebyshev polynomials for $r \in [0,1]$. The points are defined by:

$$r_l = \cos\left(\frac{2l-1}{2N_r}\pi\right) , \quad l = 1, ..., N_r \, . \tag{3.25}$$

As a result, the mesh points are clustered both towards the wall and to a lesser extent the centre of the pipe. Derivatives are calculated using Taylor expansions for a given function f at a radius, r_i:

$$f(r) = \sum_{0}^{2l} \frac{(r-r_i)^l}{l!} f^{(l)}(r_i) \, , \tag{3.26}$$

using l neighbouring points on each side of r_i gives us $2l$ equations. These Taylor expansions can also be expressed in a matrix format:

$$\mathbf{f} = \mathbf{A}\mathbf{df} \quad \Rightarrow \quad \mathbf{df} = \mathbf{A}^{-1}\mathbf{f} \, , \tag{3.27}$$

with $\mathbf{f} = [f(r_{-l}) \cdot f(r_l)]^T$ and $\mathbf{df} = [f(r_i) f'(r_i) \cdot f^{(2l)}(r_i)]^T$, $\mathbf{A}$ is the weight matrix, the superscript corresponds to the order of the derivative.

$\mathbf{f}$ is known and $\mathbf{A}^{-1}$ can be computed to find the values of the derivatives. Taylor expansions are used for integrations as well, integrating Equation (3.26) gives:

$$\int_r f(r)\mathrm{d}r = (r-r_i)f(r_i) + \frac{(r-r_i)^2}{2!}f^{'}(r_i) + \frac{(r-r_i)^3}{3!}f^{(2)}(r_i) + ... = \sum_0^{2l} \frac{(r-r_i)^{l+1}}{(l+1)!}f^{(l)}(r_i)\ . \quad (3.28)$$

Similarly, using l neighbouring points around r_i one can obtain a solvable matrix system from which is derived $\int_r f(r)\mathrm{d}r$. In practice, since the mesh is fixed, the values of the weight matrices only need to be computed once at the beginning of the run. Derivations and integrations are less accurate close to the wall when there are fewer than l points between r_i and the wall. The problem is partially alleviated with the use of Chebyshev roots for radial points as they are clustered towards the wall.

3.3.3 Modifications of the code for the solid phase

The code used in this chapter has been modified in order to model the solid phase through a fully Eulerian framework. In a first time is added a set of equations for the particles velocity, $\mathbf{u_p}$, for both the standard and adjoint problem (corresponding to Equation (2.16) for the direct problem and Equation (3.10) for the adjoint problem respectively). Numerically this corresponds to a modification of the matrices A and B mentioned in Equation (3.24).

Initial and boundary conditions for the particle velocity need to be added to the code as well. The initial fluid velocity is obtained from a previous saved state. The code has been modified to allow for the particle velocity to either be taken for a previous saved state or be randomised, although the first option will reach convergence after a lower amount of iteration.

In the single phase LDNS, the convergence of the problem by ensuring that $\frac{\partial \mathscr{L}}{\partial \mathbf{u_0}}$ tends towards 0. An additional condition is added to the problem in the case of the particulate flow: $\frac{\partial \mathscr{L}}{\partial \mathbf{u_{p0}}} = 0$. The iterative process of the code (mentioned in Section 3.2) had to be modified to compute and ensure the decay of both $\frac{\partial \mathscr{L}}{\partial \mathbf{u_0}}$ and $\frac{\partial \mathscr{L}}{\partial \mathbf{u_{p0}}}$.

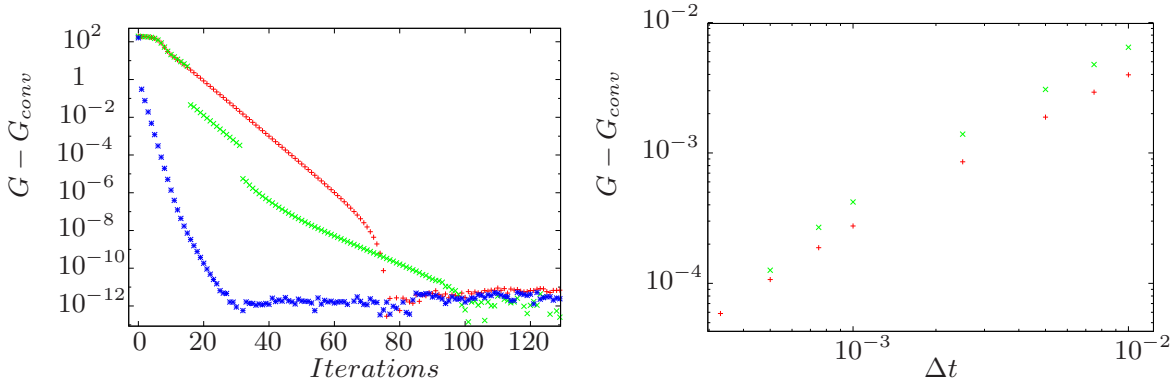

Figure 3.1: $S = 10^{-3}$, $f = 0.1$ **Left:** Transient growth as a function of the number in the n^{th} optimisation process with $Re = 1000$. Single phase flow (blue), fixed T (red), varying T (blue). **Right:** Transient growth as a function of Δt, $Re = 1000$ (red), $Re = 2000$ (green).

3.4 Convergence of the LDNS code

Figure 3.1 shows the difference between the values for maximum transient growth obtained for a given number of iterations, and the fully converged value after 500 iterations. The transient growth is shown to converge as the process is iterated; the jumps are due to the periodic recalibrating of the optimal time of growth. After approximately a hundred iterations the growth has converged and subsequent variations are due to noise, probably due to limitations in machine precision. Convergence is faster for a single phase flow, with 30 iterations necessary before the code reaches machine precision; this number is more than doubled for particulate flows. However, the error quickly becomes smaller to the other incertitude source due to the number of points in the radial direction and the timestep. In this case, the initial perturbation was random, convergence can also be accelerated by choosing a perturbation closer to the optimal perturbation expected. The maximum growth converges as the timestep decreases as illustrated in Figure 3.1; the rate of convergence is a power law. The timestep chosen in this chapter is, unless otherwise specified, $dt = 10^{-3}$ to obtain a good compromise between accuracy and computational cost.

3.5 Monotonic stability

As mentioned in section 1.8, a flow is defined as monotonically stable if the amplitude of all perturbations decreases at all time. This is a much more stringent condition than the global stability studied in Chapter 2.

Knowing the value of the optimal growth as $T \to 0$ is sufficient to determine whether the flow is monotonically stable. In order to study monotonic stability numerically, we fix a small value

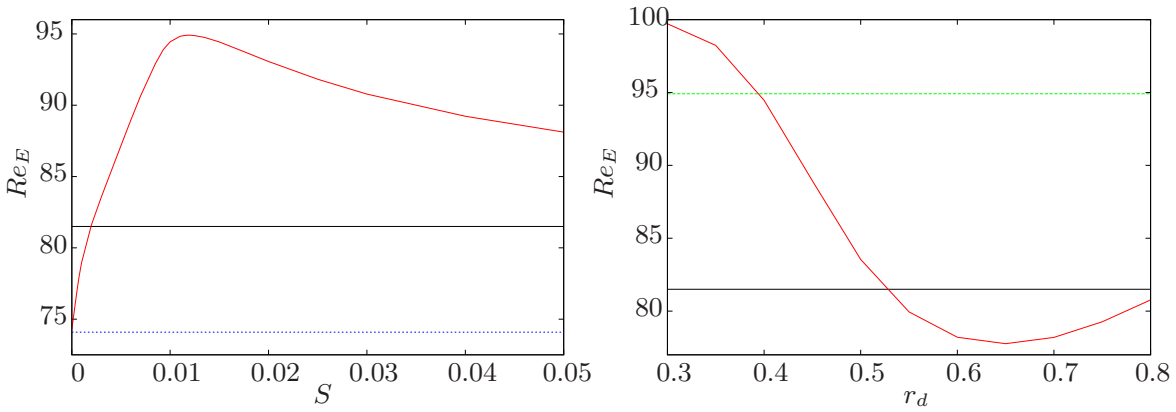

Figure 3.2: Critical Reynolds number for the monotonic stability Re_E (red), $f = 0.1$. **Left:** As a function of S, uniform particle distribution. **Right:** For a Gaussian particle distribution, as a function of its position r_d, $S = 1.2^{-2}$, $\sigma = 0.1$. The black line represents the single phase pipe flow Re_{E_f}, the blue, Re_{E_f} normalised by $1+f = 0.1$, $Re_{E_{f2}}$. The green line represents the value of Re_E for a uniform particle distribution with $S = 1.2 \times 10^{-2}$.

of $T = 10^{-2}$ and look for the critical Reynolds monotonic stability, Re_E, keeping the solid phase parameters f and S (as well as r_d and σ for nonhomogeneous particle distributions) with a bisection method. Figure 3.2 shows the value of the critical Reynolds for monotonic stability in the case of uniform (left side) and Gaussian particle distribution (right side). As mentioned in Section 2.7.6, the addition of particles modifies the average density of the flow, it is then sensible to normalise the value of the single phase flow critical Reynolds by $1+f$. The value of Re_E for a particulate flow with a uniform particle distribution is higher than Re_{E_f} when $S > 10^{-3}$. Re_E is also always higher than $Re_{E_{f2}}$ and $Re_E(S \to 0) \to Re_{E_{f2}}$. Re_E shows a sharp increase with S, followed by a slower decrease after a peak around $S = 1.2 \times 10^{-2}$. The amplitude of the effect, of the order of 10%, is significant. In the case of the Gaussian distribution, Re_E is below the value found for the uniform particle distribution (with the same value of S) except when $r_d < 0.40$. The lowest value is reached when $r_d = 0.65$, coincidently it corresponds to the Segré-Silberberg radius (Segre and Silberberg, 1962), and is very close to the radius for which the linear instability was the strongest (Section 2.8.3). This is another point in favour of the argument that particle effect on the flow is strongest around this radius. The solid phase has, for an homogeneous particle distribution, a tendency to increase the monotonic Reynolds number of the flow. On the other hand, arranging particles in a Gaussian distribution tends to decrease it, especially when particles are concentrated at a radius close to the Segré-Silberberg radius. Overall, the effect of particles on the monotonic stability is fairly limited, even with for Gaussian particle distributions that have been shown to lead to linear instability.

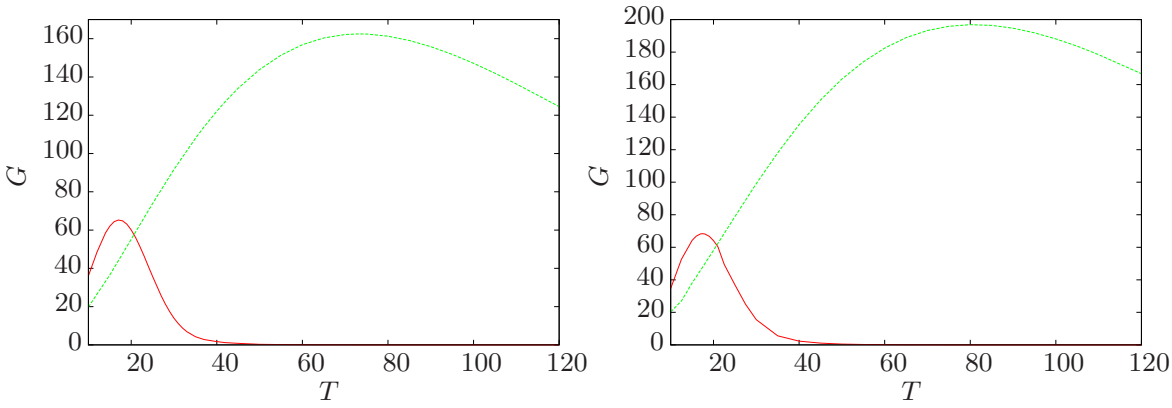

Figure 3.3: Maximal growth as a function of the time of optimisation, T with $Re = 1500$. **Left:** Single phase flow. **Right:** Uniform particle distribution $S = 10^{-3}$, $f = 0.1$. Wavenumbers $(\alpha, m) = (1, 1)$ in red, $(\alpha, m) = (0, 1)$ in green.

3.6 Transient growth for uniform particle distributions

First, we consider the case of uniform particle distribution where, as seen in Chapter 2, the particulate flow is linearly stable for all values of Re, S and f.

3.6.1 Envelope of maximum transient growth

The value of the maximum transient growth depends on the chosen time, while we are mostly interested in T_{max}; it is interesting to see how G depends on T. Figure 3.3 shows an example of the maximum energy growth as a function of the chosen time T for a single phase flow, and a particulate flow with homogeneous distribution. The two modes that have the largest growth, $(\alpha, m) = (0, 1)$ and $(\alpha, m) = (1, 1)$, are plotted independently. The curves for single phase and particulate flow are of similar shape, where there are two competing mechanisms for growth.

- For small times, below $T = 20$ in the single phase flow case, and $T = 22.5$ for the particulate flow, the mode producing the most growth is $(\alpha, m) = (1, 1)$. The growth produced by this mode quickly decreases as the time increases.
- For larger values of T, the mode producing the most growth is $(\alpha, m) = (0, 1)$.

$(\alpha, m) = (0, 1)$ is the mode that yields the largest transient growth when optimising for T, with a value approximately three times larger than the largest growth when $(\alpha, m) = (1, 1)$, for both single phase flows and particulate flows with homogeneous particle distributions. T will be optimised when studying the transient growth in the following sections.

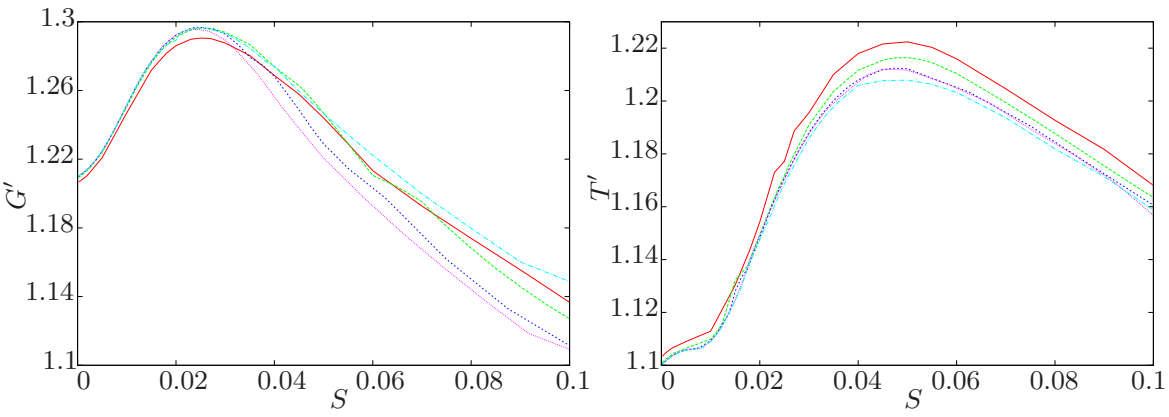

Figure 3.4: Ratio of growth between particulate and single phase flow as a function of S for $f = 0.1$. **Left:** Maximal transient growth. **Right:** Ratio of the time of maximum growth. $Re = 500$ (red), 1000 (green), 2000 (dotted blue), 3000 (purple), 5000 (blue dashed).

3.6.2 Impact of the Reynolds and dimensionless relaxation time on the transient growth

In this section the effect of the Reynolds number Re and the dimensionless relaxation time S on the maximum transient growth is studied, f is kept constant at $f = 0.1$. In order to illustrate the effect of particles on the flow, we define the ratio between the growth for the particulate flow with a given set of parameters and the single phase flow with the same Reynolds number: $G' = \frac{G_p(Re,S,f)}{G_f(Re)}$, where both G_p and G_f are maximised over T. A similar ratio is chosen between the optimal time for particulate and single phase flow, $T' = \frac{T_p(Re,S,f)}{T_f(Re)}$. Figure 3.4 shows the growth ratio as well as the ratio of optimal times as a function of S for different values of the Reynolds number. One can see that the addition of particles increases the transient growth for all values of S, the growth is also delayed since the ratio between optimal times is always larger than 1. The maximum growth as a function of S peaks at intermediate values of S, similar to the linear eigenvalue. From now on the growth peak is defined as G'_{peak}, and the dimensionless relaxation time associated S_G.

The limit $S \to 0$ corresponds to small particles with a small relaxation time. The particles behave like passive tracers, they closely follow the fluid and do not affect the behaviour of the flow. However, as particles which much heavier than the fluid are added to the flow, its average density is increased by a factor $(1+f)$. Consequently, the effective Reynolds number of the flow becomes $Re' = Re(1+f)$. This implies that if the growth rate of a particulate flow obtained at a Reynolds number Re is equal to the growth rate of the single phase flow at a Reynolds number $Re' = (1+f)Re$, both exhibits identical properties, the difference in growth rate only being due to a difference in average density. This is what occurs when $S \to 0$, as illustrated in Table 2.6 which shows examples of growth rates for particulate flows and single phases flow with Reynolds numbers Re and $(1+f)Re$ respectively, for $S = 10^{-6}$. The normalised difference is consistently below 5×10^{-4}. In this case, the addition of particles makes the flow less stable, but only through the modification of the average density of the fluid. Klinkenberg

et al. (2011) found a similar result in the case of the plane Poiseuille flow. It has also been found that the normalised leading eigenvalue stays almost constant for S in the range 10^{-7} to 10^{-4}.

When $S \to 0$, $G' \approx 1.2$. The difference between single phase and particulate flows is due, in this case, to the modification of the average density of the flow caused by the particles. Let us remind that the limit $S \to 0$ corresponds to small particles with a small relaxation time. The particles behave like passive tracers and do not directly affect the behaviour of the flow. However, the average density of the particulate flow is $(1+f)$ time the density of the single phase flow. Then, the effective Reynolds number of the particulate flow is $Re' = 1.1Re$. Moreover, in the single phase pipe flow the growth G_f is proportional to Re^2, therefore:

$$G_p(Re, S \to 0) = G_f(Re') = G_f((1+f)Re) = (1+f)^2 G_f(Re) \,. \tag{3.29}$$

In the case $f = 0.1$; it implies a a value of the growth ratio $G' = 1.1^2 = 1.21$, as observed in Figure 3.4. As S increases the ratio G' seems to decreases towards 1, although convergence is not yet achieved for $S = 10^{-1}$; the highest value considered. In the limit of $S \to \infty$, the particles are so heavy that particles and flow are effectively decoupled so the particles have no effect on the flow. A similar effect was observed for the linear stability analysis in Section 2.7.6. The Reynolds number has little incidence on G', as the curves have a very similar shape when Re is varied. The curves of Figure 3.4 have, for all Re considered, a peak for approximately the same relaxation time, $S \simeq 2.5 \times 10^{-2}$.

Moreover, the value of G'_{peak} shows little change as Re varies with $1.290 \leqslant G'_{peak} \leqslant 1.297$. G'_{peak} is almost constant over the Reynolds number and the transient growth for single phase flow $G_f(Re)$ scales with Re^2; it follows that the transient growth for particulate flows optimised over S $G_p(S_G)$ also scales with Re^2.

The right graph of Figure 3.4 shows the ratio of T' as a function of S. The growth is delayed for particulate flows compared to single phase for any value of S and Re considered. As $S \to 0$, the time for which the growth is maximised increases by 10% compared to the single phase flow. This corresponds to the time for the modified Reynolds number $Re' = (1+f)Re$ since, as discussed in the previous section, the time for maximum growth increases linearly with Re. Similarly, a peak for the time ratio T'_{peak} occurs at a dimensionless relaxation time S_T. The time ratio decreases as S continues to increase in a similar fashion as the ratio of growth. S_T is significantly higher than S_G, in addition there also are more variations between cases. The peak value of S is centred around $S_T = 5 \times 10^{-2}$. T'_{peak} vary between 1.205 and 1.22 depending on Re. The ratio becomes slightly lower as the Reynolds number increases but the effect size is small with only a 1.5% difference for an increase of the Re by an order of magnitude.

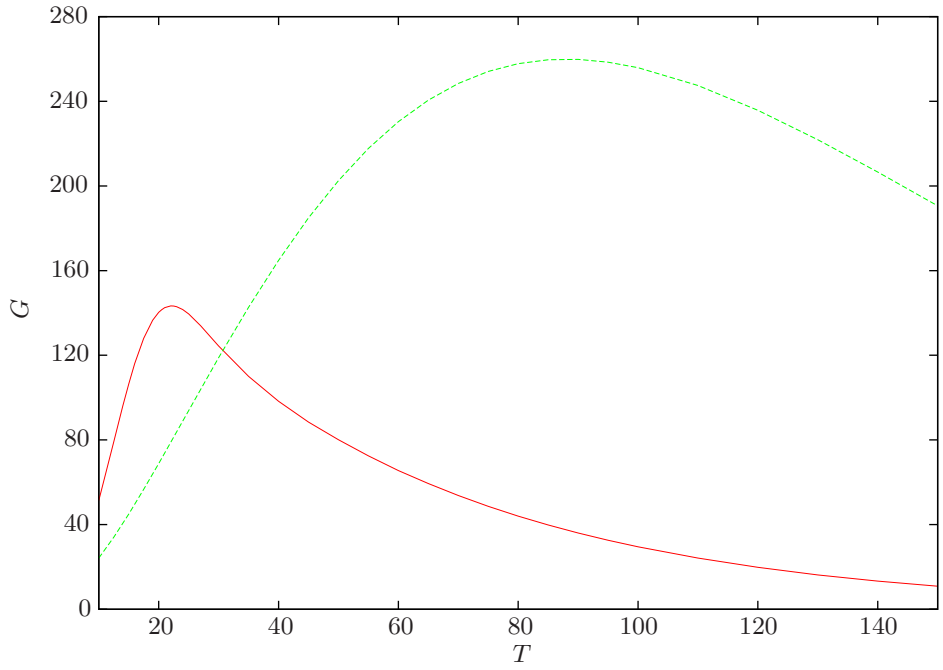

Figure 3.5: Maximal growth as a function of the time of optimisation T for a Gaussian particle distribution with $Re = 1500$, $S = 10^{-3}$, $f = 0.1$, $r_d = 0.65$ and $\sigma = 0.104$. The red line corresponds to the wavenumbers $(\alpha, m) = (1, 1)$, the green line to $(\alpha, m) = (0, 1)$.

3.7 Transient growth with nonhomogeneous particle distribution

We have seen in Chapter 2 that allowing for a nonhomogeneous distribution of the particles dramatically increases the effect of the solid phase on the flow linear stability. This is also the case for the transient growth. The mechanisms producing transient growth for single phase and particulate flows are the same, even when considering nonhomogeneous distribution, however, the amplitude of transient growth can be much stronger as particles are non-uniformly distributed. Figure 3.5 shows the envelope for a Gaussian particles distribution with $r_d = 0.65$ and $\sigma = 0.104$. For these parameters the flow is still linearly stable. The behaviour is the same for the pure fluid and homogeneous distribution cases as illustrated in Figure 3.3, but the transition to streamwise independent modes is slightly delayed, occurring at $T = 25$. The overall shape of the growth is the same for a Gaussian distribution as one for the homogeneous particle distribution as illustrated in Figure 3.6. The maximum growth increases as particles get more concentrated, corresponding to a decrease of σ. However, the effect is significantly more pronounced even for smaller values of σ, for $\sigma = 0.10$ the smallest value considered, and $r_d = 0.7$, $G'_{peak} = 2.30$. The growth ratio as $S \to 0$ is no longer equivalent to the ratio for Re'. However G' still tends towards 1 for very large values of S.

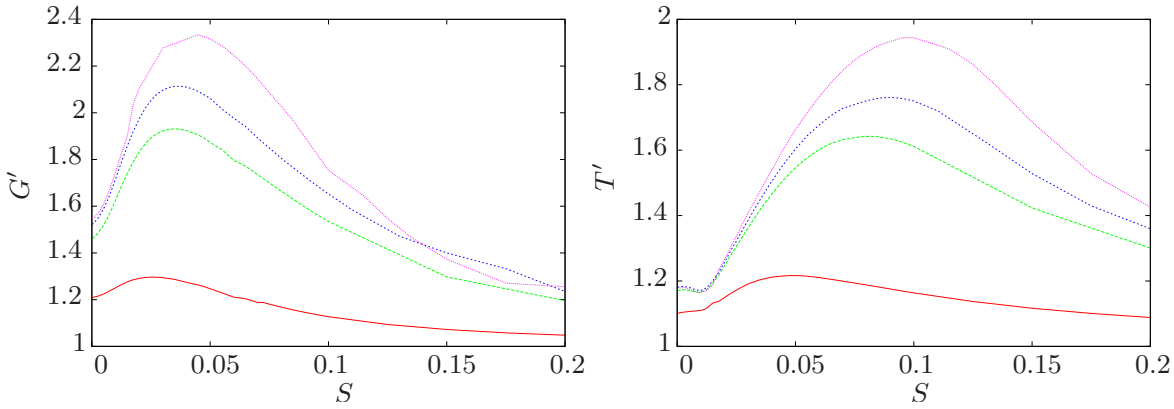

Figure 3.6: Ratio of growth between particulate and single phase flow as a function of S for $f = 0.1$ and $Re = 1000$ in the case of a Gaussian particle distribution centred around $r_d = 0.7$. **Left:** Maximal transient growth. **Right:** Ratio of the time of maximum growth. Uniform distribution (red), $\sigma = 0.15$ (green), $\sigma = 0.12$ (dotted blue), $\sigma = 0.10$ (purple).

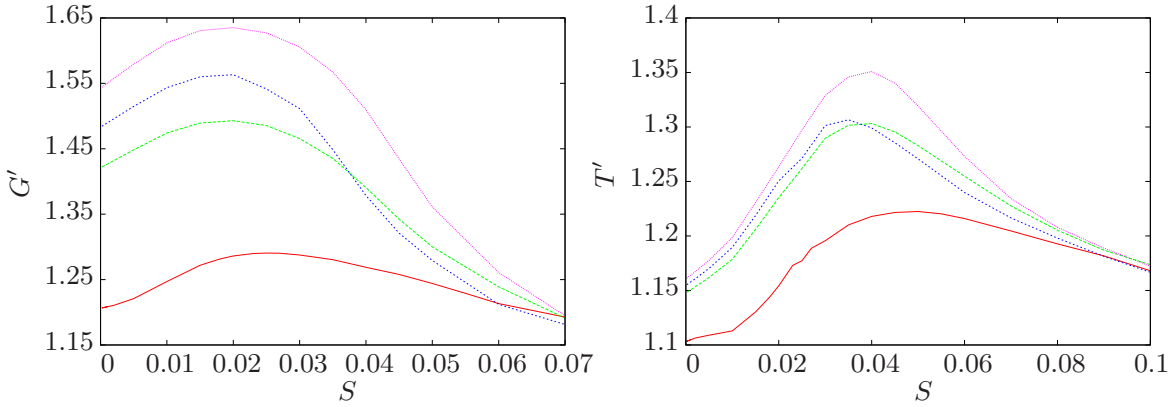

Figure 3.7: Ratio of growth between particulate and single phase flow as a function of S for $f = 0.1$ and $Re = 500$ in the case of a Gaussian particle distribution centred around $r_d = 0.3$. **Left:** Maximal transient growth. **Right:** Ratio of the time of maximum growth. Uniform distribution (red), $\sigma = 0.15$ (green), $\sigma = 0.12$ (dotted blue), $\sigma = 0.10$ (purple).

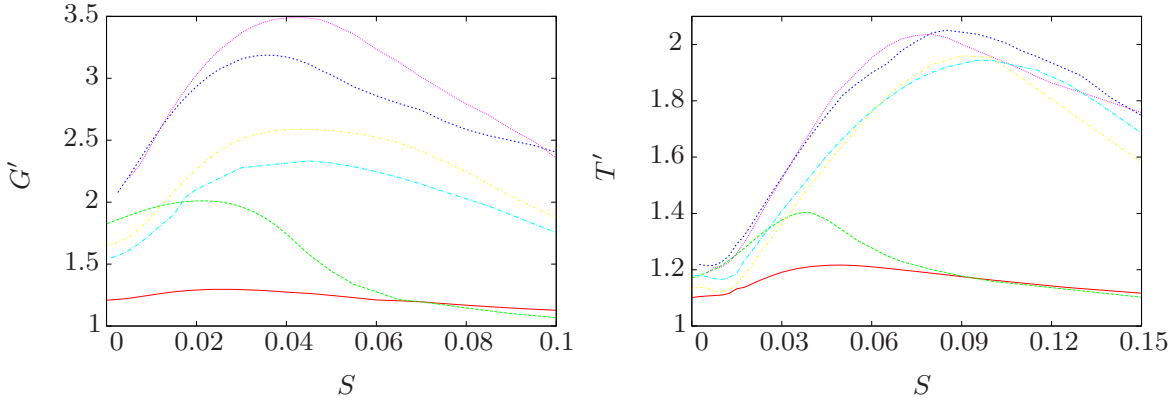

Figure 3.8: Ratio of growth between particulate and single phase flow as a function of S for $f = 0.1$ and $Re = 1000$ in the case of a Gaussian particle distribution with $\sigma = 0.1$. **Left:** Maximal transient growth. **Right:** Ratio of the time of maximum growth. Uniform distribution (red), $r_d = 0.3$ (green), $r_d = 0.5$ (dotted blue), $r_d = 0.6$ (purple), $r_d = 0.7$ (dashed blue), $r_d = 0.8$ (yellow).

This is similar to the linear stability analysis when the effect of particles is higher as they are more concentrated. The position of the peak shifts to a larger S in the nonhomogeneous distribution case, around $S_G \simeq 3.5 \times 10^{-2}$.

The time at which the optimal growth occurs is delayed for Gaussian particle distributions as well. The effect is stronger for Gaussian distributions and the ratio of times further increases as the standard deviation σ decreases. The time ratio as $S \to 0$ is no longer equivalent to the time ratio for Re', as opposed to the homogeneous particle distribution. The maximum growth occurs at larger values of S compared to homogeneous particle distribution, with $8.25 \times 10^{-2} \leqslant S_T \leqslant 9 \times 10^{-2}$. Changing the standard deviation σ of the particles distribution affected the growth ratio but has little effect on the value of S_G and S_T. The behaviour as a function of S in general is not affected.

The position of the preferential radius of particles has a strong impact on both G' and T'. Figure 3.7 shows the ratio of growth for several values of σ with $r_d = 0.3$, with all other parameters being kept equal to those of Figure 3.6. The effect of σ is similar to the one observed for $r_d = 0.3$. On the other hand, the values of G'_{peak}, T'_{peak} as well as S_G and S_T are quite different. For example, when $\sigma = 0.10$, the peak of the ratio of the transient growth is $G'_{peak}(r_d = 0.3) = 1.65$ (compared to $G'_{peak}(r_d = 0.7) = 2.3$) and the time ratio is $T'_{peak}(r_d = 0.3) = 1.35$ (compared to $T'_{peak}(r_d = 0.7) = 1.8$). The position of the particle distribution is therefore a critical parameter when considering the flow transient growth. Although the effect is weaker, both G'_{peak} and T'_{peak} are significantly stronger for the Gaussian particle distribution with $r_d = 0.3$ than for a homogeneous particle distribution. The dimensionless relaxation time at which these peaks occur is smaller for Gaussian distribution when $r_d = 0.30$ in comparison to homogeneous distribution, this is the opposite effect to what occurred for $r_d = 0.70$. For $r_d = 0.3$, $S_G = 2 \times 10^{-2}$ (while $S_G = 2.5 \times 10^{-2}$ with an homogeneous particle distribution) and $S_T \simeq 4 \times 10^{-2}$ (compared to $S_T = 5 \times 10^{-2}$ for an homogeneous particle distribution).

More values of r_d are considered in Figure 3.8, which gives the ratios of transient growth as a function of S for several particle distribution radius r_d, with $Re = 1000$ and $\sigma = 0.1$. The value of the growth peak goes from $G'_{peak} = 1.95$ for $r_d = 0.3$, to $G'_{peak} = 3.50$ for $r_d = 0.6$. The time of maximum growth are likewise dependent on r_d. The effect of particles on the flow is the highest for $r_d = 0.5 - 0.6$ both for the ratio of maximum growth and the ratio of time as shown in Figure 3.8. Again, the effect of the particle is maximal relatively close to the Segré-Silberberg radius. Both S_G and S_T are, for $r_d = 0.3$, smaller than their counterpart in the case of a uniform particle distribution, but larger for all the others values of r_d studied. There does not seem to be a consistent effect between r_d and either G'_{peak} or T'_{peak}.

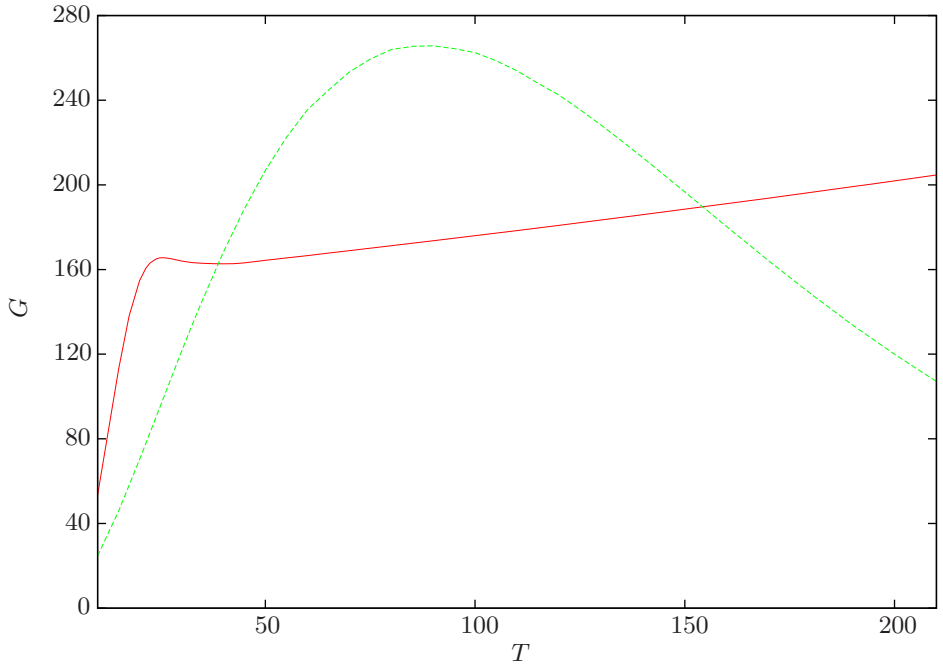

Figure 3.9: Maximal growth as a function of the time of optimisation T, for a Gaussian particle distribution with $Re = 1500$, $r_d = 0.65$, $S = 10^{-3}$, $f = 0.1$ and $\sigma = 0.094$. The red line illustrates the mode $(\alpha, m) = (1, 1)$, the green line $(\alpha, m) = (0, 1)$.

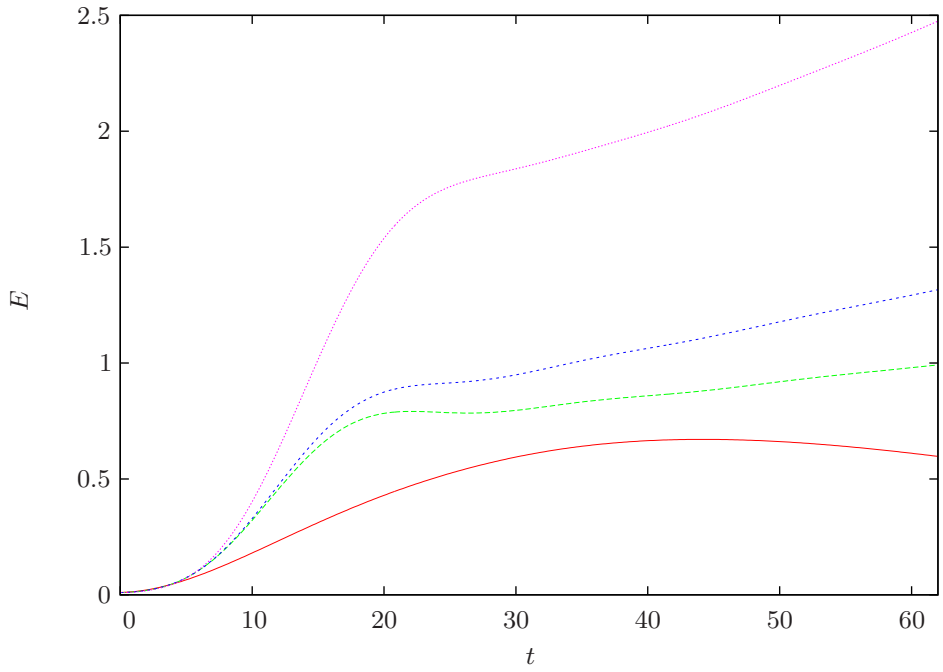

Figure 3.10: Energy growth as a function of time for several Reynolds numbers, $Re = 750$ (red), $Re = 915$ (green), $Re = 1000$ (blue), $Re = 1500$ (purple). $S = 10^{-3}$, $f = 0.1$, $r_d = 0.70$, $\sigma = 0.09$.

3.8 Linear instability

Since the particulate pipe flow can become linearly unstable, the LDNS simulation should show a different behaviour, with no maximum growth for a finite time. Figure 3.9 shows the envelope for a linearly unstable case, the behaviour for the mode $(\alpha, m) = (0, 1)$ is similar to what is observed in Figure 3.5, where the flow is linearly stable. The mode $(\alpha, m) = (1, 1)$, however, continues to increase indefinitely with the target time after its peak until it exceeds the value from the other mode at $T = 150$. This observation is consistent with the fact that in the single phase flow case, the optimal transient growth is produced by a streamwise-independent mode with $m = 1$ (Section 2.8). The evolution of a perturbation as a function of the time t (distinct from the target time T) is shown in Figure 3.10. The flow is stable for $Re = 750$ and unstable for the other values. The energy growth in unstable case exhibits a first peak corresponding to the single phase transient growth followed by a momentary decrease and a exponential growth for larger times. The time for the transient growth peak is smaller in the unstable cases.

Overall, the effect of particle on the transient growth in the case of Gaussian particle distributions is quite pronounced. The growth is more than doubled at the peak in the region $r_d = 0.5 - 0.8$, where particle tend to cluster (as discussed in Sections 1.9.2 and 2.9) for a distribution of $\sigma = 0.1$, which is not highly clustered. This stronger growth could lead to new mechanisms for turbulence formation. Another question we will seek to answer in the next section is the role of particle on the shape of the optimal perturbation, as it could give insight on different ways to trigger turbulence in particulate flows.

3.9 Velocity modes topology

In this chapter, the impact of the particles on the transient growth has been studied. We now consider how the addition of particle affects the profile of the optimal initial perturbation. In the figures of this section, the heat map represents the streamwise velocity while the arrows are proportional to the spanwise velocity, normalised by its maximum.

3.9.1 Single phase flow

The velocity contours of the perturbations are very different depending on whether the dominant mode is $(\alpha, m) = (1, 1)$ or $(\alpha, m) = (0, 1)$. Figures 3.11a and 3.12a are velocity contours of the pipe section. Figure 3.11a are the contours of the initial perturbation and Figure 3.12a shows the peak velocity contours, as the growth is optimised for $T = 14$. Figure 3.11a shows two symmetric rolls in

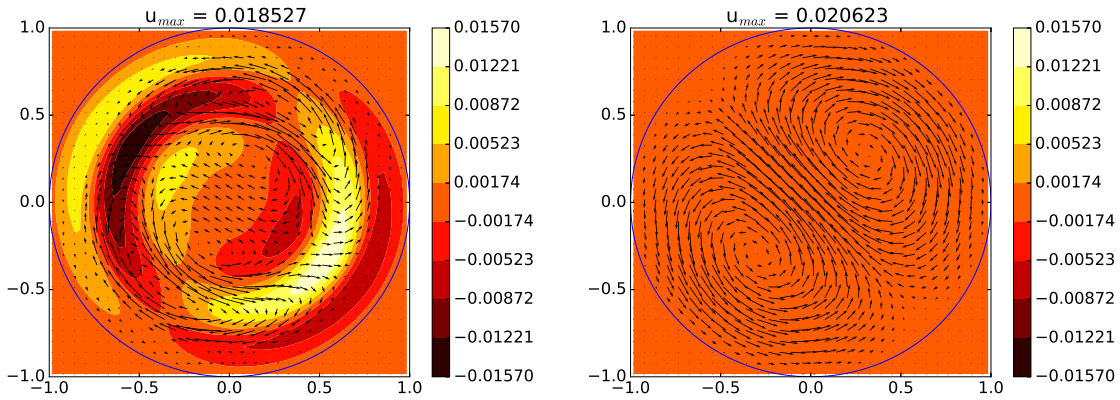

(a) Target time $T = 14$. Mode $(\alpha, m) = (1, 1)$. (b) Target time $T = 90$. Mode $(\alpha, m) = (0, 1)$.

Figure 3.11: Velocity contours u_0 of the optimal perturbation for single phase flows, $Re = 1500$.

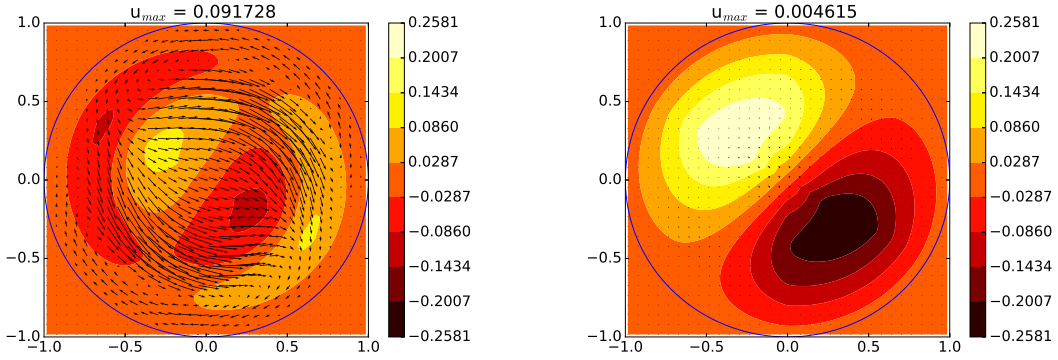

(a) Target time $T = 14$. Mode $(\alpha, m) = (1, 1)$. (b) Target time $T = 90$. Mode $(\alpha, m) = (0, 1)$.

Figure 3.12: Peak velocity contours u_T of single phase flow, $Re = 1500$.

the spanwise direction. The streamwise velocity has a peak of the form of an antisymmetric annulus between $r = 0.5$ and $r = 0.7$, with a change of direction between the peak and the rest of the half plane. There is also a reflectional symmetry with regards to the centre due to the fact that $m = 1$. Streamwise and spanwise velocities are of the same order of magnitude in both cases.

For a perturbation with a larger target time T, the streamwise independent mode is dominating as illustrated in Figure 3.11b. The velocity contours at $T = T_{peak}$ for $T = 90$ (Figure 3.12b) and the optimal perturbation for the same time (Figure 3.11b) have an identical shape. However, for the optimal perturbation, the spanwise velocity is much stronger than the streamwise velocity, while in the case of the peak velocity, the streamwise velocity is an order of magnitude larger than the other components. In the spanwise direction, there are two rolls that are distinctive of the usual single phase transient growth (Bergström, 1993). The spanwise velocity is more uniformly distributed than for $T = 14$. The streamwise velocity is also more than two orders of magnitude smaller than the spanwise velocity for $T = 90$, when the mode $(\alpha, m) = (1, 1)$ is dominant, whereas they are of the same order of magnitude when $T = 14$.

3.9.2 Particulate flows

For small values of the dimensionless relaxation time and uniform particle distribution, both the initial perturbation of the fluid and particles are almost identical, as illustrated in Figures 3.13a-3.13f. The topology of the streamwise velocity distribution is shaped as two antisymmetric spirals with the spanwise velocity concentrated over these same rolls. For the lower target time $T = 14$ when the mode $(\alpha = 1, m = 1)$ is dominant; both the optimal initial velocity contours and peak velocity contours, as seen in Figures 3.13a-3.13f, are quantitatively equal to the one observed for single phase flow (see Figures 3.11a and 3.12a). In the second case where $T = 90$; the mode $(\alpha = 0, m = 1)$ is dominant. The velocity contours between single phase (illustrated in Figure 3.11b) and particulate flows (Figures 3.13c and 3.13d) are identical both in shape and in values. The contours have the same characteristics in the case of Gaussian distributed particles, with the exception of the velocity of the initial optimal perturbations concentrated where the particles are distributed (see Figures 3.14a-3.14d). The fluid and particles peak velocities are very similar to the peak velocity of the single phase flow due to the fact that for a small dimensionless relaxation time, fluid and particles are strongly coupled.

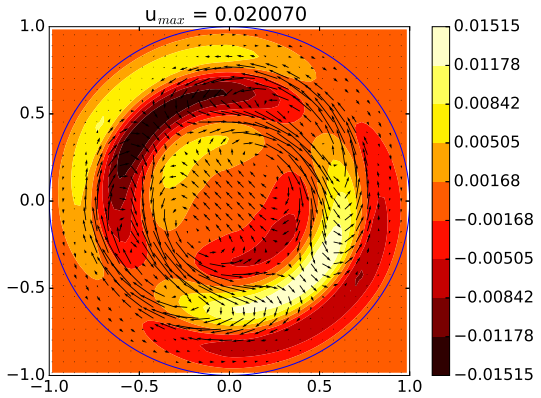

(a) Target time $T = 14$. Optimal perturbation $\mathbf{u_0}$.

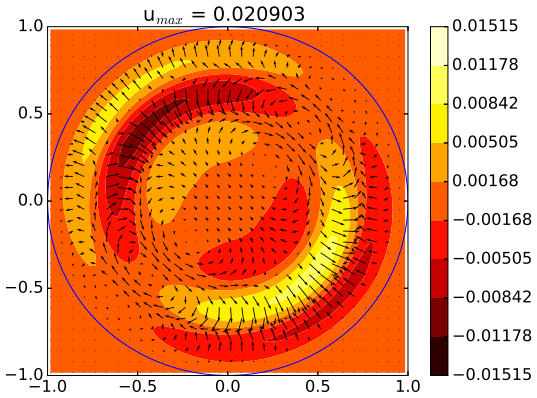

(b) Target time $T = 14$. Optimal perturbation $\mathbf{u_{p0}}$.

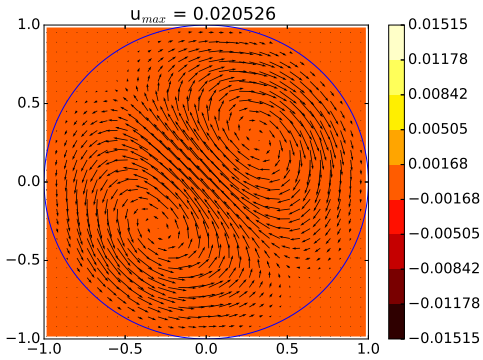

(c) Target time $T = 90$. Optimal perturbation $\mathbf{u_0}$.

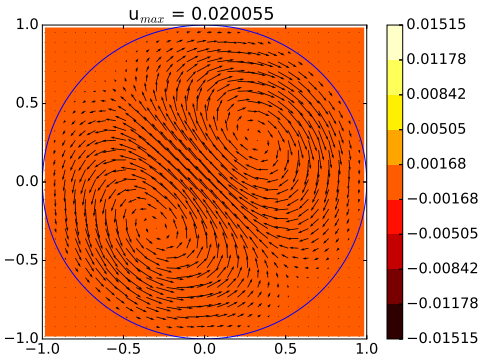

(d) Target time $T = 90$. Optimal perturbation $\mathbf{u_{p0}}$.

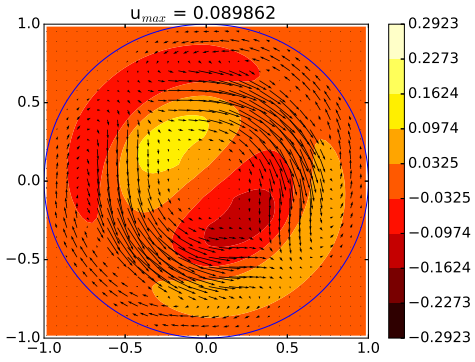

(e) Target time $T = 14$. Peak velocity $\mathbf{u_{pT}}$.

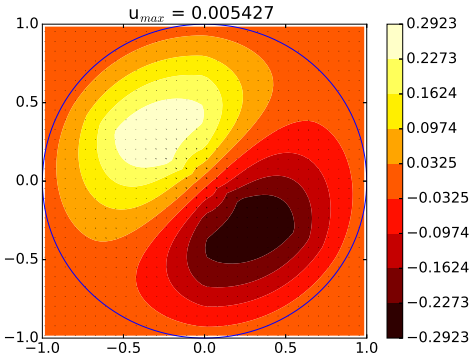

(f) Target time $T = 90$. Peak velocity $\mathbf{u_{pT}}$.

Figure 3.13: Homogeneous particle distribution, $Re = 1500$, $f = 0.1$, $S = 10^{-3}$, the dominant mode is $(\alpha, m) = (1, 1)$ in the case $T = 14$ and $(\alpha, m) = (0, 1)$ for $T = 90$.

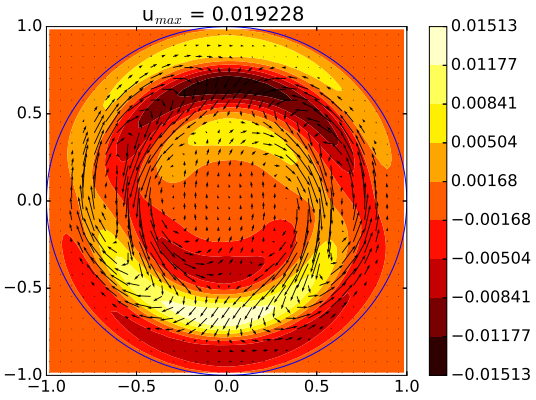

(a) Target time $T = 14$. Optimal perturbation $\mathbf{u_0}$.

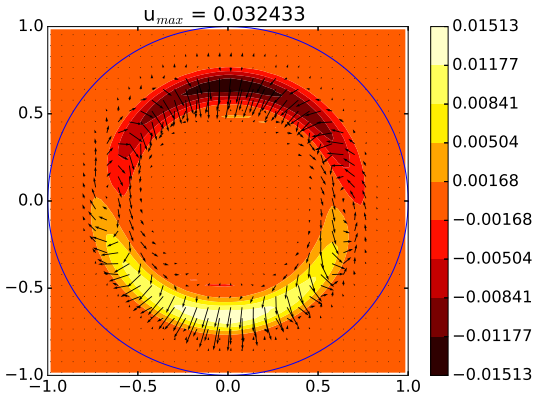

(b) Target time $T = 14$. Optimal perturbation $\mathbf{u_{p0}}$.

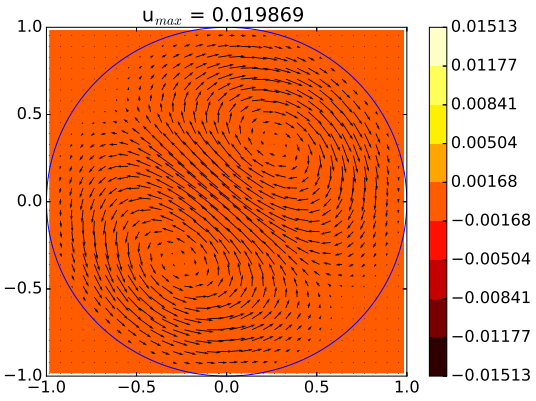

(c) Target time $T = 90$. Optimal perturbation $\mathbf{u_0}$.

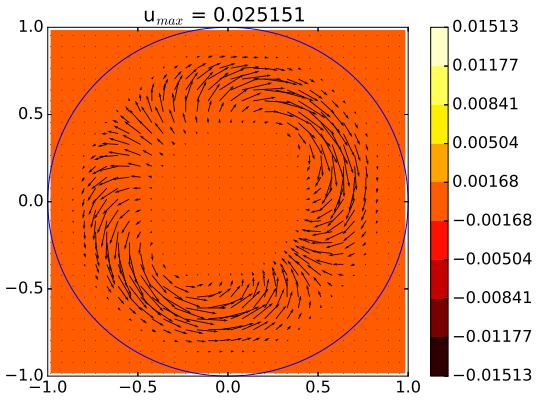

(d) Target time $T = 90$. Optimal perturbation $\mathbf{u_{p0}}$.

Figure 3.14: Optimal perturbation contours of a particulate flow with a Gaussian particle distribution, $Re = 1500$, $f = 0.1$, $S = 10^{-3}$, $r_d = 0.65$, $\sigma = 0.104$.

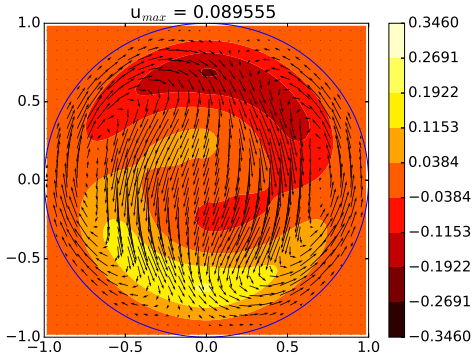

(a) Target time $T = 14$. Peak velocity $\mathbf{u_{pT}}$.

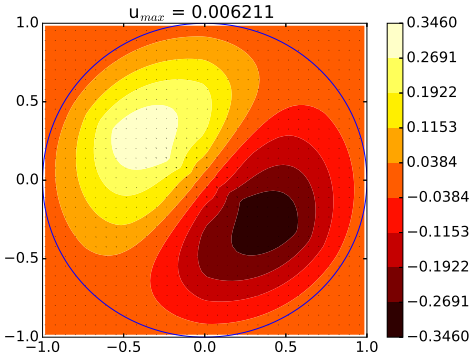

(b) Target time $T = 90$. Peak velocity $\mathbf{u_{pT}}$.

Figure 3.15: Peak velocity contours of a particulate flow with a Gaussian particle distribution, $Re = 1500$, $f = 0.1$, $S = 10^{-3}$, $r_d = 0.65$, $\sigma = 0.104$.

3.10 Conclusion

The addition of particles does impact the maximum transient growth as well as the maximum time of growth. In a similar fashion to the effect on the growth rate in the linear stability analysis seen in Chapter 2, homogeneous particles distributions only have a limited effect, with a below 30% increase in all cases even for a fairly large value of $f = 0.1$. The effect of S on the transient growth is slightly different than that of the growth rate in the linear stability analysis; the transient growth is increased regardless of the values of S, while some values of S have a stabilising effect on the flow in the linear stability analysis. The behaviour for transient growth and linear stability analysis, however, is similar for $S \to 0$, where the growth is increased proportionally to $1 + f$, and $S \to \infty$ where the addition of particles has no effect on the flow. There is a value of the dimensionless relaxation time for which the growth is maximised. Not only is this relaxation time independent of the Reynolds number, the ratio of growths optimised over S, G'_{peak}, is constant as Re varies. This implies that the particulate flow scales as Re^2 as it does for the single phase flow. In the case of Gaussian particle distributions, the addition of particles can lead to an increase of the transient growth by more than 200% for some values of S, r_d and σ. The transient growth increases monotonically as σ decreases. As for r_d, the effect of the solid phase on the transient growth is weaker when the particles are close to the wall or at the pipe centre, and strongest at the intermediate region ($r_d = 0.6 - 0.7$). This region seems to play a key role both in the laminar state and in the flow stability. Indeed, neutrally buoyant particles tend to cluster in this region in the laminar state (Matas et al., 2004b; Segre and Silberberg, 1962) and particulate pipe flows have been found linearly unstable when particles of intermediate size are added in that region (Rouquier et al., 2018). Several elements, such as the most for which the growth is the same for single phase and particulate flows being the same, and velocity contours staying quite similar as particles are added, seems to indicate that the addition of particles does not change the mechanisms by which the transient growth occurs. The work done in this Chapter does not answer the questions of how the particles increase the flow transient growth and whether the actual pathway to turbulence is indeed sensitive to particles being present in that region. Further work including fully nonlinear effects is necessary in order to better understand the the role of the solid phase in the transition to turbulence. Although it is likely that the addition of particles leads to new mechanisms for transition to turbulence (Boronin, 2012; Matas et al., 2003), the fully Eulerian model did not highlight any new mechanism.

Chapter 4

Point particle model

The work presented in Chapters 2 and 3 used an Eulerian framework to model the solid phase. As mentioned in Section 1.4, while using an Eulerian mesh for this purpose has advantages, it also comes with limitations. Particles are not considered individually, limiting the study of particle behaviour and particle-particle dynamics in particular. The fully Eulerian model also relies on the continuous assumption for the solid phase, which breaks down if the distance between particles is too large, for example in cases where a small number of large particles are considered. In this chapter a second theoretical model is implemented, using particle Lagrangian tracking to model the solid phase while the fluid phase is modelled with an Eulerian framework. The main objectives of this Chapter are to describe the code used and give some examples of how its applications. As the code is still under construction, there are limitations as to what is doable, but interesting results where obtained nonetheless. There are several avenues for future work with minor adjustments to the code.

4.1 Description of the model and governing equations

4.1.1 Equations of motion of the fluid

Our model needs two types of equations of motion, one in the Eulerian frame of reference for the fluid and the second in the Lagrangian frame of reference for the particles. The fluid velocity is described by the standard Navier-Stokes equations; conservation of mass and conservation of momentum respectively yield:

$$\nabla \cdot \mathbf{u} = 0 \,, \tag{4.1}$$

$$\rho_f \left(\frac{\partial \mathbf{u}}{\partial t} + (\mathbf{u} \cdot \nabla)\mathbf{u} \right) = -\nabla p + \mu \nabla^2 \mathbf{u} + \mathbf{F_0} \,. \tag{4.2}$$

where ρ_f is the fluid density, $\mathbf{u}$ is the fluid velocity, p is the pressure, μ is the dynamic viscosity and $\mathbf{F_0}$, the external forces. In our case $\mathbf{F_0}$ represents the effect of the particles on the fluid. The problem is non-dimensionalised using the steady flow centreline velocity U_0 and the pipe radius r_0. The dimensionless form of Equations (4.1) and (4.2) is:

$$\nabla \cdot \mathbf{u} = 0 \,, \tag{4.3}$$

$$\partial_t \mathbf{u} = -\mathbf{u} \cdot \nabla \mathbf{u} - \nabla p + \frac{1}{Re} \nabla^2 \mathbf{u} + \mathbf{F} \,, \tag{4.4}$$

with $Re = \frac{U_0 r_0}{\nu}$ as the flow Reynolds number.

4.1.2 Particle-fluid interaction

The motion of the particles is described using a point particle approximation (see Section 1.5.1). Each particle is modelled as a single point, the particles still have a theoretical mass and radius. The equation of motion for the particles is adapted from the equation of motion for a rigid sphere given by Maxey and Riley (1983). The velocity $\mathbf{u_p}$ of a particle is described by the following equation:

$$m_p \frac{d\mathbf{u_p}}{dt} = m_f \frac{D\mathbf{u}}{dt} + (m_p - m_f)\mathbf{g} - \frac{m_f}{2}\frac{d}{dt}\left(\mathbf{u_p} - \mathbf{u} - \frac{a^2}{10}\nabla^2\mathbf{u}\right) - 6\pi a\mu\left(\mathbf{u_p} - \mathbf{u} - \frac{a^2}{6}\nabla^2\mathbf{u}\right), \tag{4.5}$$

with $\mathbf{u}$ being the fluid velocity at the particle position, a the particle radius, μ the fluid viscosity, m_p and $m_f = \frac{4}{3}\pi\frac{a^3}{\rho_f}$ are the particle mass and the fluid mass for an equivalent volume.

Equation (4.5) can be non-dimensionalised using the steady flow velocity U_0 and the pipe radius r_0. The dimensionless numbers thus obtained are: $a' = \frac{a}{r_0}$, the particle to pipe radius ratio; $\rho_t = \frac{\rho_f}{\rho_p}$, the fluid to particle density ratio; $Re = \frac{U_0 r_0}{\nu}$, the Reynolds number; $S = \frac{2}{9}\frac{a^2}{\rho_t}$, the dimensionless relaxation time and $Ri = \frac{g r_0}{U_0^2}\mathbf{g}$, the Richardson number with g the standard gravity and $\mathbf{g}$ its direction. The dimensionless form of Equation (4.5) is given as:

$$\frac{d\mathbf{u_p}}{dt} = \rho_t \frac{D\mathbf{u}}{dt} + (1-\rho_t)Ri - \frac{\rho_t}{2}\frac{d}{dt}\left(\mathbf{u_p} - \mathbf{u} - \frac{a^2}{10}\nabla^2\mathbf{u}\right) - \frac{1}{SRe}\left(\mathbf{u_p} - \mathbf{u} - \frac{a^2}{6}\nabla^2\mathbf{u}\right). \tag{4.6}$$

The details of the non-dimensionalisation of the problem are given in Appendix B.1. There are several points of note, Equation (4.6) illustrates that the force applied by the fluid on the particles is partially driven by the velocity difference between a particle and the surrounding fluid. Moreover, all the terms of the equations are dependent on the ratio between fluid and particle densities ρ_t, as S is proportional to ρ_t as well. The behaviour of the particles is therefore mainly driven by velocity and density difference between fluid and particles, as well as particle size.

4.1.3 Detection of particle-particle collisions

As the point particle model is only valid for small solid fraction, one could consider neglecting the collisions between particles, this is the choice done in Squires and Eaton (1991). However, as particles have a tendency to cluster in both laminar (Segre and Silberberg, 1962) and turbulent flows (Eaton and Fessler, 1994). This clustering can lead particle local concentrations an order of magnitude larger than the flow average, as observed in Matas et al. (2004b) for laminar flows and Sardina et al.

(2012) in the case of fully turbulent flows. In this case the expected rate of collisions should be much higher than for homogeneously distributed particles and is less likely to have a negligible effect on the flow. Our code still allows for the possibility of neglecting particle-particle interactions if the particle volume concentration is low enough. The distance d between two particles of radii a_i and a_j whose coordinates are (r_i, θ_i, z_i) and (r_j, θ_j, z_j) is given (in cylindrical coordinates) by:

$$d = \left(r_i^2 + r_j^2 - 2\, r_i\, r_j \cos(\theta_j - \theta_i) + (z_j - z_i)^2\right)^{1/2} - (a_i + a_j)\,. \tag{4.7}$$

Two methods have been implemented to detect collisions. A first, simpler method, is to compare the position of each particle to the others at each time step to check for collision. However, it can miss some of the collisions, especially for small and fast particles. The accuracy of the method is increased by checking the distance for several sub-time steps, at the cost of an higher number of necessary computations.

The second method uses a trajectory equation (Yamamoto et al., 2001) in order to obtain a function describing an approximation of the evolution of a particle position between t and $t + dt$, assuming that the particle velocity is constant during the interval, such that

$$\mathbf{x}_i(\tau) = \mathbf{x}_i(t) + \tau\, u_{p_i}\,, \tag{4.8}$$

where $\mathbf{x_i}(\tau)$ is the position of the particle i at a time τ, and $\mathbf{u_{p_i}}$ its velocity at a time t. One can then express the evolution of the distance between two particles i and j, between t and $t + dt$:

$$\begin{aligned} d(\tau) \;= \Big(& r_i^2 + 2\, r_i\, u_{pri}\,\tau + u_{pri}^2\,\tau^2 + r_j^2 + 2\, r_j\, u_{prj}\,\tau + u_{prj}^2\,\tau^2 \\ & - 2\,(r_i + u_{pri}\,\tau)(r_j + u_{prj}\,\tau)\cos(\theta_i + u_{p\theta i}\,\tau - \theta_j - u_{p\theta i}\,\tau) \\ & + (z_j + u_{pzj}\,\tau - z_i - u_{pzi}\,\tau)^2 \Big)^{1/2} - (a_i + a_j)\,. \end{aligned} \tag{4.9}$$

A collision between two particles occurs at any τ that is a root of the function $d(\tau)$. There is, however, no simple way to solve this equation due to the presence of the cosine term. This issue is resolved in our code by converting the problem to Cartesian coordinates where the equation for $d(\tau)$ is a second order polynomial whose roots can easily be found. The better suited detection method depends on the particles velocities, their radii and the code timestep. If $u_p \Delta t \ll a$, checking particles position at $t + dt$ is sufficient, otherwise using a trajectory equation is necessary to ensure no collision is missed.

4.1.4 Processing of particle-particle collisions

One can bypass the issue of particle-particle collisions by adding a fictitious repulsive force, as mentioned in Section 1.5.2. While, for the repulsive force used, for example, in (Glowinski et al., 1999) model, the addition of this force only require a simple modification of the model that does not require additional steps to process collisions, it is a non physical way of solving the problem. In this work, rather than utilising a fictitious force, a hard-particle model of collisions is used to process particle-particle collisions and compute the resulting velocity changes, as described in Section 1.6. The hard-particle model assumes the conservation of momentum through a inelastic collision between two particles i and j. The collision is described using the conservation of linear momentum for each particle,

$$m_i(\mathbf{u_i}^+ - \mathbf{u_i}^-) = \mathbf{J} \quad \Rightarrow \quad \mathbf{u}_i^+ = \mathbf{u_i}^- + \frac{\mathbf{J}}{m_i}\,, \tag{4.10}$$

$$m_j(\mathbf{u_j}^+ - \mathbf{u_j}^-) = -\mathbf{J} \quad \Rightarrow \quad \mathbf{u}_j^+ = \mathbf{u_j}^- - \frac{\mathbf{J}}{m_j}\,, \tag{4.11}$$

where $\mathbf{J}$ is the impulse of momentum acting on particle i due to collision with particle j; $\mathbf{u}$ is the particles velocity, with the superscripts $+/-$ indicating if the value of the variable is after or before the collision respectively. $\mathbf{J}$ can be written as:

$$\mathbf{J} = m'(1+\varepsilon_N)\big((\mathbf{u_i}^- - \mathbf{u_j}^-)\cdot\hat{\mathbf{n}}\big)\hat{\mathbf{n}} + \frac{2}{7}m'(1+\varepsilon_S)\big((\mathbf{u_i}^- - \mathbf{u_j}^-)\cdot\hat{\mathbf{s}}\big)\hat{\mathbf{s}}\,, \tag{4.12}$$

with m' representing the effective mass so that: $\frac{1}{m'} = \frac{1}{m_i} + \frac{1}{m_j}$. ε_N is the coefficient of restitution, bounded between 0 for a completely inelastic collision, and 1 for a perfectly elastic collision. ε_S is the tangential coefficient of restitution, where $\varepsilon_S = [-1, 1]$; $\varepsilon_S = -1$ corresponds to a frictionless collision, $\varepsilon_S = 1$ to a perfectly elastic one, the case $\varepsilon_S = 0$ corresponds the no-slip case. The hard-particle collision model is also used for wall-particle collisions. In this specific case $\mathbf{u_j}^- = 0$, $m' = m_i$ and $\hat{\mathbf{n}} = \hat{\mathbf{r}}$. A more elaborate collision model, the soft-particle approximation (described in Section 1.6) could be implemented into the code with minor modifications. Another point to keep in mind is that collisions in the hard-particle model are considered to be instantaneous, consequently it can only handle binary particles collisions. This is a limiting factor in the limit of dense suspensions. However, as point particle models do not model the flow around the particles nor take into account more complex particles-particles interactions such as agglomeration and sedimentation, the‘ collision model used is unlikely to be the bottleneck with regards to the particle volume fraction.

4.2 Details on the numerical method

The code used in our work is a modified version of Willis (2017), a Lagrangian tracking procedure has been implemented for the solid phase. The original code has already been described in Section 3.3. Therefore, in this section, the primary focus is on the modifications made to account for the addition of solid phase to the flow.

4.2.1 Initial particles conditions

The initial position of the particles should have little effect for a sufficiently long pipe, or for large timescales as the particles tend to converge to consistent distribution (Matas et al., 2004b; Tritton, 1988). The effect can still be significant for short timescales. Six possible initial configurations are considered for the initial particle distribution in each direction:

- Fully randomised particle distribution.
- Uniform particle distribution in the entire pipe length.
- Uniform particle distribution between two bounds.
- Gaussian particle distribution centred at r_d of a standard deviation σ.
- Initial particle state retrieved from a previous run.

Since the set of possible particle positions is continuous in a Lagrangian framework, the distributions considered cannot be exactly evenly distributed. Therefore, in all cases except for the fixed value case, the particles initial distribution is defined in probabilistic terms using the inbuilt Fortran random number generator. For example, considering an "uniform" distribution, each particle has a uniform probability of being anywhere in the pipe, it does not necessarily lead to the distribution of the particles to homogeneous. Consequently, the distribution will have deviations compared to the ideal case, resulting in differences in initial distribution from one run to another even if all parameters are kept identical, the issue is especially relevant for low numbers of particles, this effect is illustrated in Section 4.2.7. This is not an issue, as the ideal case does not accurately represent realistic distributions, indeed a particle distribution with some variation is closer to real cases. Still, having particles initial distributions conserved between runs allows for direct comparisons, studying a particular dynamic or the effect of a parameter. This is why the possibility of using the particle distribution from a previous run has been implemented in the code. This allows us to consider a variety of cases; for example, particles distributed at a fixed streamwise position z and evenly distributed in the section, simulating how particles are often injected in experiments (Matas et al., 2004b). Likewise, a homogeneous

particle distribution in the streamwise and azimuthal distribution, with a nonhomogeneous distribution in the radial direction is closer to what is found in the developed particulate pipe flow (Matas et al., 2004b; Saffman, 1965). Although the particles are treated as points in our model, they still possess a theoretical radius, so that once the initial positions are determined for all particles, the program needs to check for overlap between particles, in the case where there is an overlap between two particles, one of them is given a new random position. As for the initial velocity of the particles, it is set to be either equal to the fluid velocity, or randomised with only a fixed total kinetic energy per particle. It is also possible to use the particles initial velocities from a previous run.

4.2.2 Neighbouring cell: Coarse Contact Detection

The collision detection algorithm need to check for potential collisions for all particles. While can detect collisions using a brute force method that checks for every possible collision between any two particles, however, the number of operations per timestep required scales with N_p^2. Therefore, the brute force method is not practical when considering a large number of particles. The efficiency can be improved by checking for possible collisions of a given particle only with particles that are in their neighbourhood (Vance et al., 2006; Yamamoto et al., 2001; Zhao et al., 2006). The domain is separated into cells, following which the collision detection can be made independently for each cell. The numerical program has a mesh used for the Eulerian formulation of the fluid. We can either use it directly or multiples of it depending on the cell size wanted, as the detection algorithm is optimised when the cell size is around twice the particles radius (Mio et al., 2005). If correctly optimised, a neighbouring cell method scales as $O(n)$ (Muth et al., 2007). This scaling has not yet be verified in the present code, this is one of the expected next step in future works.

4.2.3 Eulerian to Lagrangian interpolation

Since our model is a point particle model with a Lagrangian framework for the particles and an Eulerian one for the fluid, the values of the fluid velocity need to be interpolated from the neighbouring nodes to the particles position and vice-versa, in order to compute fluid-particle interactions. The accuracy of the interpolation depends on the distance between the mesh point and the interpolated point as well as the interpolation method used. Two such methods have been implemented: *trilinear interpolation* and *spline interpolation*.

Trilinear interpolation

A trilinear interpolation is a first order method interpolating the value of function **f** at a point whose coordinates are (x,y,z), from the closest neighbouring points $(x_0,y_0,z_0,x_1,y_1,z_1)$. In three

dimensions, the linear interpolation of a function $\mathbf{f}$ is:

$$\begin{aligned}\mathbf{f}(x,y,z) =&(1-z_d)(1-y_d)(1-x_d)\mathbf{f}(x_0,y_0,z_0)+(1-z_d)(1-y_d)x_d\mathbf{f}(x_1,y_0,z_0)+\\&(1-z_d)y_d(1-x_d)\mathbf{f}(x_0,y_1,z_0)+(1-z_d)y_d x_d\mathbf{f}(x_1,y_1,z_0)+\\&z_d(1-y_d)(1-x_d)\mathbf{f}(x_0,y_0,z_1)+z_d(1-y_d)x_d\mathbf{f}(x_1,y_0,z_1)+\\&z_d y_d(1-x_d)\mathbf{f}(x_0,y_1,z_1)+z_d y_d x_d\mathbf{f}(x_1,y_1,z_1)\,,\end{aligned} \tag{4.13}$$

where $x_d = \frac{x-x_0}{x_1-x_0}$, $y_d = \frac{y-y_0}{y_1-y_0}$ and $z_d = \frac{z-z_0}{z_1-z_0}$.

Although linear interpolation methods have been used in the literature (Sardina et al., 2012), they have a rather low accuracy, requiring a very fine grid to keep a satisfying uncertainty margin.

Spline interpolation

A second, more accurate method implemented in our code uses spline polynomials. In our case, a spline of order 3, with n_s points in each direction, are used for the interpolation. For a discrete function $\mathbf{f}$ whose value is known at the points x_k with $k \in [1,\ 2n]$, the coefficients a_k, b_k and c_k that best fit the values of $\mathbf{f}$ given are computed. Assuming a given position x_a where $x_i \leqslant x_a \leqslant x_{i+1}$, $\mathbf{f}$ can then be interpolated as:

$$\mathbf{f}(x_a) = \mathbf{f}(x_i) + a_i(x_a - x_i) + b_i(x_a - x_i)^2 + c_i(x_a - x_i)^3\,. \tag{4.14}$$

Even though the interpolation only uses the closest points, the coefficients a_i, b_i and c_i depend upon all $2n_s$ points, leading to increased accuracy as the number of points used increases. The interpolation methods used here are best suited to smooth functions, but are less reliable in the case of sharp velocity changes.

4.2.4 Lagrangian to Eulerian interpolation

The particle velocity needs to be interpolated to the fluid Eulerian mesh in order to compute the effect of the particles on the fluid phase. In the point particle approximation limit, the particle information is interpolated from a single data point. This severely limits the maximum attainable accuracy. The bluntest way to interpolate from a single point to the Eulerian mesh is to divide the point force equally among all neighbouring points. A weighting function depending on the distance between the mesh point and the particle can be used to improve the accuracy. Our code uses a linear function but more elaborate weighting functions could be implemented later. The function used in the code is, for a force $\mathbf{F}$ which is to be interpolated from a Lagrangian point $\mathbf{X}$ to the eight closest neighbouring Eulerian

mesh points $\mathbf{x_i}$. Thus we have:

$$\mathbf{f_i}(\mathbf{x_i}) = \frac{d_i \mathbf{F_i}}{\sum d_i} \,, \tag{4.15}$$

where $d_i = |\mathbf{x_i} - \mathbf{X_i}|$ is the distance between the particle position and the Eulerian mesh point i. $\sum_{i=1}^{8} \mathbf{f_i} = \mathbf{F_i}$.

4.2.5 Structure of the code

Equation (4.6) gives the acceleration of a particle. It involves a time derivative for both the fluid and particle velocities. Consequently, the numerical form of the evolution of fluid and particle velocity is:

$$\mathbf{u}^{n+1} = \mathbf{f}(\mathbf{u}^n, \mathbf{u_p}^n, \mathbf{u_p}^{n+1}) \quad , \quad \mathbf{u_p}^{n+1} = \mathbf{g}(\mathbf{u_p}^n, \mathbf{u}^n, \mathbf{u}^{n+1}) \,. \tag{4.16}$$

Since both $\mathbf{u}^{n+1}$ and $\mathbf{u_p}^{n+1}$ need information from the step $n+1$, they cannot be computed directly. Instead, an iterative process is used. In a first time, an approximate value of the fluid velocity is computed:

$$\mathbf{u}_{(0)}^{n+1} = \mathbf{f}(\mathbf{u}^n, \mathbf{u_p}^n) \,, \tag{4.17}$$

then the particle velocity is obtained using $\mathbf{u_p}_{(0)}^{n+1}$, and the values from the n^{th} step, giving:

$$\mathbf{u_p}_{(0)}^{n+1} = f_1(\mathbf{u}^n, \mathbf{u_p}^n, \mathbf{u}_{(0)}^{n+1}) \,. \tag{4.18}$$

The value of the fluid velocity is updated using the approximate value:

$$\mathbf{u}_{(1)}^{n+1} = f\left(\mathbf{u}^n, \mathbf{u_p}^n, \mathbf{u_p}_{(0)}^{n+1}\right) \,, \tag{4.19}$$

$\mathbf{u_p}^{n+1}$ is finally updated using $\mathbf{u}_{(1)}^{n+1}$:

$$\mathbf{u_p}_{(1)}^{n+1} = f_1\left(\mathbf{u}^n, \mathbf{u_p}^n, \mathbf{u}_{(1)}^{n+1}\right) \,. \tag{4.20}$$

The process is repeated until values of $\mathbf{u}^{n+1}$ and $\mathbf{u_p}^{n+1}$ converge to the required precision. The precision required for the predictor-corrector operation (described in Section 3.3.1) is 10^{-5}, the same value has been taken for the precision of the convergence. The code can be used for one-way, two-way and four-way coupling, its logic diagram is given in Figure 4.1 for the two last cases. To recall, in a one-way coupling model, the particles are affected by the fluid while the effect of the solid phase on the fluid is neglected. In two-way coupling models fluid and solid phases are fully coupled; both fluid and particles affect each other. Four-way coupling models add particle-particle interactions, in

our case collisions. In the case of the one-way coupling, there are two additional steps compared to the single phase flow simulation; the interpolation from the Eulerian to the Lagrangian mesh and the computation of the particles velocity. Two-way and four-way coupling models require major changes. This is especially true for the four-way coupling case with the management of particle-particle collisions where several steps are needed, it can also be computationally expensive for large particles concentrations when a large number of collisions occurs at each timestep.

4.2.6 Test of the interpolation from Eulerian to Lagrangian meshes

n_s	$(64,12,12)$	$(64,24,24)$	$(64,48,48)$	$(128,48,48)$	$(128,72,72)$
lin	3.7120×10^{-2}	8.6166×10^{-3}	2.0771×10^{-3}	2.4632×10^{-3}	1.9930×10^{-3}
1	2.6070×10^{-2}	6.1284×10^{-3}	1.5549×10^{-3}	1.5556×10^{-3}	1.4968×10^{-3}
2	1.2941×10^{-3}	7.7383×10^{-5}	4.9271×10^{-6}	4.9110×10^{-6}	4.7153×10^{-6}
3	1.8685×10^{-4}	1.0810×10^{-5}	6.9708×10^{-7}	6.5145×10^{-7}	6.5806×10^{-7}
4	1.7308×10^{-4}	1.1684×10^{-5}	8.0029×10^{-7}	7.5850×10^{-7}	7.2488×10^{-7}
5	1.6947×10^{-4}	8.2089×10^{-6}	4.8946×10^{-7}	7.5850×10^{-7}	4.1352×10^{-7}
6	1.5393×10^{-4}	8.4405×10^{-6}	5.6014×10^{-7}	5.1115×10^{-7}	4.8382×10^{-7}

Table 4.1: Average normalised error of the trilinear and spline interpolations of the function $\mathbf{g}(r,\theta,z) = 0.3\cos(z)*(2\cos(r)-\sin(\theta))$ at 1000 random positions for a pipe of length, $L=2\pi$ as a function of the number of interpolation points n_s for Eulerian meshes composed of (N_r,N_t,N_z) points in the radial, azimuthal and streamwise directions respectively.

In order to validate the interpolation method used in this work, the accuracy of the interpolation as a function of the number of grid points of the Eulerian mesh has been tested using a known sinusoidal function. Table 4.1 gives the normalised error from a known sinusoidal function depending on r, θ, and z. The result shows that the accuracy of the interpolation method is dependent on n_s as well as the number of points in the Eulerian mesh. Both are to be expected, as the efficiency of the coefficients computation increases with n_s and the finer the Eulerian mesh, the smaller the average distance between the particle position and the closest Eulerian mesh point. The trilinear interpolation error is between 10^{-3} and 10^{-2} (at the exception of the coarsest mesh). Even the finest mesh has an averaged error larger than 10^{-3}, because it is impractical to use a mesh as fine when considering a longer pipe. Moreover, the error computed here is after a single interpolation, one would expect it to compound with time. Therefore, the trilinear interpolation does not yield accurate enough results for our needs. The spline interpolation method shows a much higher accuracy than the linear interpolation. The error around three orders of magnitude more accurate for $n_s \geqslant 2$. The accuracy of the interpolation increases with n_s but diminishing returns are hit as n_s gets larger than 4. The value $n_s = 4$ is therefore used in

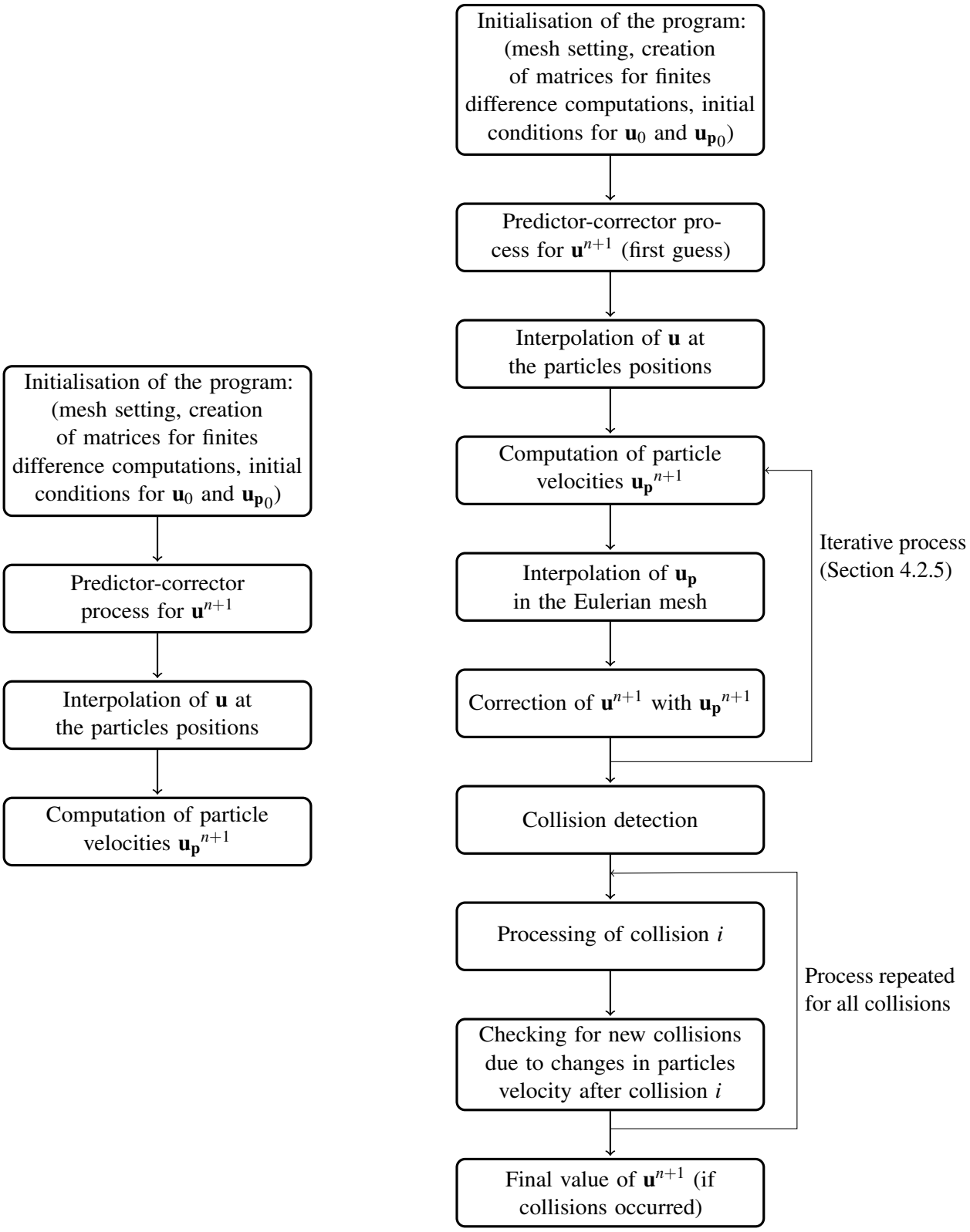

Figure 4.1: Logic diagram of the point particle code for one-way coupling (left) and four-way coupling (right).

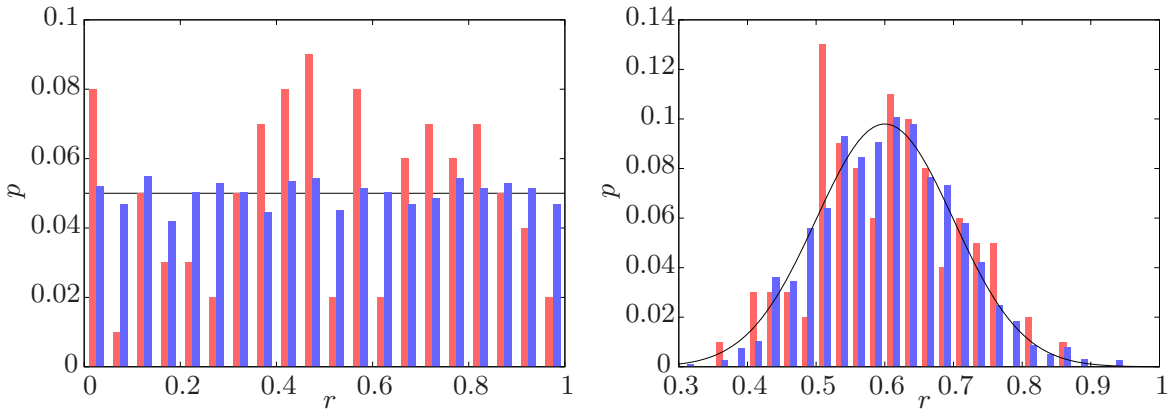

Figure 4.2: Frequency histogram of initial particle distributions with $N_p = 100$ (red) and $N_p = 5000$ (blue), the solid line represents the values in the continuous case for uniform and Gaussian distributions. **Left:** Random uniform probability across the radius. **Right:** Random Gaussian probability centred around $r = 0.6$ with a standard deviation $\sigma = 0.1$.

our numerical simulations unless otherwise specified. As for the effect of the Eulerian mesh density, there is, for the radial direction, little variation between $N_r = 64$ and $N_r = 128$. The normalised error actually is slightly higher for $N_r = 128$ in some cases, indicating that the efficiency of the interpolation in the radial direction reaches diminishing returns for less than 64 points. In the other two directions the accuracy seems to plateau at 48 points, although the pipe length is small in this case. The number of points in the streamwise direction is then a limiting factor as longer pipes are considered. One should also note that the function chosen here is sinusoidal. It is possible that the interpolation error is larger in our flow, especially for turbulent flows where smaller scales are involved.

4.2.7 Initial particle distribution

The initial particle distributions considered in our code (Section 4.2.1) are, for most configurations, statistically defined. Therefore, one should expect differences between runs with theoretical values. It is illustrated in Figure 4.2 which shows the frequency histogram for a uniform and a Gaussian particles initial distributions for $N_p = 100$ and $N_p = 5000$. In both cases, there are deviations; the impact is less pronounced as the number of particles increases and there are still significant variations from the theoretical distributions even for 5000 particles. This needs to be taken into account when interpreting results (with the exception of fully turbulent flows which do not depend on initial conditions).

4.2.8 Range of validity of the model

The range of parameters for which the fully Eulerian model used for the linear stability and linear transient growth analyses has been evoked in Section 2.1. The restrictions of the point particle model are, in comparison, loosened due to several of its characteristics:

- As the point particle model does not rely on an averaging process, there is no lower bound on the number of particles considered, allowing for the study of a small number of larger particles. However, the model is ill-suited to very large number of particles, although it can be done if one is willing to bear the computational cost associated. For example, some of Sardina et al. (2012) runs considered more than 10^6 particles, at a high cost of approximately 200000 core hours per run.

- As particle-particle interactions are taken into account, the dilute regime assumption is not necessary. However, the model still breaks down for a dense regime (volume fraction over 25%) as this model only considers binary collisions, and particle clustering and sedimentation is neglected. Moreover, the flow around the particles is not directly modelled, this can lead to large discrepancies when the particle volume concentration is too high or the particles too large.

- While the point particle approximation breaks down for arbitrarily large particles, it is compatible for a larger particles than the fully Eulerian model. On the other hand, the fully Eulerian model can include Brownian motion, albeit the one studied in Chapter 2 does not, making the fully Eulerian model more suited to extremely small particles.

- Finally, while the model used in Chapters 2 and 3 only considers the Stokes drag, the model used in this chapter also adds the effect the buoyancy, added mass force and effect of the undisturbed flow to the equation of motion.

Overall, while the point particle model breaks down in some conditions, such as very large particles or dense suspensions; it is usable in broader parameter range than the fully Eulerian model.

4.3 Turbulent flow with one-way coupling

Willis' code has been used in Chapter 2 and 3 to test for long term decay rates and transient growth respectively. It has also been used for various works (Budanur and Hof, 2017; Cerbus et al., 2018; Pringle and Kerswell, 2010). Our focus, when verifying the code validity, is therefore going to be on the treatment of the solid phase of the flow.

4.3.1 Particles and fluid cross-correlation

At first, we consider a simplified model in order to test the code, neglecting particle-particle collisions, with either only the Stokes drag force alone, or the combination of the Stokes drag, pressure gradient, added mass force terms with one-way coupling between flow and particles. The pipe length considered is of $L = 20r_0$ (equivalent to 10 diameters). The particles are, initially, uniformly distributed within the pipe. Figure 4.3 shows the velocity of a given particle as well as the interpolated fluid velocity at the particle position. The behaviour of the particles with regards to the flow is influenced by the

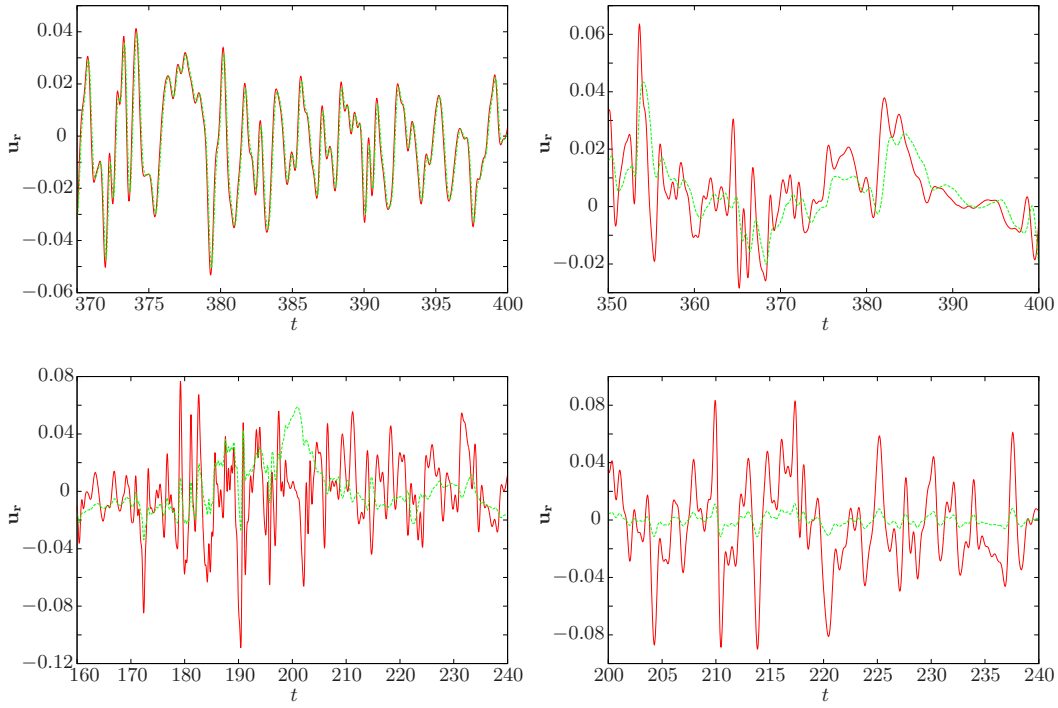

Figure 4.3: Radial velocity as a function of time for a particle (green) and the fluid (red) interpolated at the particle position, with the Stokes drag only. $Re = 3000$, $\rho_t = 1$. **Top left:** $a = 10^{-2}$. **Top right:** $a = 3.5 \times 10^{-2}$. **Bottom left:** $a = 10^{-1}$. **Bottom right:** with Stokes drag, pressure drag and added mass forces, $a = 10^{-2}$.

particle's size as one can expect. A case with small particles is given in the top-left graph of Figure 4.3 with $a = 10^{-2}$. In this case, one can see the particle and fluid velocity are almost identical even as the fluid velocity shows rapid variations. Since we use one-way coupling here, the fluid is not influenced by the particles, implying that the particle closely follows the fluid trajectories, as is expected for small particles (Saffman, 1962). As particles get bigger, they still follow the broad motions of the flow but there is a delay between fluid and particles velocity, as shown in the top right graph of Figure 4.3. The difference between fluid and particles get more pronounced as the timescale associated to the particles increases. The largest particles are illustrated in the bottom-left graph of Figure 4.3. Here the particle and fluid are decoupled; the fluid has little to no influence on the particle behaviour. Comparing top left and bottom right graph of Figure 4.3 which have the same particle size, but the first one only considers the Stokes drag force while the second adds pressure drag and added mass forces. One can observe the effect of the added mass force: it acts as a dampener on particle velocity even for small particles, where the particles follows the fluid velocity variations closely.

Figure 4.3 is an example where only a single particle is considered. In order to obtain a more complete picture one can analyse the cross-correlation between fluid and particles. As a reminder, the cross-correlation between two functions is defined as:

$$(\mathbf{u_p} * \mathbf{u})(\tau) = \int_{-\infty}^{\infty} \mathbf{u_p}(\tau)\mathbf{u}(\tau + t')\mathrm{d}t' \,, \tag{4.21}$$

Stokes drag only			***Stokes drag, p-grad and added mass***		
a	Delay	Cross-correlation	a	Delay	Cross-correlation
10^{-2}	5.51×10^{-3}	0.925	10^{-2}	5.32×10^{-3}	0.985
3×10^{-2}	1.07×10^{-2}	0.303	3×10^{-2}	3.23×10^{-2}	0.731
6×10^{-2}	0.272	0.255	6×10^{-2}	4.44×10^{-2}	0.591
10^{-1}	0.428	0.259	10^{-1}	4.89×10^{-2}	0.556

Table 4.2: Delay between fluid and particles and cross-correlation in a fully turbulent, average over 1000 particles for 300 seconds for different particles radius, $Re = 3000$, $\rho_t = 1$.

where τ is the displacement. In the case of discrete functions such as the ones used in this work, the cross-correlation becomes:

$$(\mathbf{u_p} * \mathbf{u})(\tau) = \sum_{l=-\infty}^{\infty} \mathbf{u_p}(\tau)\mathbf{u}(\tau + l\Delta t) \,, \tag{4.22}$$

where Δt is the time step. The cross-correlation is normalised to vary between -1 and 1, the higher the correlation, the closer the two vectors are, if the cross-correlation is equal to 1 they are identical. On the contrary, negative correlations imply that the values are anti-correlated, higher values of one variable tend to be associated with lower values of the other. Finally, a cross-correlation of 0 means that the two variables are independent. When studying a cross-correlation, two relevant parameters are the strongest cross-correlation when optimising over τ, that we will call $(\mathbf{u_p} * \mathbf{u})_{max}$, and the value of the displacement associated, referred as τ_{max}.

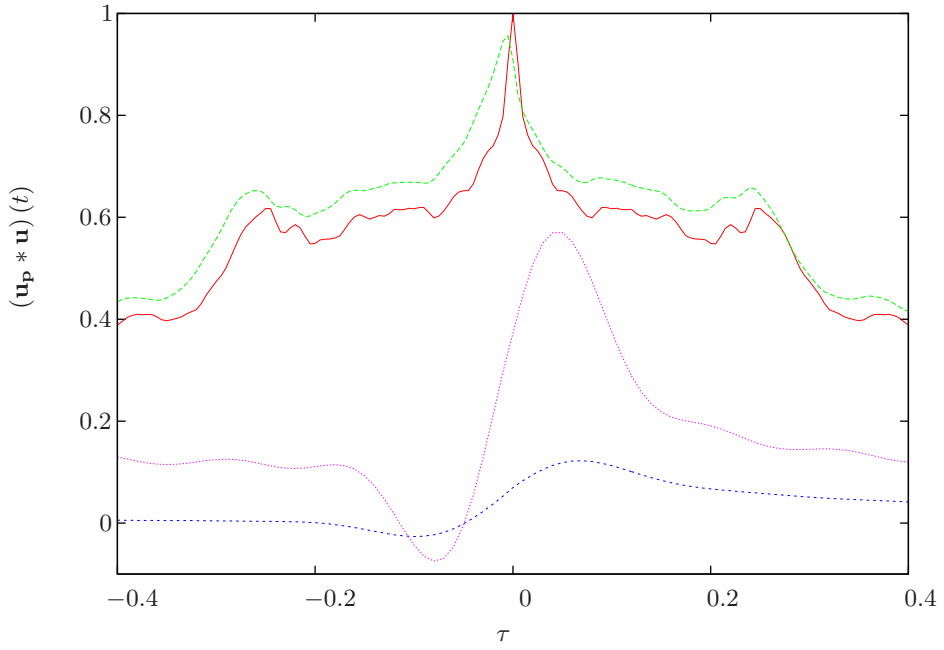

Figure 4.4: Autocorrelation $(\mathbf{u} * \mathbf{u})(\tau)$ (green) and cross-correlation $(\mathbf{u_p} * \mathbf{u})(\tau)$ with $S = 2.2 \times 10^{-5}$ (red), $S = 2 \times 10^{-4}$ (purple) and $S = 2.2 \times 10^{-3}$ (blue).

Figure 4.4 shows example of auto and cross-correlation, the auto-correlation is equal to 1 for $\tau = 0$, as one would expect. The profile of the cross-correlation strongly depends on the dimensionless relaxation time. For smaller values of S, the maximal cross-correlation is very close to 1 and τ_{max} is very small as well, the particle behaves as a tracer and closely follows the fluid. The cross-correlation decreases as S increases, for the largest values of S it peaks around $0.20 - 0.30$. For these values there is almost no connection between fluid and particles, this corresponds to heavy particles being almost decoupled from the fluid phase.
Table 4.2 gives the average values of $(\mathbf{u_p} * \mathbf{u})_{max}$ and τ_{max}, considering a thousand particles over 300 seconds in a fully turbulent flow when only Stokes drag force is considered. Smaller particles follow the fluid very closely with τ_{max} below 10^{-2}, in this case $(\mathbf{u_p} * \mathbf{u})_{max}$is also close to 1. The optimised cross-correlation decreases dramatically fast as the particle radius increases. τ_{max} increases as well, although the change is not as sharp. Even though the particles velocity is dampened when added mass and pressure gradient force are considered, small particles still follow the flow closely, as illustrated through the value of $(\mathbf{u_p} * \mathbf{u})_{max}$. $(\mathbf{u_p} * \mathbf{u})_{max}$ also decreases when the dimensionless relaxation time increases, as one would expect. For $S = 2 \times 10^{-4}$ and $S = 8 \times 10^{-4}$, τ_{max} is lower and the cross-correlation between fluid and particle is higher when the three forces are taken into account than when only the Stokes drag force was included. Neither the pressure gradient nor the added mass force depends on the particle radius, while the Stokes drag term is proportional to the inverse square of the particle size (Equation 4.6). Therefore, pressure gradient and added mass gain importance relative to the Stokes force as a increases.

4.3.2 Particles radial distribution

In this section, we analyse the radial distribution of heavy particles, with $\rho_t = 10^{-3}$, as a function of S. All forces are neglected except the Stokes drag force, for the sake of comparison with Sardina et al. (2012) who used a one way coupled model, where only the Stokes drag force is considering.
Figure 4.5 shows the time evolution of the particle radial repartition evolution with time for various values of the dimensionless relaxation time. Each run has 1000 particles which are initially uniformly distributed. The pipe is separated in four zones of equal length (quartiles) along the radial direction. It is to be noted that when referring to particle position, the centre of the particle is implied. Since particles cannot penetrate the wall, the possible positions for a particle of radius a are within the range $[0, 1 - a]$. This can affect the statistical results for the higher particle sizes. For example, if one considers particles uniformly distributed of radius $a = 0.1$, the expected average radial position is $r = 0.45$ rather than $r = 0.5$.
Three behaviours are illustrated in Figure 4.5, depending on the dimensionless relaxation time:

- $S < 5 \times 10^{-4}$ (top left). For small values of S, particles do follow the flow closely, the particles do not seem to favour a particular radius but the distribution strongly varies with time, with several peaks where a third of all particles are concentrated in a tenth of the pipe radius-wise.

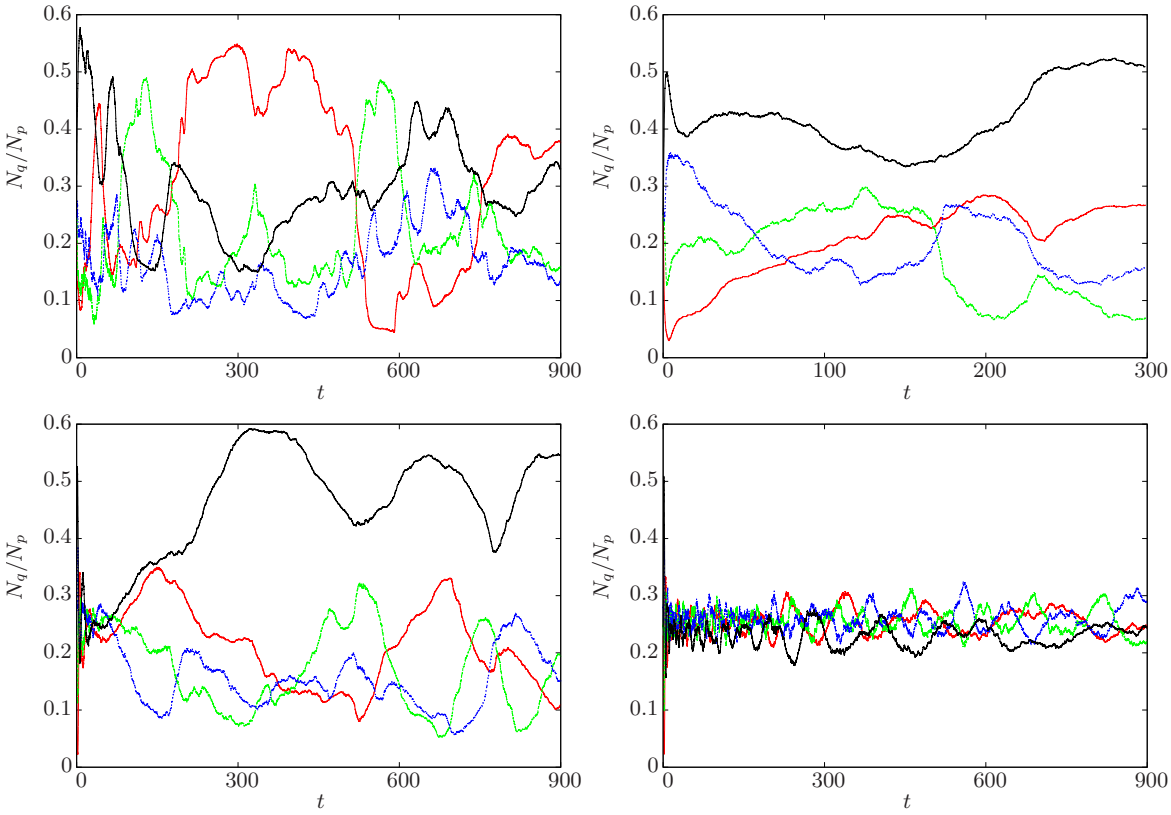

Figure 4.5: Proportion of particles in each radius quartile as a function of time. The line color associated to each quartile are: red for $r = 0-0.25$, green for $r = 0.25-0.5$, blue for for $r = 0.5-0.75$ and black for $r = 0.75-1$. values of S considered are, from top left to bottom right: **Top left:** $S = 2.22 \times 10^{-4}$, **top right:** $S = 8.89 \times 10^{-4}$. **Bottom left:** $S = 5.56 \times 10^{-3}$, **bottom right:** Stokes drag only, $S = 2 \times 10^{-1}$. $Re = 3000$, $\rho_t = 10^{-3}$, $N_p = 1000$.

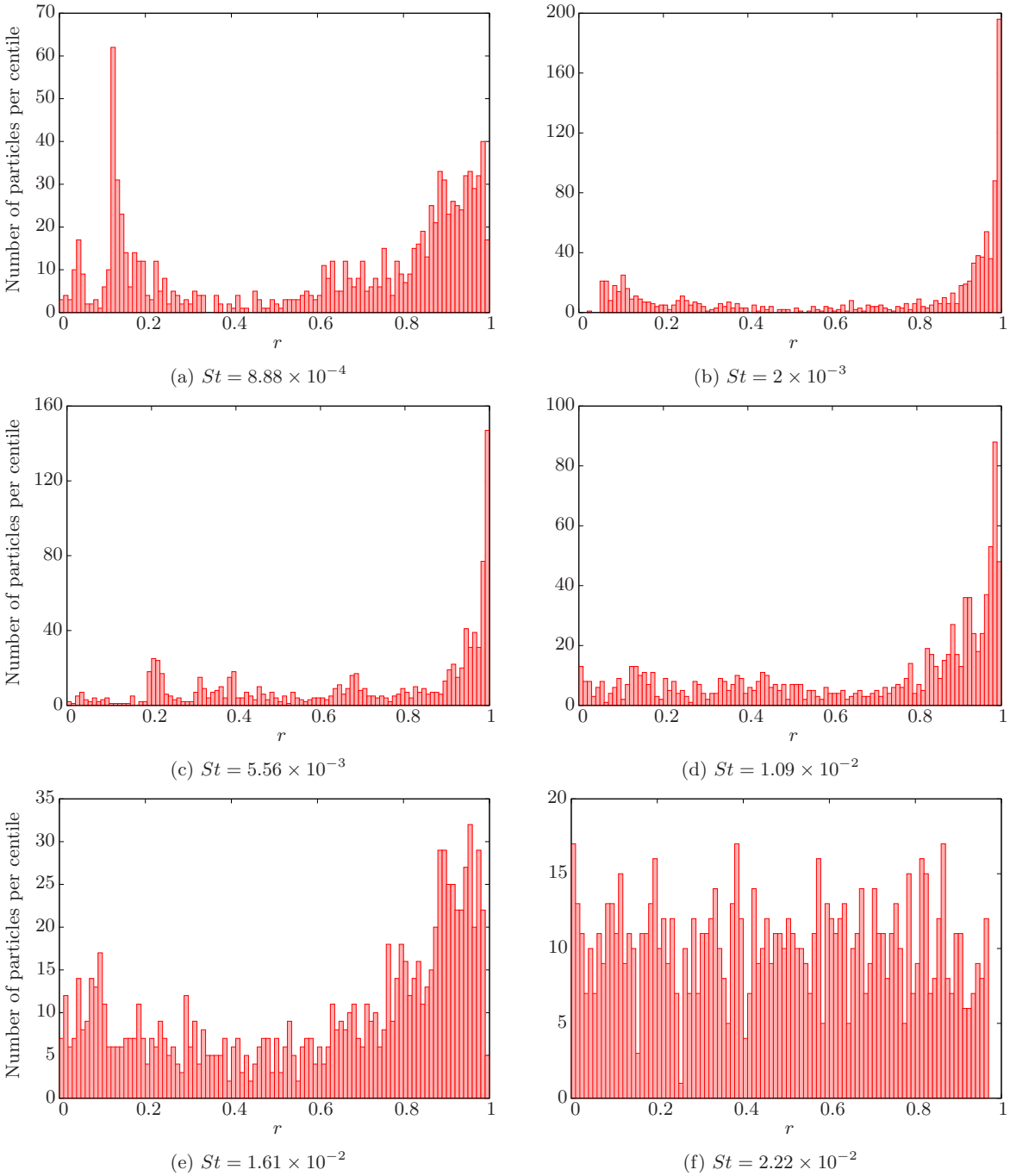

(a) $St = 8.88 \times 10^{-4}$

(b) $St = 2 \times 10^{-3}$

(c) $St = 5.56 \times 10^{-3}$

(d) $St = 1.09 \times 10^{-2}$

(e) $St = 1.61 \times 10^{-2}$

(f) $St = 2.22 \times 10^{-2}$

Figure 4.6: Histogram of particles radial position at $t = 900$. $Re = 3000$, $\rho_t = 10^{-3}$, $N_p = 1000$.

- $9 \times 10^{-4} < S < 2 \times 10^{-3}$. For medium relaxation times, particles significantly drift towards the wall, between $r = 0.75$ and $r = 1$, while there is some variation in the rest of the pipe no other region stands out.

- $S > 2 \times 10^{-3}$. As the S gets larger, particles become less coupled to the flow. The particles stay uniformly distributed with very little variation in time.

The case $S = 8.89 \times 10^{-4}$ illustrates the transition between the first and second behaviour. The particle concentration is highest close to the wall although the difference is not as pronounced as for larger values of S and there are strong distribution variations with time such as observed for $S = 2.22 \times 10^{-4}$. In order to have a more detailed picture of the repartition of the particles in the pipe, we studied snapshots in time of the particles radial position. Figure 4.6 gives histograms of the particles radial position for different dimensionless relaxation times. Each run considers 1000 particles and the histogram bin width is of 0.01, such that in the case of a uniformly distributed particles each bin would contain ten particles.

- Particles start to migrate closer to the wall at $S = 8.89 \times 10^{-4}$ although there are still transient peaks of concentration in the rest of the pipe.

- For $S = 2 \times 10^{-3}$, particles cluster very close to the wall, with almost a fifth of the particles in a radius between 0.99 and 0.1 at this time.

- For $2 \times 10^{-3} \leqslant S \leqslant 1.61 \times 10^{-2}$ particle concentration is still higher close to the wall but the sharpness of the peaks gets less pronounced as the S increases until the particle distribution is homogeneous again for $S = 2.22 \times 10^{-2}$.

One can compare the results to Sardina et al. (2012), who studied a one-way coupled point particle model limited to Stokes drag force for heavy particles, with a density ratio $\rho_p/\rho_f = 1/770$, in the case of wall-flows. While their different geometry, a channel flow, does not allow for direct comparison, the results are qualitatively similar. Very small particles act as tracers but as particle size increases, the particles accumulate close to the wall. The magnitude of the accumulation towards the wall rapidly increases with the particles size until a maximum, wall-accumulation then decreases as the particle size continues to increase.

The particles' accumulation towards the wall is likely to be caused by turbophoresis. Turbophoresis is the tendency of particles to migrate towards zones where turbulence is weaker, in this case close to the wall (Caporaloni et al., 1975; Sardina et al., 2012). When comparing the amplitude of the effect of particle-wall accumulation, it is more pronounced in the case of the wall channel flow. (Sardina et al., 2012) found a ratio of over a hundred between the particle concentration close to the wall and the average concentration, while we find a ratio of at most 20 for the pipe flow.

4.3.3 Particle-particle collision rate

c	$N_p = 100$, $\rho_t = 1$	$N_p = 1000$, $\rho_t = 1$	$N_p = 100$, $\rho_t = 10^{-3}$	$N_p = 1000$, $\rho_t = 10^{-3}$
10^{-4}	3.5	20	10	235
3×10^{-4}	14	80	40	410
10^{-3}	105	940	140	1620
3×10^{-3}	400	9700	360	4760

Table 4.3: Particle collision rate as a function of the flow volume fraction; $c = \frac{N_p 4/3\pi a^3}{V_p}$, with V_p as the pipe volume. Here, only the Stokes drag force is taken into account.

c	$N_p = 100$, $\rho_t = 1$	$N_p = 1000$, $\rho_t = 1$	$N_p = 100$, $\rho_t = 10^{-3}$	$N_p = 1000$, $\rho_t = 10^{-3}$
10^{-4}	0.1	2.5	10	135
3×10^{-4}	0.4	3	20	410
10^{-3}	0.9	8.2	70	1170
3×10^{-3}	3.2	25	200	3200

Table 4.4: Particle collision rate as a function of the flow particle volume fraction $c = \frac{N_p 4/3\pi a^3}{V_p}$, with V_p as the pipe volume. In this case, the stokes drag, pressure gradient and added mass forces are taken into account.

Until now, particle-particle collisions were neglected. When considering one-way coupled particulate flows, this assumption can be made safely. Indeed, there is no feedback from the particles to the fluid: a simulation with N_p particles is equivalent to N_p simulations of a flow containing a single particle. However, the effect of the solid phase on the fluid needs to be included when studying the stability of a particulate flow. One-way coupled simulations with varying parameters where the collision rate is measured were conducted. While the collision rate obtained here with a one-way coupling model is not equal to the one that would be obtained with a two or four-way coupled model; it still gives an estimate of the parameters regimes in which neglecting particle-particle collisions is a reasonable assumption.

Collision rates are shown in Tables 4.3 and 4.4. Several patterns emerge from the data. The particle collision rate increases with the volume fraction, this result was expected. The increase in collision rate, as c increases, is steeper when only the Stokes drag is considered than when Stokes drag, added mass and pressure gradient are considered. However, due to the limited number of cases considered we cannot infer a precise scaling. More interesting is the effect of the number of particles. Even at a constant volume fraction, c; flows with a larger number of particles have a much higher collision rate,

with a more than tenfold increase between 100 and 1000 particles. The addition of pressure gradient and added mass forces significantly decreases the collision rate as well. A possible explanation is the velocity dampening caused by the added mass force, as observed in Section 4.3.1. Even though only dilute particle concentration were considered, there are cases in which collision rates are too high to safely neglect collisions. This needs to be taken into careful consideration when using a two-way coupling model.

4.4 Conclusion

One-way coupling computations showed that there is a particle size range for which the particles accumulate towards the wall, even when particle rotation is not taken into account. The code is still in development, and further effects such as particles rotation and particle-particle collisions are in need of testing and final corrections. The results shown here only consider one-way coupled flows with low particles volume fractions. The code has not been parallelised in the case of two way coupled yet. Therefore we are limited to relatively low amounts of particles (of the order of one thousand) and smaller pipes where the effect of the particles on the fluid phase is minimal. The results are promising and the point particle model presented in this chapter is a versatile tool that should allow for a more advanced study of transition to turbulence in particulate pipe flows.

General conclusion

This thesis focused on the influence of the solid phase on the stability of a particulate pipe flow from several angles through the use of numerical simulations. In Chapter 2, we did analyse the linear stability of a particulate pipe flow where the solid phase is modelled with an Eulerian formulation. The analysis has been made by means of an eigenvalue solver. In the case of homogeneous particle distribution, the particulate pipe flow remains linearly stable, as is the single phase pipe flow (Lessen et al., 1968). The effect of the particle mass concentration f is monotonic and almost linear. On the other hand, the dimensionless relaxation time S affects the growth rate in a more complex way, with a nonmonotonic dependency and two extrema, one stabilising and one destabilising. These extrema also scale with both α and Re.

However, the results are significantly different when considering nonhomogeneous particles distributions. In particular, preferential concentrations of particles at a given radius which are closer to the experimental observations (Matas et al., 2004b). It was found that the particulate flow is linearly unstable within some parametric range. Most noticeably the flow can only be linearly unstable for intermediate values of the Reynolds number. For low Reynolds numbers, the flow is dominated by viscous diffusion, while in the case of high Reynolds numbers, fluid and solid phases are decoupled. As for the effect of the shape of the particles distribution, the effect of particles on stability get more pronounced as particles get more clustered (corresponding to a decrease of σ). When considering the radius of the annulus at which particles are concentrated, linear instability is strongest when $r_d \approx 0.65$, very close to the both in terms Segré-Silberberg radius (Segre and Silberberg, 1962). This is also the radius around which the eigenfunctions of the unstable mode are the largest.

Chapter 3 extended the study of the fully Eulerian model to linear transient growth with a LDNS code adapted from Willis (2017). The optimal linear transient growth of the particulate pipe has been found to scale with Re^2 while the time at which the peak in energy is reached increases linearly as a function of Re, as seen in the single phase pipe flow (Bergström, 1993). The transient growth is increased by the addition of particles for all values of S. The transient growth depends nonmonotonically on S and is maximised for an intermediate value of S: this value is almost independent of Re and σ. Similarly to what has been found for the linear stability analysis, the effect of the solid phase is much stronger for nonhomogeneous particle distributions with increase of the transient growth of over 200% compared to that of the single phase transient growth. The transient growth is most pronounced when particles are concentrated around radii, $r_d = 0.6 - 0.7$. This is consistent with previous results from this work and from the literature (Matas et al., 2004b; Segre and Silberberg, 1962). The optimal initial perturbations peak velocities have also been studied for a $S = 10^{-3}$ (for this value of S the particulate flow can be linearly unstable). It follows that the linear transient growth analysis did not highlight any new mechanism.

In the fourth chapter, we presented a point particle model developed with the purpose to extend the scope of this work. The code is still in development, but the first results are promising. Studying one-way coupled particles, we highlighted several regimes depending on the particles size. Smaller

particles follow the fluid phase closely, acting as tracers. As particles get bigger, they largely follow the motions of the flow while the largest particles are almost independent from the fluid. The way particles are distributed in a turbulent flow is also consistent with these regimes. Small particles do not show a preferential radius but their radial distribution strongly varies with time. This behaviour is likely caused by particles following turbulent structures. The largest particles do not show a preferential radius either, and are much less affected by the fluid, with very little changes in radii across time. The most interesting case is the one of medium-sized particles, which have a marked tendency to aggregate in the region close to the wall. This tendency has been observed in shear flows before (Sardina et al., 2012).

Overall, this thesis highlights the important role of the particle size on the particulate flow stability as particles can have either a stabilising or destabilising effect on the stability depending on their sizes. This is consistent with literature results on both numerical and experimental works (Klinkenberg et al., 2011; Matas et al., 2003). Being able to estimate the effect of particles on the stability in function of their size can allow to better estimate the state of industrial particulate flows who are not easily observable, such as inside pipelines; and to delay the transition to turbulence in a flow by seeding it with particles of the appropriate size. The second critical parameter is how the solid phase is distributed through the pipe, as the location of the particles has a dramatic effect on the flow stability. The effect of particles is consistently the strongest in the region near the wall, in particular close to the Segré-Silberberg radius. Albeit most of these results have been obtained in a simplified framework, it illustrates how the concentration of particles in an annulus could be a key step in the the transition to turbulence.

The point particle model has not been used extensively so far, it is a flexible method and there are many possible ways to extend this work. Notably, one could expand this work on how the particles distribution in the pipe is affected by the particles size for both laminar and turbulent flows. Indeed, the particles position seems to be one of the key parameters in the transition to turbulence, as indicated by both this work as well as previous experimental and numerical results. A better understanding on how particles get distributed in the flow is, therefore, critical when one aim to estimate the conditions for which the transition to turbulence occurs. One can also analyse the relative importance of the various forces, and of the particles rotations and collisions on the flow depending on the flow regime. The interest is two-fold: allowing for a better understanding of the underlying mechanisms between the transition to turbulence of particulate pipe flows; knowing the relative importance of the different forces as a function of the parameter space. This allows for a more efficient study of the problem by neglecting the less relevant forces (or particle-particle interactions). Of interest is also the role of the particles in the transition to turbulence within this new model framework, and how it corroborates with the previous results obtained with the fully Eulerian model, as well as the work done on pipe flows (Matas et al., 2003; Yu et al., 2013).

Future work can be considered for the fully Eulerian model used in Chapters 2 and 3. For example by using more complex particle distributions, closer to real flows. Additional interaction forces can also be taken into account in order to increase the range in which the model is valid. However, the fully Eulerian method has inherent limitations regarding the physical mechanisms and the range in which the results are valid. On the other hand, the point particle model offers several avenues for future work. As is stands, the point particle model does not include rotation. Taking into account particles rotation is necessary to simulate the process of particle migration in laminar flows (Segre and Silberberg, 1962). The position of the particles is highly relevant to flow instability and the development of turbulence. While a carefully chosen initial particles position might give a reasonably accurate approximation of the particles position after their migration for short time scales, it is probably only of limited interest. Therefore, the current point-particle code is, as it stands, not well suited to the study of instability of the flow. It is, however, more adapted to the study of fully turbulent flows. In particular one can study turbulence modulation and how turbulence is affected by varying the particles parameters, such as size and density as well as the mass fraction ratio and whether the distribution is monodisperse and polydisperse. Another phenomenon to consider is turbulence decay, and in which conditions the addition of particles can either delay or provoke it. The point-particle model can be adapted to include the rotation of particles. The rotation rate can be obtained using an empirical formula (Ferrante and Elghobashi, 2003), the effect of collisions rate can be computed in the soft-collision model framework (Zhu and Yu, 2002; Zhu et al., 2007). With the particles' rotation taken into account, the point particles model can be used to study the flow stability. One can consider changes in the critical Reynolds number, whether the addition of particles can lead to new paths of transition to turbulence, and the statistical lifetime of the perturbations in function of the particles characteristics.

Bibliography

Andersson, P., Berggren, M., and Henningson, D. S. (1999). Optimal disturbances and bypass transition in boundary layers. *Physics of Fluids*, 11(1):134–150.

Asmolov, E. S. (1999). The inertial lift on a spherical particle in a plane poiseuille flow at large channel reynolds number. *Journal of Fluid Mechanics*, 381:63–87.

Avila, K., Moxey, D., de Lozar, A., Avila, M., Barkley, D., and Hof, B. (2011). The onset of turbulence in pipe flow. *Science*, 333(6039):192–196.

Baines, P. G., Majumdar, S. J., and Mitsudera, H. (1996). The mechanics of the tollmien-schlichting wave. *Journal of Fluid Mechanics*, 312:107–124.

Balachandar, S. and Eaton, J. K. (2010). Turbulent dispersed multiphase flow. *Annual Review of Fluid Mechanics*, 42:111–133.

Barkley, D. (2011). Simplifying the complexity of pipe flow. *Physical Review E*, 84(1):016309.

Basset, A. (1961). A treatise on hydrodynamics (deighton bell, cambridge, 1888). reprinted.

Bergström, L. (1992). Initial algebraic growth of small angular dependent disturbances in pipe poiseuille flow. *Studies in Applied Mathematics*, 87(1):61–79.

Bergström, L. (1993). Optimal growth of small disturbances in pipe poiseuille flow. *Physics of Fluids A: Fluid Dynamics*, 5(11):2710–2720.

Berlin, S., Lundbladh, A., and Henningson, D. (1994). Spatial simulations of oblique transition in a boundary layer. *Physics of Fluids (1994-present)*, 6(6):1949–1951.

Boivin, M., Simonin, O., and Squires, K. D. (1998). Direct numerical simulation of turbulence modulation by particles in isotropic turbulence. *Journal of Fluid Mechanics*, 375:235–263.

Boronin, S. (2012). Optimal disturbances of a dusty-gas plane-channel flow with a nonuniform distribution of particles. *Fluid Dynamics*, 47(3):351–363.

Boronin, S. and Osiptsov, A. (2008). Stability of a disperse-mixture flow in a boundary layer. *Fluid Dynamics*, 43(1):66.

Boronin, S. A. and Osiptsov, A. N. (2016). Nonmodal instability of a stratified plane-channel suspension flow with fine particles. *Physical Review E*, 93(3):033107.

Brandt, L. (2014). The lift-up effect: The linear mechanism behind transition and turbulence in shear flows. *European Journal of Mechanics-B/Fluids*, 47:80–96.

Budanur, N. B. and Hof, B. (2017). Heteroclinic path to spatially localized chaos in pipe flow. *Journal of Fluid Mechanics*, 827.

Caporaloni, M., Tampieri, F., Trombetti, F., and Vittori, O. (1975). Transfer of particles in nonisotropic air turbulence. *Journal of the atmospheric sciences*, 32(3):565–568.

Cerbus, R. T., Liu, C.-c., Gioia, G., and Chakraborty, P. (2018). Laws of resistance in transitional pipe flows. *Physical review letters*, 120(5):054502.

Chantry, M. and Schneider, T. M. (2014). Studying edge geometry in transiently turbulent shear flows. *Journal of Fluid Mechanics*, 747:506–517.

Craik, A. D. (1971). Non-linear resonant instability in boundary layers. *Journal of Fluid Mechanics*, 50(02):393–413.

Cundall, P. A. and Strack, O. D. (1979). A discrete numerical model for granular assemblies. *geotechnique*, 29(1):47–65.

Darbyshire, A. and Mullin, T. (1995). Transition to turbulence in constant-mass-flux pipe flow. *Journal of Fluid Mechanics*, 289:83–114.

De La Mora, J. F. and Rosner, D. (1981). Inertial deposition of particles revisited and extended: Eulerian approach to a traditionally lagrangian problem. *PhysicoChem. Hydrodyn.*, 2(1):1–21.

Di Giacinto, M., Sabetta, F., and Piva, R. (1982). Two-way coupling effects in dilute gas-particle flows. *Journal of Fluids Engineering*, 104(3):304–311.

Durst, F., Miloievic, D., and Schönung, B. (1984). Eulerian and lagrangian predictions of particulate two-phase flows: a numerical study. *Applied Mathematical Modelling*, 8(2):101–115.

Eaton, J. K. and Fessler, J. (1994). Preferential concentration of particles by turbulence. *International Journal of Multiphase Flow*, 20:169–209.

Eckhardt, B., Schneider, T. M., Hof, B., and Westerweel, J. (2007). Turbulence transition in pipe flow. *Annu. Rev. Fluid Mech.*, 39:447–468.

Einstein, A. (1911). Berichtigung zu meiner arbeit: Eine neue bestimmung der molekuldimensionen. *Annalen der Physik*, 339(3):591–592.

Elghobashi, S. (1991). Particle-laden turbulent flows: direct simulation and closure models. *Applied Scientific Research*, 48(3-4):301–314.

Faisst, H. and Eckhardt, B. (2004). Sensitive dependence on initial conditions in transition to turbulence in pipe flow. *Journal of Fluid Mechanics*, 504:343–352.

Ferrante, A. and Elghobashi, S. (2003). On the physical mechanisms of two-way coupling in particle-laden isotropic turbulence. *Physics of fluids*, 15(2):315–329.

Ferry, J. and Balachandar, S. (2001). A fast eulerian method for disperse two-phase flow. *International journal of multiphase flow*, 27(7):1199–1226.

Ferry, J., Rani, S. L., and Balachandar, S. (2003). A locally implicit improvement of the equilibrium eulerian method. *International journal of multiphase flow*, 29(6):869–891.

Février, P., Simonin, O., and Squires, K. D. (2005). Partitioning of particle velocities in gas–solid turbulent flows into a continuous field and a spatially uncorrelated random distribution: theoretical formalism and numerical study. *Journal of Fluid Mechanics*, 533:1–46.

Fox, R. O., Laurent, F., and Massot, M. (2008). Numerical simulation of spray coalescence in an eulerian framework: direct quadrature method of moments and multi-fluid method. *Journal of Computational Physics*, 227(6):3058–3088.

Gingold, R. A. and Monaghan, J. J. (1977). Smoothed particle hydrodynamics: theory and application to non-spherical stars. *Monthly notices of the royal astronomical society*, 181(3):375–389.

Glowinski, R., Pan, T.-W., Hesla, T. I., and Joseph, D. D. (1999). A distributed lagrange multiplier/fictitious domain method for particulate flows. *International Journal of Multiphase Flow*, 25(5):755–794.

Gore, R. and Crowe, C. (1991). Modulation of turbulence by a dispersed phase. *Journal of fluids engineering*, 113(2):304–307.

Guégan, A., Schmid, P. J., and Huerre, P. (2006). Optimal energy growth and optimal control in swept hiemenz flow. *Journal of Fluid Mechanics*, 566:11–45.

Hassan, Y. (1998). Multiparticle imaging velocimetry measurements in two-phase flow. In *Proc. OECD/CSNI Specialist Meeting on Advanced Instrumentation and Measurement Techniques*, pages 17–20.

Hassan, Y., Blanchat, T., and Seeley Jr, C. (1992). Piv flow visualisation using particle tracking techniques. *Measurement Science and Technology*, 3(7):633.

Herbert, T. (1988). Secondary instability of boundary layers. *Annual Review of Fluid Mechanics*, 20(1):487–526.

Hertz, H. (1882). Ueber die beruhrung fester elastischer korper. *J Reine Angew Math*, 92:156–171.

Hof, B., Juel, A., and Mullin, T. (2003). Scaling of the turbulence transition threshold in a pipe. *Physical review letters*, 91(24):244502.

Hof, B., Westerweel, J., Schneider, T. M., and Eckhardt, B. (2006). Finite lifetime of turbulence in shear flows. *Nature*, 443(7107):59–62.

Jackson, R. (2000). *The dynamics of fluidized particles*. Cambridge University Press.

Jeffrey, R. C. and Pearson, J. (1965). Particle motion in laminar vertical tube flow. *Journal of Fluid Mechanics*, 22(04):721–735.

Joseph, D. and Carmi, S. (1969). Stability of poiseuille flow in pipes, annuli, and channels. *Quarterly of applied Mathematics*, 26(4):575–599.

Kerswell, R. (2011). Lecture 9: Triggering transitions-towards minimal seeds. *Summer program in Geophysical Fluid Dynamics, Woods Hole Oceanographic Institute, Massachusetts, USA (http://www. whoi. edu/main//gfd/proceedings-volumes/2011)*.

Kidanemariam, A. G. and Uhlmann, M. (2014a). Direct numerical simulation of pattern formation in subaqueous sediment. *Journal of Fluid Mechanics*, 750:R2.

Kidanemariam, A. G. and Uhlmann, M. (2014b). Interface-resolved direct numerical simulation of the erosion of a sediment bed sheared by laminar channel flow. *International Journal of Multiphase Flow*, 67:174–188.

Klebanoff, P., Tidstrom, K., and Sargent, L. (1962). The three-dimensional nature of boundary-layer instability. *Journal of Fluid Mechanics*, 12(01):1–34.

Klinkenberg, J., de Lange, H., and Brandt, L. (2011). Modal and non-modal stability of particle-laden channel flow. *Physics of Fluids (1994-present)*, 23(6):064110.

Klinkenberg, J., Sardina, G., De Lange, H., and Brandt, L. (2013). Numerical study of laminar-turbulent transition in particle-laden channel flow. *Physical Review E*, 87(4):043011.

Koshizuka, S. and Oka, Y. (1996). Moving-particle semi-implicit method for fragmentation of incompressible fluid. *Nuclear science and engineering*, 123(3):421–434.

Kreiss, G., Lundbladh, A., and Henningson, D. S. (1994). Bounds for threshold amplitudes in subcritical shear flows. *Journal of Fluid Mechanics*, 270:175–198.

Krieger, I. M. (1972). Rheology of monodisperse latices. *Advances in Colloid and Interface Science*, 3(2):111–136.

Kussin, J. and Sommerfeld, M. (2002). Experimental studies on particle behaviour and turbulence modification in horizontal channel flow with different wall roughness. *Experiments in Fluids*, 33(1):143–159.

Landahl, M. T. (1975). Wave breakdown and turbulence. *SIAM Journal on Applied Mathematics*, 28(4):735–756.

Lawson, N. and Wu, J. (1997). Three-dimensional particle image velocimetry: error analysis of stereoscopic techniques. *Measurement Science and Technology*, 8(8):894.

Lemoult, G., Shi, L., Avila, K., Jalikop, S. V., Avila, M., and Hof, B. (2016). Directed percolation phase transition to sustained turbulence in couette flow. *Nature Physics*, 12(3):254–258.

Lessen, M., Sadler, S. G., and Liu, T.-Y. (1968). Stability of pipe poiseuille flow. *Physics of Fluids (1958-1988)*, 11(7):1404–1409.

Mack, L. M. (1976). A numerical study of the temporal eigenvalue spectrum of the blasius boundary layer. *Journal of Fluid Mechanics*, 73(3):497–520.

Marble, F. E. (1970). Dynamics of dusty gases. *Annual Review of Fluid Mechanics*, 2(1):397–446.

Matas, J.-P., Glezer, V., Guazzelli, É., and Morris, J. F. (2004a). Trains of particles in finite-reynolds-number pipe flow. *Physics of Fluids (1994-present)*, 16(11):4192–4195.

Matas, J.-P., Morris, J. F., and Guazzelli, E. (2003). Transition to turbulence in particulate pipe flow. *Physical review letters*, 90(1):014501.

Matas, J.-P., Morris, J. F., and Guazzelli, É. (2004b). Inertial migration of rigid spherical particles in poiseuille flow. *Journal of Fluid Mechanics*, 515:171–195.

Maxey, M. R. and Riley, J. J. (1983). Equation of motion for a small rigid sphere in a nonuniform flow. *Physics of Fluids (1958-1988)*, 26(4):883–889.

Melling, A. (1997). Tracer particles and seeding for particle image velocimetry. *Measurement Science and Technology*, 8(12):1406.

Meseguer, A. and Trefethen, L. N. (2003). Linearized pipe flow to reynolds number 10 7. *Journal of Computational Physics*, 186(1):178–197.

Migdal, D. and Agosta, V. (1967). A source flow model for continuum gas-particle flow. *Journal of Applied Mechanics*, 34:860.

Mikulencak, D. R. and Morris, J. F. (2004). Stationary shear flow around fixed and free bodies at finite reynolds number. *Journal of Fluid Mechanics*, 520:215–242.

Mio, H., Shimosaka, A., Shirakawa, Y., and Hidaka, J. (2005). Optimum cell size for contact detection in the algorithm of the discrete element method. *Journal of chemical engineering of Japan*, 38(12):969–975.

Monaghan, J. (2012). Smoothed particle hydrodynamics and its diverse applications. *Annual Review of Fluid Mechanics*, 44:323–346.

Monaghan, J. J. (1992). Smoothed particle hydrodynamics. *Annual review of astronomy and astrophysics*, 30(1):543–574.

Monaghan, J. J. (2005). Smoothed particle hydrodynamics. *Reports on progress in physics*, 68(8):1703.

Mooney, M. (1951). The viscosity of a concentrated suspension of spherical particles. *Journal of colloid science*, 6(2):162–170.

Mueller, S., Llewellin, E., and Mader, H. (2009). The rheology of suspensions of solid particles. In *Proceedings of the Royal Society of London A: Mathematical, Physical and Engineering Sciences*, page rspa20090445. The Royal Society.

Muth, B., Müller, M., Eberhard, P., and Luding, S. (2007). Collision detection and administration methods for many particles with different sizes. *Preprint submitted to Elsevier Science*.

Nishi, M., Ünsal, B., Durst, F., and Biswas, G. (2008). Laminar-to-turbulent transition of pipe flows through puffs and slugs. *Journal of Fluid Mechanics*, 614:425–446.

Okamoto, K., Hassan, Y., and Schmidl, W. (1995). New tracking algorithm for particle image velocimetry. *Experiments in Fluids*, 19(5):342–347.

Orr, W. M. (1907). The stability or instability of the steady motions of a perfect liquid and of a viscous liquid. part ii: A viscous liquid. pages 69–138.

Osiptsov, A. (1988). Motion of a dusty gas at the entrance to a flat channel and a circular pipe. *Fluid Dynamics*, 23(6):867–874.

Patankar, N. and Joseph, D. (2001). Modeling and numerical simulation of particulate flows by the eulerian–lagrangian approach. *International Journal of Multiphase Flow*, 27(10):1659–1684.

Peixinho, J. and Mullin, T. (2006). Decay of turbulence in pipe flow. *Physical review letters*, 96(9):094501.

Peixinho, J. and Mullin, T. (2007). Finite-amplitude thresholds for transition in pipe flow. *Journal of Fluid Mechanics*, 582:169–178.

Peskin, C. S. (1972). *Flow patterns around heart valves: a digital computer method for solving the equations of motion*. UMI.

Peskin, C. S. (2002). The immersed boundary method. *Acta numerica*, 11:479–517.

Pfenniger, W. (1961). Transition in the inlet length of tubes at high reynolds numbers, boundary layer and flow control. *GV Lachman (éd.)*, 970.

Poiseuille, J. (1836). Observations of blood flow. *Ann Sci Nat STrie*, 5(2).

Pringle, C. C. and Kerswell, R. R. (2010). Using nonlinear transient growth to construct the minimal seed for shear flow turbulence. *Physical review letters*, 105(15):154502.

Pringle, C. C., Willis, A. P., and Kerswell, R. R. (2012). Minimal seeds for shear flow turbulence: using nonlinear transient growth to touch the edge of chaos. *Journal of Fluid Mechanics*, 702:415–443.

Prosperetti, A. and Oguz, H. (2001). Physalis: a new o (n) method for the numerical simulation of disperse systems: potential flow of spheres. *Journal of Computational Physics*, 167(1):196–216.

Reshotko, E. (2001). Transient growth: A factor in bypass transition. *Physics of Fluids (1994-present)*, 13(5):1067–1075.

Reuter, J. and Rempfer, D. (2004). Analysis of pipe flow transition. part i. direct numerical simulation. *Theoretical and Computational Fluid Dynamics*, 17(4):273–292.

Reynolds, O. (1883). An experimental investigation of the circumstances which determine whether the motion of water shall be direct or sinuous, and of the law of resistance in parallel channels. *Proceedings of the royal society of London*, 35(224-226):84–99.

Rubinow, S. and Keller, J. B. (1961). The transverse force on a spinning sphere moving in a viscous fluid. *Journal of Fluid Mechanics*, 11(3):447–459.

Saffman, P. (1962). On the stability of laminar flow of a dusty gas. *Journal of fluid mechanics*, 13(1):120–128.

Saffman, P. (1965). The lift on a small sphere in a slow shear flow. *Journal of fluid mechanics*, 22(2):385–400.

Sakai, M., Shigeto, Y., Sun, X., Aoki, T., Saito, T., Xiong, J., and Koshizuka, S. (2012). Lagrangian–lagrangian modeling for a solid–liquid flow in a cylindrical tank. *Chemical engineering journal*, 200:663–672.

Sano, M. and Tamai, K. (2016). A universal transition to turbulence in channel flow. *Nature Physics*, 12(3):249.

Sardina, G., Schlatter, P., Brandt, L., Picano, F., and Casciola, C. M. (2012). Wall accumulation and spatial localization in particle-laden wall flows. *Journal of Fluid Mechanics*, 699:50–78.

Schmid, P. J. and Henningson, D. S. (2012). *Stability and transition in shear flows*, volume 142. Springer Science & Business Media.

Schneider, T. M., Eckhardt, B., and Yorke, J. A. (2007). Turbulence transition and the edge of chaos in pipe flow. *Physical review letters*, 99(3):034502.

Segre, G. and Silberberg, A. (1962). Behaviour of macroscopic rigid spheres in poiseuille flow part 1. determination of local concentration by statistical analysis of particle passages through crossed light beams. *Journal of fluid mechanics*, 14(1):115–135.

Sexl, T. (1927). Zur stabilitätsfrage der poiseuilleschen und couetteschen strömung. *Annalen der Physik*, 388(14):835–848.

Shan, H., Ma, B., Zhang, Z., and Nieuwstadt, F. (1999). Direct numerical simulation of a puff and a slug in transitional cylindrical pipe flow. *Journal of Fluid Mechanics*, 387:39–60.

Shao, X., Yu, Z., and Sun, B. (2008). Inertial migration of spherical particles in circular poiseuille flow at moderately high reynolds numbers. *Physics of Fluids (1994-present)*, 20(10):103307.

Shimizu, M., Manneville, P., Duguet, Y., and Kawahara, G. (2014). Splitting of a turbulent puff in pipe flow. *Fluid Dynamics Research*, 46(6):061403.

Sipos, M. and Goldenfeld, N. (2011). Directed percolation describes lifetime and growth of turbulent puffs and slugs. *Physical Review E*, 84(3):035304.

Squires, K. D. and Eaton, J. K. (1991). Preferential concentration of particles by turbulence. *Physics of Fluids A: Fluid Dynamics*, 3(5):1169–1178.

Stock, D., Jurewicz, J., Crowe, C., and Eschbach, J. (1975). Measurement of both gas and particle velocity in turbulent two-phase flow.

Sun, X., Sakai, M., and Yamada, Y. (2013). Three-dimensional simulation of a solid–liquid flow by the dem–sph method. *Journal of Computational Physics*, 248:147–176.

Taylor, M. (1955). The flow of blood in narrow tubes. *Australian Journal of Experimental Biology & Medical Science*, 33(1).

Tritton, D. (1988). Physical fluid dynamics, clarendon.

Uhlmann, M. (2005). An immersed boundary method with direct forcing for the simulation of particulate flows. *Journal of Computational Physics*, 209(2):448–476.

Van den Brule, B. and Jongschaap, R. (1991). Modeling of concentrated suspensions. *Journal of statistical physics*, 62(5-6):1225–1237.

Vance, M. W., Squires, K. D., and Simonin, O. (2006). Properties of the particle velocity field in gas-solid turbulent channel flow. *Physics of Fluids*, 18(6):063302.

Vand, V. (1948). Viscosity of solutions and suspensions. i. theory. *The Journal of Physical Chemistry*, 52(2):277–299.

Waleffe, F. (1995). Transition in shear flows. nonlinear normality versus non-normal linearity. *Physics of Fluids*, 7(12):3060–3066.

Waleffe, F. (1997). On a self-sustaining process in shear flows. *Physics of Fluids*, 9(4):883–900.

Willis, A. P. (2017). The Openpipeflow Navier–Stokes solver. *SoftwareX*, 6:124–127.

Wu, X., Stewart, P. A., and Cowley, S. J. (1996). On the weakly nonlinear development of tollmien-schlichting wavetrains in boundary layers. *Journal of Fluid Mechanics*, 323:133–171.

Wygnanski, I. and Champagne, F. (1973). On transition in a pipe. part 1. the origin of puffs and slugs and the flow in a turbulent slug. *Journal of Fluid Mechanics*, 59(02):281–335.

Wygnanski, I., Sokolov, M., and Friedman, D. (1975). On transition in a pipe. part 2. the equilibrium puff. *Journal of Fluid Mechanics*, 69(02):283–304.

Yamamoto, Y., Potthoff, M., Tanaka, T., Kajishima, T., and Tsuji, Y. (2001). Large-eddy simulation of turbulent gas–particle flow in a vertical channel: effect of considering inter-particle collisions. *Journal of Fluid Mechanics*, 442:303–334.

Yu, Z., Wu, T., Shao, X., and Lin, J. (2013). Numerical studies of the effects of large neutrally buoyant particles on the flow instability and transition to turbulence in pipe flow. *Physics of Fluids (1994-present)*, 25(4):043305.

Zhao, D., Nezami, E. G., Hashash, Y. M., and Ghaboussi, J. (2006). Three-dimensional discrete element simulation for granular materials. *Engineering Computations*, 23(7):749–770.

Zhu, H. and Yu, A. (2002). Averaging method of granular materials. *Physical Review E*, 66(2):021302.

Zhu, H., Zhou, Z., Yang, R., and Yu, A. (2007). Discrete particle simulation of particulate systems: theoretical developments. *Chemical Engineering Science*, 62(13):3378–3396.

Zikanov, O. Y. (1996). On the instability of pipe poiseuille flow. *Physics of Fluids*, 8(11):2923–2932.

Personal publications

Rouquier, A., Potherat, A., and Pringle, C. (2018). An instability mechanism for particulate pipe flow. *Journal of fluid mechanics DOI: https://doi.org/10.1017/jfm.2019.264*.

Rouquier, A., Potherat, A., and Pringle, C. (2019). Linear transient growth of particulate pipe flows. *arXiv preprint arXiv:1903.10389.pdf*

Conference presentations

Rouquier, A., Potherat, A., and Pringle, C. (2016). Linear stability analysis of particulate pipe flow. *International Congress of Theoretical and Applied Mechanics, 24th edition.*

Rouquier, A., Potherat, A., and Pringle, C. (2017). Linear stability analysis of particulate pipe flow, effect of nonhomogenous distributions. *Bifurcations and Instabilities in Fluid Dynamics, 7th symposium.*

List of Figures

List of Tables

Appendix A

Transient growth, derivation of the adjoint system of equations

A.1 Direct system of equations

Reminder of the system of equations used in chapter 2 and 3:
The fluid equation of motion (NS):

$$\partial_t \mathbf{u} = -\nabla p \; - \mathbf{U}\cdot\nabla\mathbf{u} \; - \mathbf{u}\cdot\nabla\mathbf{U} + \frac{1}{Re}\nabla^2\mathbf{u} + \frac{fN_0}{SRe}\left(\mathbf{u_p}-\mathbf{u}\right). \tag{A.1}$$

The particle equation of motion (NSp):

$$\partial_t \mathbf{u_p} = -\mathbf{u_p}\cdot\nabla\mathbf{U} - \mathbf{U}\cdot\nabla\mathbf{u_p} + \frac{1}{SRe}\left(\mathbf{u}-\mathbf{u_p}\right). \tag{A.2}$$

The conservation equation for the density of particles (Neq):

$$\partial_t N = -\nabla\cdot\left(N\,\mathbf{u_p}\right). \tag{A.3}$$

Mass conservation of the fluid:

$$\nabla\cdot\mathbf{u} = 0\,. \tag{A.4}$$

The transient growth problem is about finding which perturbation $\mathbf{u}$ for a given initial energy E_0 will produce the maximum energy E_t at a given time T. This is equivalent to maximising $\mathscr{L}$.

$$\begin{aligned}\mathscr{L} = &\left\langle \frac{1}{2}\left(m_f\,\mathbf{u}^2(T) + m_p\,\mathbf{u_p^2}(T)\right)\right\rangle - \lambda\left[\left\langle\frac{1}{2}\left(m_f\,\mathbf{u^2}(0) + m_p\,\mathbf{u_p^2}(0)\right) - E_0\right\rangle\right]\\ &- \int_0^T \langle\Upsilon\cdot\mathbf{NS}\rangle\,\mathrm{d}t - \int_0^T \langle\Upsilon_p\cdot\mathbf{NSp}\rangle\,\mathrm{d}t - \int_0^T \langle\Pi\cdot[\nabla\cdot u]\rangle\,\mathrm{d}t - \int_0^T \langle\Gamma\cdot\mathbf{Neq}\rangle\,\mathrm{d}t\,,\end{aligned} \tag{A.5}$$

with $\left\langle\,\cdot\,\right\rangle$ the volume integration.

$\mathscr{L}$ is maximised when $\delta\mathscr{L} = 0$, this corresponds to (with $m_p = \frac{\rho_p}{N}$) :

$$\delta\left\langle m_p\,\mathbf{u_p^2}\right\rangle = \left\langle 2m_p\,\mathbf{u_p}\,\delta\mathbf{u_p} - \rho_p\,\mathbf{u_p^2}\,\frac{\delta N}{N^2}\right\rangle = \left\langle 2m_p\,\mathbf{u_p}\,\delta\mathbf{u_p} - m_p\,\mathbf{u_p^2}\,\frac{\delta N}{N}\right\rangle, \tag{A.6}$$

$$\delta\left\langle\frac{1}{2}\left(m_f\,\mathbf{u}^2(T) + m_p\,\mathbf{u_p^2}(T)\right)\right\rangle = \left\langle m_f\,\mathbf{u}(T)\,\delta\mathbf{u}(T) + m_p\,\mathbf{u_p}(T)\;\delta\mathbf{u_p}(T) - m_p\,\mathbf{u_p}(T)^2\,\frac{\delta N}{N}\right\rangle, \tag{A.7}$$

and:

$$\delta\left[\lambda\left\langle z,\frac{1}{2}\left(m_f\,\mathbf{u^2}(0)+m_p\,\mathbf{u_p^2}(0)\right)\right\rangle\right]=\lambda\left\langle m_f\,\mathbf{u}(0)\,\delta\mathbf{u}(0)+m_p\,\mathbf{u_p}(0)\;\delta\mathbf{u_p}(0)-m_p\,\mathbf{u_p^2}(0)\;\frac{\delta N}{N}\right\rangle, \tag{A.8}$$

$\delta\mathscr{L}$ is expressed by:

$$\begin{aligned}\delta\mathscr{L}=&\left\langle m_f\,\mathbf{u}(T)\;\delta\mathbf{u}(T)+m_p\,\mathbf{u_p}(T)\,\delta\mathbf{u_p}(T)-m_p\,\mathbf{u_p^2}(T)\;\frac{\delta N}{N}\right\rangle\\&-\lambda\left\langle m_f\,\mathbf{u}(0)\delta\mathbf{u}(0)+m_p\,\mathbf{u_p}(0)\;\delta\mathbf{u_p}(0)-m_p\,\mathbf{u_p^2}(0)\;\frac{\delta N}{N}\right\rangle\\&-\int_0^T\langle\,\delta\Upsilon\cdot\mathrm{NS}\,\rangle\,\mathrm{d}t-\int_0^T\langle\delta\Upsilon_p\cdot\mathrm{NSp}\rangle\,\mathrm{d}t-\int_0^T\langle\delta\Pi\cdot[\nabla\cdot\mathbf{u}]\,\rangle\,\mathrm{d}t-\int_0^T\langle\delta\Gamma\cdot\mathrm{Neq}\rangle\,\mathrm{d}t\\&-\int_0^T\langle\Upsilon\cdot\delta(\mathrm{NS})\,\rangle\,\mathrm{d}t-\int_0^T\langle\Upsilon_p\cdot\delta(\mathrm{NSp})\rangle\,\mathrm{d}t-\int_0^T\langle\Pi\cdot[\nabla\cdot\delta\mathbf{u}]\,\rangle\,\mathrm{d}t-\int_0^T\langle\Gamma\cdot\delta(\mathrm{Neq})\rangle\,\mathrm{d}t\,.\end{aligned} \tag{A.9}$$

The aim is to obtain the adjoint equations looking as:
$\delta\mathbf{u}\,/\,\mathbf{u_p}\,/\,N$. (Adjoint equation) , avoiding terms like $\delta(\nabla X)$ or $\delta(\partial_t X)$
Let us derive the adjoint equation term by term. Small reminder, all variables are, in our model, periodic, then using the Stokes theorem, one can prove that $\iiint_V\nabla(X)=\oiint_S X=0$.
Time-related terms for Equation (A.1):

$$\int_0^T\langle\Upsilon\cdot\delta(\partial_t\mathbf{u})\,\rangle\,\mathrm{d}t=\int_0^T\delta\cdot\langle\,\Upsilon\,\partial_t\mathbf{u}\,\rangle\,\mathrm{d}t-\int_0^T\langle\,\delta\mathbf{u}\cdot\partial_t\Upsilon\,\rangle\,\mathrm{d}t \tag{A.10}$$

$$=\langle\,\Upsilon(T)\cdot\delta\mathbf{u}(T)-\Upsilon(0)\cdot\delta\mathbf{u}(0)\,\rangle-\int_0^T\langle\,\delta\mathbf{u}\cdot\partial_t\Upsilon\,\rangle\,\mathrm{d}t\,, \tag{A.11}$$

similarly for equation ((A.2)):

$$\int_0^T\langle\Upsilon\cdot\delta(\partial_t\mathbf{u})\,\rangle\,\mathrm{d}t=\langle\,\Upsilon_p(T)\cdot\delta\mathbf{u_p}(T)-\Upsilon_p(0)\cdot\delta\mathbf{u_p}(0)\,\rangle-\int_0^T\langle\,\delta\mathbf{u_p}\,\partial_t\Upsilon_p\,\rangle\,\mathrm{d}t\,, \tag{A.12}$$

and Equation (A.3):

$$\begin{aligned}\int_0^T\langle\Gamma\cdot\delta\partial_t N\,\rangle\,\mathrm{d}t=&\int_0^T\langle\;\partial_t(\Gamma\,\delta N)\,\rangle\,\mathrm{d}t-\int_0^T\langle\,\delta N\cdot\partial_t\Gamma\rangle\,,\mathrm{d}t\\=&\langle\,\Gamma(T)\cdot\delta N(T)-\Gamma(0)\cdot\delta N(0)\,\rangle-\int_0^T\langle\,\delta N\cdot\partial_t\Gamma\rangle\,\mathrm{d}t\,.\end{aligned} \tag{A.13}$$

Linear convective term for Equation (A.1):

$$\int_0^T \langle \Upsilon \cdot \delta(\mathbf{U}\,\partial_z \mathbf{u}) \rangle \,\mathrm{d}t \;=\; \int_0^T \langle \Upsilon \cdot \mathbf{U}\,\partial_z(\delta\mathbf{u}) \rangle \,\mathrm{d}t \;=\; \int_0^T \langle \mathbf{U} \cdot \partial_z(\Upsilon\,\delta\mathbf{u}) \rangle \,\mathrm{d}t \;-\; \int_0^T \langle\, \delta\mathbf{u} \cdot \mathbf{U}\,\partial_z \Upsilon \rangle \,\mathrm{d}t$$

$$= -\int_0^T \langle\, \delta\mathbf{u} \cdot \mathbf{U}\,\partial_z \Upsilon \rangle \,\mathrm{d}t\,, \tag{A.14}$$

similarly the linear convective term for Equation (A.2):

$$\int_0^T \langle \Upsilon_p \cdot \delta(\mathbf{U}\,\partial_z \mathbf{u_p}) \rangle \,\mathrm{d}t \;= -\int_0^T \langle \delta\mathbf{u_p} \cdot \mathbf{U}\,\partial_z \Upsilon_p \rangle \,\mathrm{d}t\,, \tag{A.15}$$

and for Equation (A.3):

$$\int_0^T \langle \Gamma \cdot \delta\,\nabla(N_0\,\mathbf{u_p}) \rangle \,\mathrm{d}t \;= -\int_0^T \langle \delta N_0 \cdot \mathbf{u_p}\,\nabla\Gamma \rangle \,\mathrm{d}t \;-\; \int_0^T \langle \delta\mathbf{u_p} \cdot N_0 \nabla\Gamma \rangle \,\mathrm{d}t\,. \tag{A.16}$$

Second linear convective term for Equation (A.1):

$$\int_0^T \left\langle \Upsilon \cdot \delta(u_r \mathbf{U}'\,\hat{z}) \right\rangle \mathrm{d}t \;=\; \int_0^T \left\langle \delta\mathbf{u} \cdot \left(\mathbf{U}'\,\Upsilon_z\,\hat{r}\right) \right\rangle \mathrm{d}t\,, \tag{A.17}$$

similarly for Equation (A.2):

$$\int_0^T \left\langle \Upsilon_p \cdot \delta(u_{pr} \mathbf{U}'\,\hat{z}) \right\rangle \mathrm{d}t \;=\; \int_0^T \left\langle \delta\mathbf{u_p} \cdot \left(\mathbf{U}'\,\Upsilon_{pz}\,\hat{r}\right) \right\rangle \mathrm{d}t\,, \tag{A.18}$$

and for Equation (A.3):

$$\int_0^T \langle \Gamma \cdot \mathbf{U}\,\partial_z(\delta N) \rangle \,\mathrm{d}t \;= -\int_0^T \left\langle \delta(N_0 + N') \cdot \mathbf{U}\,\partial_z \Gamma \right\rangle \mathrm{d}t\,. \tag{A.19}$$

The pressure term for Equation (A.1):

$$\int_0^T \Upsilon \nabla \cdot \langle\, \delta p \rangle \,\mathrm{d}t \;=\; \int_0^T \langle\, \delta\,(\nabla p\,\Upsilon) \rangle \,\mathrm{d}t \;-\; \int_0^T \delta p \cdot \langle\, \nabla\Upsilon \rangle \,\mathrm{d}t$$

$$=\; -\int_0^T \delta p \cdot \langle\, \nabla\Upsilon \rangle \,\mathrm{d}t\,. \tag{A.20}$$

Diffusion term for Equation (A.1):

$$\int_0^T \left\langle \Upsilon \cdot \nabla^2 \delta\mathbf{u} \right\rangle \mathrm{d}t \;=\; \int_0^T \langle \nabla\,(\Upsilon \nabla \delta\mathbf{u}) \rangle \,\mathrm{d}t - \int_0^T \langle \nabla\Upsilon\,\nabla\delta\mathbf{u} \rangle \,\mathrm{d}t$$

$$= -\int_0^T \left\langle \delta\mathbf{u} \cdot \nabla^2 \Upsilon \right\rangle \mathrm{d}t + \int_0^T \left\langle \nabla \left(\nabla\Upsilon \cdot \delta\mathbf{u} \right) \right\rangle \mathrm{d}t$$

$$= -\int_0^T \left\langle !\delta\mathbf{u} \cdot \nabla^2 \Upsilon \right\rangle \mathrm{d}t \,, \tag{A.21}$$

Stokes terms for Equation (A.1):

$$\int_0^T \left\langle \Upsilon \cdot \delta \left[\frac{K}{\rho_f} (N_0 + N') \left(\mathbf{u_p} - \mathbf{u} \right) \right] \right\rangle \mathrm{d}t =$$

$$\int_0^T \left\langle \delta\mathbf{up} \cdot \left[\frac{K(N_0+N)}{\rho_f} \Upsilon \right] \right\rangle \mathrm{d}t \; - \int_0^T \left\langle \delta\mathbf{u} \cdot \left[\frac{K(N_0+N)}{\rho_f} \Upsilon \right] \right\rangle \mathrm{d}t$$

$$+ \int_0^T \left\langle \delta N_0 \cdot \left[\frac{K}{\rho_f} \left(\mathbf{u_p} - \mathbf{u} \right) \right] \right\rangle \mathrm{d}t \; + \int_0^T \left\langle \delta N \cdot \left[\frac{K}{\rho_f} \left(\mathbf{u_p} - \mathbf{u} \right) \right] \right\rangle \mathrm{d}t \,, \tag{A.22}$$

and Equation (A.2):

$$\int_0^T \left\langle \Upsilon_p \cdot \delta \left[\frac{K}{m_p} \left(\mathbf{u} - \mathbf{u_p} \right) \right] \right\rangle \mathrm{d}t = \int_0^T \left\langle \delta\mathbf{u} \cdot \left[\frac{K}{m} \Upsilon_p \right] \right\rangle \mathrm{d}t \; - \int_0^T \left\langle \delta\mathbf{u_p} \cdot \left[\frac{K}{m_p} \Upsilon_p \right] \right\rangle \mathrm{d}t$$

$$+ \int_0^T \left\langle \delta N_0 \cdot \left[\frac{K}{\rho_f} \left(\mathbf{u_p} - \mathbf{u} \right) \right] \right\rangle \mathrm{d}t \; + \int_0^T \left\langle \delta N \cdot \left[\frac{K}{\rho_f} \left(\mathbf{u_p} - \mathbf{u} \right) \right] \right\rangle \mathrm{d}t \,. \tag{A.23}$$

The final expression of $\delta\mathscr{L}$ is:

$$\begin{aligned}
\delta\mathscr{L} = {} & \left\langle \delta\mathbf{u}(T) \left(m_f u(T) - \Upsilon(T) \right) \right\rangle + \left\langle \delta\mathbf{u}(0) \left(\Upsilon(0) - \lambda\, m_f\, \mathbf{u}(0) \right) \right\rangle \\
& + \left\langle \delta\mathbf{u_p}(T) \left(m_p\, \mathbf{u_p}(T) - \Upsilon_p(T) \right) \right\rangle + \left\langle \delta\mathbf{u_p}(0) \left(\Upsilon_p(0) - \lambda\, m_p\, \mathbf{u_p}(0) \right) \right\rangle \\
& - \left\langle \delta N(T) \; \frac{m_p}{N(T)} \mathbf{u_p}(T) \right\rangle - \left\langle \delta N(0) \; \lambda \, \frac{m_p}{N(0)} \mathbf{u_p}(0) \right\rangle \\
& - \int_0^T \left\langle \delta\Upsilon \cdot \mathrm{NS} \right\rangle \mathrm{d}t \; - \int_0^T \left\langle \delta\Upsilon_p \cdot \mathrm{NSp} \right\rangle \mathrm{d}t \; - \int_0^T \left\langle \delta\,\Pi \cdot [\nabla \cdot \mathbf{u}] \right\rangle \mathrm{d}t \; - \int_0^T \left\langle \delta\,\Gamma \cdot \mathrm{Neq} \right\rangle \mathrm{d}t \\
& + \int_0^T \left\langle \delta\mathbf{u} \cdot \partial_t \Upsilon + \mathbf{U}\,\partial_z \Upsilon - \Upsilon_z \mathbf{U}' \hat{\mathbf{r}} + \nabla\Pi + \nu\nabla^2\Upsilon + \frac{K N_0}{\rho_f} \Upsilon - \frac{K}{m_p} \Upsilon_p \right\rangle \mathrm{d}t \\
& + \int_0^T \left\langle \delta\mathbf{u_p} \cdot \left[\partial_t \Upsilon_p + \mathbf{U}\,\partial_z \Upsilon_p - \Upsilon_{pz} \mathbf{U}' \hat{\mathbf{r}} + N_0 \cdot \nabla\Gamma \frac{K}{m_p} \Upsilon_p - \frac{K N_0}{\rho_f} \Upsilon \right] \right\rangle \mathrm{d}t \\
& + \int_0^T \left\langle \delta N' \cdot \partial_t \Gamma + \mathbf{U}\,\partial_z \Gamma + \mathbf{u_p} \nabla\Gamma + \right\rangle \mathrm{d}t \,.
\end{aligned} \tag{A.24}$$

A.2 Adjoint system of equations

In order to maximise the variational $\mathscr{L}$ we have to find the value for which $\delta\mathscr{L} = 0$. It can be done by having each of the term of Equation (A.24) to be equal to 0. The integrals terms gives the modified set of Navier-Stokes equations used in chapter 2, equal to the Equations (2.15)-(2.18), as well as the adjoint system of equations:

$$\partial_t \Upsilon = -\mathbf{U}\cdot\nabla\Upsilon + \Upsilon\cdot\mathbf{U} - -\nabla\Pi - \frac{1}{Re}\nabla^2\Upsilon - \frac{fN_0}{SRe}\Upsilon + \frac{1}{SRe}\Upsilon_p\,, \tag{A.25}$$

$$\partial_t \Upsilon_p = -\mathbf{U}\cdot\nabla\Upsilon_p + \Upsilon_p\cdot\mathbf{U} + N_0\nabla\Gamma + \frac{fN_0}{SRe}\Upsilon - \frac{1}{SRe}\Upsilon_p\,, \tag{A.26}$$

$$\partial_t \Gamma = -\mathbf{U}\cdot\nabla\Gamma - \mathbf{u_p}\cdot\nabla\Gamma\,. \tag{A.27}$$

The other terms being equal to 0 produce another set of conditions:

$$\mathbf{u}(T) = \Upsilon(T) \quad , \quad \mathbf{u_p}(T) = \Upsilon_p(T)\,, \tag{A.28}$$

$$\lambda\mathbf{u}(0) - \Upsilon(0) = 0 \quad , \quad \lambda\mathbf{u_p}(0) - \Upsilon_p(0) = 0\,. \tag{A.29}$$

A.3 Additional plots

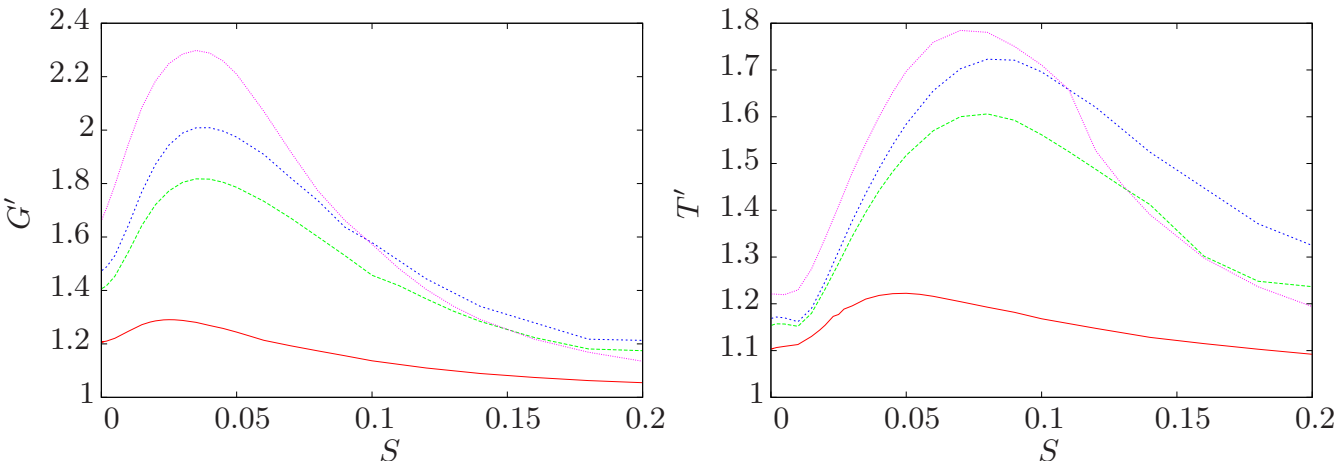

Figure A.1: Ratio of growth between particulate and single phase flow as a function of S for $f = 0.1$ and $Re = 500$ in the case of a Gaussian particle distribution centred around $r_d = 0.7$. Uniform distribution (red), $\sigma = 0.15$ (green), $\sigma = 0.12$ (dotted blue), $\sigma = 0.10$ (purple).

Appendix B

Point particle code, misc.

B.1 Non-dimensionalisation details for point particle model

The dimensional variables used are the centreline velocity U_0, the radius of the pipe r_0 and the ratio between particle and pipe radius $a' = a/r_0$. The time is normalised as $T_0 = r_0/U_0$.

The dimension of the time dependent term is: $\frac{m_p U_0}{T_0}$.
The right-hand side terms have to be normalised by this constant to obtain a dimensionless equation.

$-6\pi a\mu\left(\mathbf{u_p} - \mathbf{u} - \frac{a^2}{6}\nabla^2\mathbf{u}\right)$ is the drag force term. The dimension of the drag force term is:

$$\frac{T_0}{m_p U_0} 6\pi a\mu U_0 = \frac{6\pi a\mu T_0}{4/3\pi\rho_p a^3} = \frac{9}{2}\frac{1}{a^2}\frac{1}{\rho_p} T_0\mu \ . \tag{B.1}$$

Using $\mu = \nu\rho_f = \frac{\rho_f U_0 r_0}{Re} = \frac{\rho_f L_0^2}{ReT_0}$ we get the dimensionless form of the drag term:

$$-\frac{9}{2}\frac{L_0^2}{a^2}\rho_t\frac{1}{Re}\left(\mathbf{u_p}' - \mathbf{u}' - \frac{a^2}{L_0^2}\nabla'^2\mathbf{u}'\right) = \frac{1}{SRe}\left(\mathbf{u_p'} - \mathbf{u}' - \frac{a^2}{L_0^2}\nabla'^2\mathbf{u}'\right) \ , \tag{B.2}$$

with $S = \frac{2}{9}\frac{a^2}{L_0^2}\rho_t$ the dimensionless relaxation time and $\rho_t = \rho_f/\rho_p$ the density ratio.

$-\frac{m_f}{2}\frac{d}{dt}\left(\mathbf{u_p} - \mathbf{u} - \frac{a^2}{10}\nabla^2\mathbf{u}\right)$ is the added mass term , additional inertia because the particle has to displace the fluid. This term is identical to the time-derivative term except for fluid instead of particle mass so the non-dimensionalisation is straightforward:

$$-\frac{\rho_t}{2}\frac{d'}{dt}\left(\mathbf{u_p'} - \mathbf{u}' - \frac{a'^2}{10}\nabla'^2\mathbf{u}'\right) \ . \tag{B.3}$$

$m_f\frac{D}{Dt}\mathbf{u}$ is the pressure gradient of the flow (without particle effect), same principle than added mass. Note that it corresponds to $-\nabla p$ which is computed by our numerical program. The dimensionless form is:

$$\rho_t\frac{D'}{Dt}\mathbf{u}' \ , \tag{B.4}$$

$(m_p - m_f)g$ is the buoyancy term. Dimension, $\frac{T_0}{m_p U_0}(m_p - m_f)g$, giving: $(1-\rho_t)Ri$
with $Ri = g\frac{r_0}{u_0^2}\mathbf{g}$ the Richardson number. For the direction of g, $\mathbf{g} = -\sin(\theta)\mathbf{e_r} + \cos(\theta)\mathbf{e}_\theta$.

Low Risk Research Ethics Approval

Some materials have been removed from this thesis due to Third Party Copyright. Pages where material has been removed are clearly marked in the electronic version. The unabridged version of the thesis can be viewed at the Lanchester Library, Coventry University

Low Risk Research Ethics Approval Checklist